Estimation of regional mass balance changes of the Greenland ice sheet using GRACE data and the Input-output method

Xu, Zheng

DOI
10.4233/uuid:ef8425da-0eee-45b3-8e29-086e5fb41ede

Publication date
2019

Document Version
Final published version

Citation (APA)
Xu, Z. (2019). *Estimation of regional mass balance changes of the Greenland ice sheet using GRACE data and the Input-output method*. [Dissertation (TU Delft), Delft University of Technology].
https://doi.org/10.4233/uuid:ef8425da-0eee-45b3-8e29-086e5fb41ede

Important note
To cite this publication, please use the final published version (if applicable).
Please check the document version above.

Estimation of regional mass balance changes of the Greenland ice sheet using GRACE data and the Input-output method

Estimation of regional mass balance changes of the Greenland ice sheet using GRACE data and the Input-output method

Proefschrift

ter verkrijging van de graad van doctor
aan de Technische Universiteit Delft,
op gezag van de Rector Magnificus Prof.dr.ir. T.H.J.J. van der Hagen,
voorzitter van het College voor Promoties,
in het openbaar te verdedigen op
Woensdag 24 April 2019 om 10:00

Door

Zheng Xu

M.Sc., UNESCO-IHE,
Delft, Netherlands
geboren te Jiangsu, China

This dissertation has been approved by the

Promotor: Prof.dr.ir. P.N.A.M. Visser

Copromotor: Dr.ir. E.J.O. Schrama

Composition of the doctoral committee:

Rector Magnificus	Chairperson
Prof. dr. ir. P.N.A.M. Visser	Technische Universiteit Delft
Dr.ir. E.J.O. Schrama	Technische Universiteit Delft

Independent members:

Prof.dr.ir. M. Mulder	Technische Universiteit Delft
Prof.dr.-Ing. N. Sneeuw	Universität Stuttgart
Prof.dr.-Ing. J. Kusche	Universität Bonn
Prof.dr.M.R. van den Broeke	Universiteit Utrecht
Prof.dr.L.L.A. Vermeersen	Technische Universiteit Delft
Prof.dr.ir.H.W.J. Russchenberg	Technische Universiteit Delft, reservelid

Dr.ir. W. van der Wal heeft als begeleider in belangrijke mate aan de totstandkoming van het proefschrift bijgedragen.

This research is funded by means of scholarship ALW-GO-AO/27 provided by the Netherlands Organization of Scientific Research, NWO.

Keywords: Greenland Ice Sheet, GRACE, RACMO2, mass balance, constraints

Printed by: IPSKAMP printing

Front & Back: Qixuan Li

ISBN:

An electronic version of this dissertation is available at

http://repository.tudelft.nl/.

Table of Contents

Contents

Acknowledgements

Eight years ago, I made my first life-changing decision on my own. I decided that the Netherlands will be my next stop. So, at this point, I think I have to give my first acknowledgement to my parents, they are the ones who backed me up and supported me all the way up to now. Moreover, they taught me to think free and act brave. Because of them, I enjoyed a great journey which not only took me to many different countries but also gave me many more friends; the rest of my life I will benefit by the knowledge and skills that I picked up on the way.

The next one on my list is an anonymous friend. The day I arrived in the Netherlands was a rainy day (of course). I didn't plan the road from the airport to my school in Netherlands, since my sister who had studied in Delft promised to pick me up. But the story didn't begin well. She mistook the time and did not show up at the airport. I waited several hours then made an impulsive decision that I would find the way to the school by myself. I should mention that I never spoke English outside a classroom at that time, google maps was not an option and I brought 4 pieces of luggage (my mom packed everything I had plus much more, so each piece of luggage was heavy like a truck). The trip by train was very friendly for foreigners, but once I left the Delft Zuid station I was completely lost in the city. I still remember that I stood in the rain at a crossroad and felt that I was a small boat in the middle of ocean, although later it turned out this city was no larger than a small village. Anyway, help came unexpectedly, an Indian guy discovered my hopelessness and he stopped and asked my destination. I told him the abbreviation of my school since I could only remember that much. It was very fortunate, he had a friend who studied there. So he walked me to a bus stop, helped me with the baggage, and paid my ticket (I only had five notes of 100 in my pocket). The rest of the story was just like any other foreign student arriving the first time at school. Now I would like to take the opportunity to give my best wishes to this anonymous friend, live long and prosper.

Eight years later I became a skillful traveler. I had traveled several times alone, I can live and work in a completely new city without any discomfort. At the end of my overseas adventure, that moment surfaced in my mind. I'm still in the middle of an ocean, but now I am stronger, more confident and more determined. My 8 years away from home were a long and bumpy road, but I met a great number of people who helped me along the way. Firstly, my sincere gratitude is to Dr.ir. E.J.O. (Ernst) Schrama. Thank you EJO, you led me into a new and challenging field, you did not give up on me when I was down, you let me see the joy and difficulties of being a scientist, you gave all your support for me to finish my thesis even after I left Delft. No matter whether I will continue my work in science, I will always be proud to be one of your PhD students. Then a slightly smaller thanks to Dr.ir. W. (Wouter) van der Wal. Just like Frodo Baggins has Sam (of course you are million times more gorgeous than Sam), I may never reach the "Mount Doom" without your help. For you, one bottle of beer says all.

Special thanks to Prof. Boudewijn Ambrosius, Prof. Pieter Visser and Prof. Bert Vermeersen, thank you for offering me the opportunity to pursue my PhD in the Astrodynamics and Space

Missions group. Many thanks to Prof. van den Broeke in Utrecht University (UU/IMAU), the face-to-face discussions about Greenland and RACMO deepened my understanding. Also many thanks to Dr. Ellyn Enderlin, without your discharge data I could not have completed my work. My gratitude to Dr. Ir. Bert Wouters, your research enlightened me to carry out my study of the GRACE and GrIS regional mass.

Thanks to my dear colleagues, Ron, Erwin, Marc (black T-Shirt version), Dominic, Eelco, Bart, Jose, Wim, Jacco, Sowmini, Joao, Guido, Mao and those who used to work in the group but left at some point. Although I'm not very interactive in the office and after work, you created a comfortable, family-like atmosphere in our group, which I appreciated a lot. Last but not the least, one lady should be mentioned, the "forever life saver", best secretary so far, guardian of young PhDs, dear N. (Relly) van Wingaarden. Every time I showed up in front of your door with tons of troublesome questions, you made some phone calls then told me that everything would be OK and you would take care of me. I wish the group will have you forever and thank you so much for everything.

I came to Netherlands alone, but had a big family when I left. This family is not bound by blood, but is still undivided in spite of the physical distance. Just mentioning their names is not enough to express my gratitude and unnecessary, they are the reasons that my life in Netherland is colorful and interesting. You are part of my life till the end of time.

This research is funded by means of scholarship GO-AO/27 provided by the Netherlands Organization of Scientific Research, NWO. During the writing, Dr. Ir. Bert Wouters and Dr. Ir. Cornelis Slobbe contributed as reviewers, their comments are more than valuable. I sincerely appreciate all of their advice and the time they gave to read my draft. The committee members of my PhD are also greatly acknowledged, for the devotion of time to read my dissertation and for being a part of my defense ceremony.

Delft, The Netherlands, December 2017

Zheng Xu (Black)

Summary

In the 21st century, polar land ice melting became one of the driving factors of global sea level rise, which is discussed widely by the media and the public. Although the fact of the shrinking ice caps and accompanying changes in the sea level is established, the actual amount of polar ice melting still needs to be quantified in separate regions. Sitting on top of bedrock, the Greenland ice sheet (GrIS) is the second largest ice sheet on Earth. With traditional glaciological methods the change of the Greenland ice sheet is difficult to measure directly, however with the GRACE (Gravity Recovery and Climate Experiment) satellite system the mass changes can be measured directly. There are several sub-drainage areas within the Greenland Ice Sheet. Some of the subsystems may contribute differently to the overall mass changes of GrIS. For instance, while the mass loss in the GrIS ablation zone is enhanced during the last decades, the central high altitude areas experienced increased mass accumulation (Krabill et al., 2000, Thomas et al., 2001, Colgan et al., 2015, Xu et al., 2016). It is important to quantify the regional mass changes because it gives us insight what is going on beyond the realization that the GrIS is shrinking.

Different methods have been implemented in the literature to estimate regional mass changes. As in this study, we are interested mainly in two methods, i.e.: 1) Using GRACE data to derive the GrIS mass changes (GRACE method); 2) Using modelled Surface Mass Balance (SMB) and ice discharge (D) estimates in the so-called Input-output Method (IOM method). Between these two methods, a good agreement can be found on the mass change estimates for the entire GrIS and in some sub-regions. However, in some reports in which different regional mass changes estimates are compared, we find: 1) some mass loss estimates are recognized as similar because uncertainty in one or both estimates is large; 2) in some regions, particular in the southeastern and northwestern GrIS, the comparison between methods show differences larger than the error margin. Hence, in our study, we focus on reducing the uncertainty in two types of GrIS mass loss estimates, derived from the satellite gravimetry measurements and based on the results of the IOM. With our method we get better estimates of the regional mass changes of the GrIS by properly configuring constraints during inversion while reducing bias towards to the a priori models used to derive the constraints.

In our study, we use the level-2 data from the twin satellite Gravity Recovery and Climate Experiment (GRACE). Both satellites were launched in 2002. The satellites provided global surface mass change measurements until November 2017. There are several inversion strategies to retrieve regional mass loss from GRACE level data. Schrama et al. (2011) proposed a least-squares inversion to recover the regional mass changes of GrIS from the GRACE level-2 spherical harmonic data. We adopt this method and focus on the constraints that are applied in the inversion of regional mass changes of the GrIS. Based on mass change rates of different GrIS regions, we propose to use separate constraints to limit the variance of the mass changes in two different areas,

i.e. the areas below and above the 2000 m elevation contour. Together with the constraints for the surrounding Arctic areas, we replaced the original single constraint in Schrama et al. (2011) with three different constraints. In order to determine suitable values for the constraints, we utilize a multi-objective optimization approach based on a simulation in which the GrIS mass changes is modelled by an SMB model and an estimate of the ice discharge. To test our method, we create a simulation of the GrIS mass changes mainly based on an IOM method. By implementing our method on the simulation, we find that with these improved constraints the approximation error in the mass change estimates in each GrIS region is reduced.

During the study of optimizing the constraints for GRACE solution, we noticed the correlation between the GRACE data and the approximation error in the GRACE solution. Thus we extend the use of the IOM solution based simulation to quantify the relationship between the approximation errors in the constrained least-squares inversion approach and the simulated mass changes signals, which can be seen as signal to noise ratio. We found that we can apply this signal to noise ratio to the GRACE inferred solution to further reduce the approximation errors by maximum ~40% (in the simulation). Still, even with this improvement in GRACE estimates there are regional differences in the northwest GrIS compared to the IOM solution. For this reason, we investigate the IOM solution, the surface mass changes model (RACMO2) and the ice discharge estimate (Enderlin et al, 2013). In a standard IOM solution, in order to compensate the uncertainty accumulation in the IOM approach, a reference SMB and D are subtracted from the SMB and D estimates because it helps to remove the uncertainties accumulated in the Total Mass Balance (TMB) over a long time period (see chapter 3.2). The reference SMB and D are the averaged SMB and D over a certain time period during which the GrIS is considered as stable. However, due to the SMB model uncertainty and lack of historical discharge measurements in the northwest, the reference estimate in this region is less accurate, especially the reference discharge. Thus, we replace the reference discharge in some regions with discharge based on modelled run-off from the RACMO2 model, which noticeably reduces the discrepancy between the GRACE solution and the IOM solution in some regions. Nevertheless, the difference in the northwestern GrIS remains. After validating our GRACE results with mass change estimates in this region based on satellite altimetry we conclude that the current uncertainty estimate in the IOM solution for this area is too low.

The last contribution of this study is to explore the capability of the GRACE data for deriving mass change estimates at a finer subdivision of the GrIS sub region, i.e. 19 sub-basins. We realize that, in order to get better estimates for smaller areas, more specific constraints than for the 8 sub-basins set-up are required, otherwise the approximation errors result in large uncertainties in the regional mass changes estimates. However, the method through which we optimize the regional constraints relies on an IOM based simulation of the GrIS and, as we concluded before, in some regions the IOM method is less reliable and validation of the IOM requires estimates that are independent from IOM.

To derive some constraints for the smaller regions we use the fact that the estimates for the large areas (i.e. 8 GrIS basins) are more robust, i.e. they depend less on the constraints. For this reason,

we propose a new hierarchical constraint method to derive mass changes in small GrIS regions from GRACE, i.e.: to constrain the small regions with estimates of the large regions that are composed of random combinations of smaller regions. With this method we do not need a simulation or a priori information other than what is necessary for the largest mascons in the hierarchical method. In order to validate this method, we apply it to simulated mass changes and compare it against a standard least-squares inversion with an optimized single constraint applied to the same simulation. We find that in most regions the hierarchical constraint method is capable to retrieve similar mass changes estimates as the standard single constraint method, and in some regions it shows even better consistency to the simulation.

In this study, we have investigated different methods to improve both the GRACE and IOM based regional mass changes estimates. The methods developed in chapter 2 and chapter 3 require some prior knowledge about the mass changes of GrIS, such as a GrIS mass changes simulation based on models and observations. We suggest that these methods can be applied to other areas, such as in Antarctica and Alaska if a simulation is available. In chapter 4 we present a feasible way to retrieve the regional mass from GRACE data.

Samenvatting

Landijs in de polaire gebieden is één van de bepalende factoren voor mondiale zeespiegelverandering geworden in de 21e eeuw. Het onderwerp wordt breed besproken in de media en de samenleving. Het is een feit dat landijs verdwijnt en dat dit leidt tot zeespiegel verandering, maar het is moeilijker te kwantificeren in welke gebieden op aarde en in welke mate het ijs verdwijnt. Liggend op het vaste land is de Groenlandse ijskap het twee na grootste ijssysteem op aarde. Met traditionele glaciologische methoden is het moeilijk de verandering van de ijsvoorraad op Groenland direct te meten. Met de GRACE (Gravity Recovery and Climate Experiment) satellietmissie kunnen de veranderingen in de ijsvoorraad direct gemeten worden. Er zijn verschillende subsystemen binnen de Groenlandse ijskap (GrIS), namelijk de stroomgebieden, die zijn bepaald door de lokale topografie. Sommigen van deze subsystemen kunnen een andere bijdrage leveren aan het totale massaverlies van de GrIS. In (Krabill et al., 2000), (Thomas et al., 2001), (Colgan et al., 2015), (Xu et al., 2016) zien we bijvoorbeeld een toename van massaverlies in de GrIS afsmeltzone gedurende de laatste 20 jaar, terwijl de zone boven de 2000 meter een toename van massa laat zien. Het is belangrijk de regionale massaveranderingen te kwantificeren omdat het meer inzicht geeft in wat er aan de hand is dan simpelweg te realisatie dat de GrIS massa verliest.

In de literatuur zijn verschillende methodes geïmplementeerd om regionale massaveranderingen te bepalen. Een hoge mate van overeenkomst kan gevonden worden tussen de verschillende resultaten voor de gehele GrIS en in enkele deeL-gebieden. We zijn geïnteresseerd in twee methoden: 1) de GRACE methode om de massaverandering te bepalen, 2) het gebruik van oppervlakte massa balansen en ijsgangmetingen in de zogenoemde Input-output methode. In verschillende artikelen waar regionale massabalansschattingen worden vergeleken vinden we: 1) dat de massa verliezen alleen overeenstemmen als er een grote onzekerheidsmarge wordt aangenomen, 2) In bepaalde gebieden, met name in het zuidoosten en noordwesten van de GrIS, is het verschil tussen verschillende methoden groter dan de foutmarge. In deze studie concentreren we ons op het verminderen van de onzekerheden van schattingen van de massaverliezen van de GrIS afgeleid uit 1) satelliet gravimetrie en 2) het oppervlakte massa balans model (SMB) en de ijsgangmetingen (D). Met onze methode krijgen we een verbeterde schatting van de regionale massa balansen binnen de GrIS door verbeterde limiteringendie gebruikt worden bij de inversie; hiermee voorkomen we dat de oplossingen beïnvloed worden door a-priori modellen die we gebruiken voor de afleiding van limiteringen.

In onze studie maken we gebruik van de level-2 gegevens van de GRACE (Gravity Recovery and Climate Experiment) tweeling-satellietmissie. Beide satellieten werden in 2002 gelanceerd; in November 2017 kwam een einde aan de eeks van wereldwijde metingen van de massaverandering. Er bestaan verschillende strategieën om een regionaal massaverlies uit de GRACE metingen af the leiden. In Schrama et al (2011) wordt een kleinste-kwadrateninversie voorgesteld waarbij regionale

massaveranderingen over de GrIS worden afgeleid uit de GRACE level-2 potentiaalcoefficiënten. We nemen deze methode als uitgangspunt waarbij we ons concentreren op de limiteringen die tijdens de inversie van de regionale massa verandering binnen de GrIS gebruikt worden. Gebaseerd op de snelheid waarmee massa verandert in verschillende GrIS gebieden stellen we verschillende type limiteringen op; hiermee kunnen we de variantie van de massaveranderingen in gebieden onder en boven de 2000 meter hoogtelijn beperken. Samen met de limiteringen voor de omliggende Arctische gebieden vervangen we de limitering die gebruikt werd in Schrama et al. (2011) door drie alternatieve constraints. Een multi-criteries optimalizatie-methode gebaseerd op een simulatie van de GrIS door middel van modellen van de SMB en de D is gebruikt om geschikte limiteringen te vinden. Met deze nieuwe constraints vinden we dat de benaderingsfout van het GrIS in elk sub-gebied wordt verkleind. Het eindresultaat na toepassing van de limiteringen komt beter overeen met het SMB model en de ijsgangveranderingen.

We hebben gebruik gemaakt van een simulatie die gebaseerd is op de Input-output Methode (IOM) om te kwantificeren welke mogelijke verbanden er bestaan tussen de eerder genoemde benaderingsfouten en de kleinste-kwadraten methode die afhangt van limiteringen en gesimuleerde massaveranderingen. We vinden dat het toepassen van gesimuleerde signaaL-ruisverhouding in de GRACE oplossingen de benaderingsfouten tot circa 40% reduceert. Dit neemt niet weg dat, nadat we deze verbetering hebben aangebracht, er nog steeds regionale verschillen bestaan in het noordwesten van de GrIS ten opzichte van de IOM oplossing. Om deze reden bestuderen we de IOM-oplossing bestaande uit het RACMO2 model (SMB) en de ijsgangschattingen (D) (Enderlin et al, 2013). In de IOM oplossing is het gebruikelijk om de onzekerheden in de berekening te reduceren door zogenaamde referentiewaarden voor de SMB en de D in rekening te brengen. Er bestaan onzekerheden in het SMB model en er is een gebrek aan historische ijsgangmetingen in het noordwesten van Groenland, in deze regio zijn de referentieschattingen daarom minder nauwkeurig in het bijzonder voor de ijsgangmetingen (D). Om deze redenen vervangen we de referentieijsgang D in bepaalde gebieden waarbij we gebruik maken van de gemodelleerde run-offs verkregen uit het RACMO2 model; deze procedure vermindert de discrepantie tussen de GRACE oplossing en de IOM oplossing in bepaalde gebieden. Niettemin blijft er een verschil bestaan in het noordwesten van de GrIS. Een validatie tussen de GRACE-resultaten en massa schattingen uit satelliet altimetrie leert dat de IOM-oplossing een grotere onzekerheid heeft in dit gebied.

De laatste bijdrage in deze studie bestaat uit het onderzoeken of het met GRACE data mogelijk is massaveranderingen te schatten in gebieden kleiner dan de tot nu toe gebruikte 19 sub-stroomgebieden. Wij realizeren ons dat, om betere schattingen te krijgen in kleinere gebieden, specifiekere limiteringen nodig zijn dan gebruikt voor de 8 stroom gebieden, omdat anders de benaderingsfouten kunnen leiden tot grote fouten in de regionale massabalansschattingen. De methode die gebruikt is om de regionale limiteringen te optimaliseren hangt af van de IOM simulatie van het GrIS, en, zoals we al eerder concludeerden, in sommige gebieden is de IOM methode minder betrouwbaar of ontbreken onafhankelijke schatting voor de validatie van de IOM.

De limiteringen die we gebruiken voor de acht grote stroomgebieden zijn gebiedsafhankelijk waarbij met de onzekerheid per gebied rekening wordt gehouden. Om deze reden stellen we in

hoofdstuk vier een methode voor om de limiteringen op te stellen voor kleinere gebieden die binnen grote gebieden in het GrIS liggen. Deze methode noemen we de hierarchische limiteringen methode. Met deze nieuwe methode hebben we geen simulatie of a-priori informatie nodig anders dan welke noodzakelijk is voor de grootste mascons in de hierarchische methode. We vinden dat de met de limiteringen geoptimaliseerd voor de grootste massaconcentraties de benaderingsfouten voor kleinere limiteringen geminimaliseerd worden. Een vergelijking met de IOM oplossing laat een goede overeenkomst tussen beide methoden zien in de meeste kleine gebieden.

In deze studie zijn verschillende methoden bestudeerd om regionale massabalansschattingen zowel van GRACE als de IOM verbeteren. Als er een simulatie beschikbaar is dan suggereren we dat de methoden ontwikkeld in in hoofdstuk 2 en 3 ook toegepast kunnen worden in andere gebieden, zoals Antarctica en Alaska. In het geval er geen simulatie bestaat kan de methode beschreven in hoofdstuk 4 gebruikt worden om regionale massaschattingen te maken.

Chapter 1

Introduction

1.1 Background

The Greenland ice sheet (GrIS) is the largest ice sheet on the northern hemisphere. The total extent is ~1.7×10^6 km^2, occupying ~81% of Greenland. The average thickness is ~1600 m reaching over 3000 m in the center and south of Greenland. The GrIS has a significant effect on the global climate, and it is large enough to create its own climate (Petersen et al., 2004; van Angelen, 2013). The observed mass loss of the GrIS during the last two decades is recognized as a key indicator of climate change, as mentioned in the Fifth Assessment Report (AR5) of the Intergovernmental Panel on Climate Change (IPCC) (Pachauri et al., 2015). The GrIS exhibits a clear increase in mass loss trend from 2002 up to the moment of writing (2016) compared to the mass loss in the 90s. A review of the Greenland mass loss between 1992 to 2011 can be found in Shepherd et al. (2012). Their reconciled Greenland mass changes based on four different techniques suggests -142±49 $Gt\cdot yr^{-1}$ in the timeframe 1992 to 2011 where one Gigaton is approximately equal to 1 km^3 of water. During the first decade (1992 – 2000) the mass balance of the GrIS was -15±65 $Gt\cdot yr^{-1}$, which increased to -211±37 $Gt\cdot yr^{-1}$ between 2000 and 2011 and -263±30 $Gt\cdot yr^{-1}$ between 2005 and 2010.

It is mentioned in AR5 that the increasing speed of GrIS ice sheet mass loss is one of the major drivers of global mean sea level rise during 1993–2010. In Shepherd et al. (2012) it is mentioned that the GrIS has lost around 2700±930 Gigaton of ice between 1993 and 2011, which is equivalent to an increase of the global mean sea level of 7.5±2.5 mm. Furthermore, global ecosystems are greatly affected by the continuously increasing mass loss of the GrIS along with changes in other land glaciers (Hoegh-Guldberg and Bruno, 2010). Changes in the regional mass balance can directly affect the local climate and ecosystems (Hoegh-Guldberg and Bruno, 2010), e.g. the land ice melting in the Arctic has a strong impact on a variety of organisms living above and below the ice in this region. Therefore, it is essential to understand the regional mass changes of the GrIS.

To quantify the changes of the GrIS mass balance one can use the model based methods, such as a Surface Mass Balance (SMB) model and estimates of the ice discharge to investigate the mass conservation of the GrIS. Other ways to measure the mass changes are based on gravity observations from the GRACE satellite mission and from satellite altimetry observations. These methods can be used to produce estimates for the entire GrIS but also regionally for the individual glacier basins of which the Greenland ice sheet is composed. The focus of this thesis is on the satellite gravimetry, therefore in the following sections we will discuss the method for analyzing the GRACE data.

1.2 Regional mass changes approximation

Since 2002 the GRACE mission provides inter-satellite range data aided by GPS tracking and accelerometers that provide us with monthly gravity field solutions that formed the basis for many studies providing estimates of the GrIS mass changes. During the first several years of the GRACE mission most studies focused on isolating the mass change signal from noise that originates from the measurements or from the background correction models or from signal outside the study region (i.e. leakage). The objective was to find the mass changes at the scale of the entire ice sheet, cf. Tapley et al. (2001) and Swenson et al. (2003). Filtering the GRACE data turned out to be essential to be able to observe mass variations at the Earth's surface, including a clear negative trend of mass change on the GrIS (Tapley and Bettadpur, 2004; Chen et al., 2005). To retrieve an accurate map of the GrIS mass change different versions of inversion methods were implemented, see for instance Velicogna and Wahr (2005), Luthcke et al. (2006) and Wouters and Schrama (2008). The different mass change rate estimates for the entire ice sheet have converged, as shown for instance in Shepherd et al. (2012).

At the early stages of the GRACE mission, Velicogna and Wahr (2005) used the GRACE data from 2002 to 2004 to recover a mass trend with a rate of -82±28 $Gt \cdot yr^{-1}$ over the Greenland area. Later, GRACE data indicated a higher mass loss estimate of -248±80 $Gt \cdot yr^{-1}$ with only two more years of data and with a correction for Glacial Isostatic Adjustment (GIA) with the ICE-5G model (Velicogna and Wahr, 2006). Van den Broeke et al. (2009) used GRACE data from 2003 – 2008 and compared the mass loss of the GrIS with output from a surface mass balance model (RACMO2) combined with ice discharge measurements derived from ice-penetrating radar. This so-called Input-output Method (IOM) indicated a Greenland mass loss of -237±20 $Gt \cdot yr^{-1}$. The mass loss trend increased when longer time periods of GRACE data were considered. Shepherd et al. (2012) reconciled several GrIS mass changes estimates including some based on GRACE data and found -263±30 $Gt \cdot yr^{-1}$ between 2005 and 2010. Later, other GRACE based studies have shown similar estimates, such as -280±58 $Gt \cdot yr^{-1}$ (2003 to 2014) in Velicogna et al. (2014), -278±19 $Gt \cdot yr^{-1}$ (2003–2013) in Schrama et al. (2014), -286±16 $Gt \cdot yr^{-1}$ (2003–2013) in Ran et al. (2015). Thus, GRACE inferred mass changes estimates are in agreement for the mass loss for the entire GrIS regardless of the differences between processing methods.

When we zoom in to smaller regions on the GrIS, it becomes clear that the regional mass change estimates do not always agree with each other, see for example the comparison between GRACE and IOM in the north-western and south-eastern areas in Sasgen et al. (2012) and in Velicogna et al. (2014). There are several reasons for the regional differences: 1) For the entire GrIS area, the noise in GRACE data as well as the influence of leakage are small compared to the actual mass variations (Wahr et al., 2006; Velicogna and Wahr, 2005; Wouters and Schrama, 2007). In smaller areas, the associated mass change signals are localized in higher degree and orders of the GRACE data where the noise is higher, for a discussion see Bonin and Chamber (2016). 2) When the regional estimates are combined to obtain an estimate for the whole GrIS, some errors in the regional estimates cancel out (Xu et al., 2015; 2016).

Before we discuss the differences between methods used for regional mass changes estimates,

it should be noticed that most of the implemented methods are based on the inversion approach. The basic steps of inversion are: 1) Choose a mascon definition that is a sub-set of the whole area, 2) Make an assumption of a certain mass distribution in each mascon and define scaling factors of the mass distribution, 3) Compare the assumption with the GRACE observation for various scaling factors, 4) Find the scaling factor that best matches the GRACE observation. The differences between regional GRACE estimates based on an inversion approach are due to differences in the realization of the above mentioned steps. In Swenson and Wahr, (2007), and Velicogna and Wahr (2005) averaging kernel functions are applied for large GrIS regions. This method derives the rescaling factors by comparing between signal before and after applying the Post-processing method to the GRACE data. A contour map of scaling factors can be obtained, which indicates the ratio between the actual Equivalent Water Height (EWH) changes and the EWH changes of GRACE data after Post-processing. In Velicogna and Wahr (2005) the averaging function is computed with the assumption that there is a uniform distribution of mass change in the coastal area and also that there is no mass change in the interior of the GrIS. However, multiple studies have suggested that neither the mass changes on coastal areas are evenly distributed nor that the mass changes of the interior GrIS are completely zero (van den Broeke et al., 2009; Sasgen et al., 2012). Besides, the averaging function for the entire GrIS extends to the neighboring land areas of north Canada where mass changes also occur (Schrama and Wouters, 2011; Luthcke et al., 2013).

One can also treat the GrIS as a collection of "points", which could be discs or squares but with small size (for instance, a 1^o x 1^o grid cell on the Earth's surface as in Luthcke et al., 2013). One can invert the point mass changes from the geopotential field and group all the point mass approximations within the studied region to obtain the regional mass changes approximation. Examples of point mass assumptions can be found in the studies of Forsberg and Reeh (2007), Sørensen and Forsberg (2010), Baur and Sneeuw (2011), Barletta et al. (2013), Schrama et al. (2014). The estimated mass in each point is sensitive to the Post-processing of the GRACE data, such as the GIA model and the background models (Barletta et al., 2013). Furthermore, not just for the mascon method but for all GRACE studies, a choice has to be made how to obtain the degree 1 term of the mass changes, which is not observed by GRACE (Swenson et al. 2008).

Wouters et al. (2008) implemented another inversion approach that assumes a fixed number of areas that correspond to drainage basins, which are expected to behave uniformly (Rignot and Kanagaratnam 2006). Scaling factors for each region are adjusted in order to fit the post-processed GRACE level-2 data (i.e., monthly potential coefficients produced by a GRACE processing center). By repeating this process, the best-fitting regionally averaged mass changes can be determined iteratively. For the whole GrIS, the result of this approach agrees with the results from the direct mascon method (Luthcke et al., 2006) and other independent studies, such as from Shepherd et al. (2012). However regional differences are found when comparing with Sasgen et al. (2012). Schrama and Wouters (2011) computed optimal scaling factors by utilizing the least-squares method instead of the iterative adjustment of the weights of each area as in Wouters and Schrama (2008). This least-squares inversion approach will be discussed in later chapters.

1.3 Research Motivation

The use of least-squares inversion techniques involving mascons shows consistent results compared to other methods in most GrIS drainage basins (van den Broeke et al., 2009; Sasgen et al., 2012; Shepherd et al., 2012 and Andersen et al., 2015). However, there are some regional differences between various methods, and an obvious question is: "*what causes these differences?*".

The mass changes recovered by GRACE are not uniform across the GrIS (Sasgen et al., 2012; Barletta et al., 2013; Luthcke et al., 2013; Velicogna et al., 2014; Wiese et al., 2015; Alexander et al., 2016 and Ran et al., 2017). A direct consequence of the latter, and of the nature of gravity data, is that basins in the neighborhood of the GrIS (notably Ellesmere and Baffin island, Iceland and Svalbard) also affect the mass loss on Greenland (Wouters et al., 2008; Sasgen et al., 2012; Bonin and Chambers, 2013 and Schrama et al., 2014); this effect was demonstrated in Wouters and Schrama (2007). The least-squares inversion method has also proven to be a good option to derive the regional mass changes from GRACE data (Schrama and Wouters, 2011; Bonin and Chambers, 2013). This method finds the mathematical optimal solution using the observation data but it relies on covariance information of data and of the signal. Thus, its solution may be biased, which leads to regional differences compared with other methods.

The results obtained by Schrama and Wouters (2011) show that basin mass changes are typically negatively correlated relative to neighboring basins after the inversion. This effect is referred to as the anti-correlation error, or as denoted in this thesis, the approximation error. Schrama and Wouters (2011) explained that the approximation error causes least-squares solutions to become noisier in smaller basins. They also found that the approximation error is reduced when several adjacent regions are combined. In order to reduce the approximation error, a-priori variances are introduced as regularization factors in the least-squares method. The results shown by Schrama and Wouters (2011) indicate that the anti-correlation error is reduced, but an open issue is to determine the a-priori variances in order to minimize the regional anti-correlation error.

A weak a-priori constraint is applied by Schrama and Wouters (2011) assuming that the a-priori variance is 10^6 Gt^2 for 20 regions in their solution. A valid question is whether this type of constraint is sufficient or whether it is possible to find better constraints for the inversion. It is known that local mass change estimates based on GRACE data depend on constraints that are applied during the least-squares inversion. A too small a-priori variance will over-constrain a regional mass change, while an a-priori variance that is too large will cause an increased approximation error in the solution. Hence, the goal should be to reduce the approximation errors and to ensure that the approximations are not biased towards the constraints. Bonin and Chambers (2013) use a simulation of the GrIS in order to optimize the single constraint during the inversion. Here we aim to use different constraints for different parts of the GrIS. As simulation we will make use of the IOM solution based on the RACMO2 model output that was provided for this study, which simulates surface mass balance changes on the GrIS. However, we also have to consider that the knowledge of the study area obtained by models such as RACMO2 and discharge measurements may be insufficient for a simulation. Consequently, we need to find an alternative method to determine the required constraints for the GrIS basins that is less dependent on priori information.

It has to be highlighted that when we say the model based simulation is used for determining the constraints, we do not use the mass changes from the simulation as constraints. Instead, we consider the variances of the modelled regional mass changes. In this way, we do not fit the GRACE approximation to the simulation but we only constrain the variances of the approximation to reduce the approximation error. We are also interested in the regions where the IOM shows different mass changes estimates from GRACE based estimates. In order to explain the difference, it is required to assess both the GRACE and IOM solutions. The GRACE solution can be wrong in some regions when the inversion approach is not capable to accurately extract the mass change signal. This can be verified through a simulation where we know the exact regional mass changes on the GrIS. The IOM solution is probably the best choice for creating the simulation.

For the IOM solutions, we will not investigate the RACMO2 model and the ice discharge estimates themselves. However, we will investigate the determination of the reference SMB and D which play an important role in the IOM solution. Previous IOM solutions estimate the reference D from historical data (Rignot et al., 2008). Since the historical data are incomplete in some regions, one has to assume a reference D in order to close the calculation of IOM (see the detailed discussion in section 3.2). This is reason to suspect the regional accuracy of the IOM solution when it shows different results compared with the GRACE based estimates. Furthermore, some studies apply the over uncertainty of the SMB model for the whole GrIS, e.g.: van den Broeke et al. (2009) and Sasgen et al. (2012), but the uncertainty of the SMB model is still unknown in regions. It could lead to under- or over-estimated regional uncertainty which can also cause the results to be different from other solutions. Hence it becomes necessary to re-evaluate the IOM solution in those regions.

1.4 Research questions

Based on the motivation described in section 1.3 we obtain the following research questions:

1) How can the variance information derived from an IOM solution help to get better constraints for the mascon inversion procedure?
2) How large are the differences between the GRACE mascon inversion results and the IOM results and how can they be explained?
3) How can we impose an alternative constraint on the GRACE mascon inversion procedure which depends only weakly on simulated mass changes?
4) How do our GRACE mascon inversion results compare to other published results?

1.5 Dissertation Structure

This thesis consists of 5 chapters. Chapter 2 is published in Geophysical Journal International in 2015, and it focuses on finding optimal constraints for different basins in the GrIS. In this chapter, we describe the approximation error when using the least-squares inversion approach. In order to minimize the approximation error appearing in the regional mass changes estimates for several GrIS basins as well as the coastal and the interior areas, we propose a method to solve the

multi-objective optimization problem of finding optimal constraint values for coastal and interior GrIS regions. A simulation based on the provided IOM solution is implemented to test the method.

Chapter 3 is published in The Cryosphere in 2016 where we discuss improved optimal constraints to determine rates of mass changes in 16 GrIS basins. Independent from that, we utilize the IOM method in which the surface mass changes estimates come from the RACMO2.3 model and where the ice discharge estimates are based on a survey of the ice thickness of the GrIS glaciers. We compare the two regional solutions in this chapter, and identify causes of the regional disagreement. A method was developed to validate the accuracy of the constrained least-squares inversion approach and to improve our GRACE solution by targeting the still existing approximation error. Finally, we also improve the IOM solution by using a correction of the historical discharge data based on modeled run-off.

The methods presented in chapter 2 and 3 require a priori information of the GrIS which may not be available in all basins with the required quality. In chapter 4 a so-called hierarchical constraint method is developed which uses the estimated mass changes in large (top-level) basins to constrain mass changes in smaller basins enclosed within the top-level basins. The method is based on the finding that top-level basins are less affected by approximation errors than small basins when they are constrained in the same way. We use this method to reduce approximation errors in the GRACE regional solutions with less dependence on prior knowledge about the ice mass changes and without the commonly used regularization term in the least-squares inversion method. The method is tested with a simulation based on the IOM solution and applied to the GRACE data for further validation.

We summarize the results obtained in this thesis in chapter 5 where the reader can also find recommendations for future studies on improving our methods and for applying our methods to other study regions.

Chapter 2

Optimization of regional constraints for estimating the Greenland mass balance with GRACE level-2 data

Z. Xu, E. Schrama, W. van der Wal

Published in *Geophysical Journal International*, Vol. 202, p. 381–393, 2015

Abstract

Data from the Gravity Recovery and Climate Experiment (GRACE) satellite mission can be used to estimate the mass change rate for separate drainage systems (DSs) of the Greenland Ice Sheet (GrIS). One approach to do so is by inversion of the level-2 spherical harmonic data to surface mass changes in predefined regions, or mascons. However, the inversion can be numerically unstable for some individual DSs. This occurs mainly for DSs with a small mass change signal that are located in the interior region of Greenland. In this study, we present a modified mascon inversion approach with an improved implementation of the constraint equations to obtain better estimates for individual DSs. We use separate constraints for mass change variability in the coastal zone, where run-off takes place, and for the ice sheet interior above 2000 m, where mass changes are smaller. A multi-objective optimization approach is used to find optimal prior variances for these two areas based on a simulation model. Correlations between adjacent DSs are suppressed when our optimized prior variances are used, while the mass balance estimates for the combination of the DSs that make up the GrIS above 2000 m are not affected significantly. The resulting mass balance estimates for some DSs in the interior are significantly improved compared to an inversion with a single constraint, as determined by a comparison with mass balance estimates from surface mass balance modelling and discharge measurements. The rate of mass change of the GrIS for the period of January 2003 to December 2012 is found to be −266.1 ± 17.2 Gt yr−1 in the coastal zone and areas below 2000 m, and +8.2 ± 8.6 Gt yr−1 in the interior region.

Key words: Inverse theory; Satellite gravimetry; Time variable gravity; Arctic region; Glaciology.

2.1. Introduction

The Gravity Recovery and Climate Experiment (GRACE) mission was launched in March 2002. Several studies have shown that ice mass decrease takes place on Greenland using data from the GRACE mission, (Schrama et al., 2011; Jacob et al., 2012, Sasgen et al., 2012; Shepherd et al., 2012; Barletta et al., 2013; Luthcke et al., 2013; Velicogna and Wahr, 2013; Schrama et al., 2014). An advantage of satellite gravimetry is that one can directly derive the total ice mass balance after correcting for glacial isostatic adjustment and atmospheric, oceanic and continental hydrology mass changes. An alternative method is to measure surface elevation change by satellite altimetry, in which case the density of the snowpack, the firn and the deeper ice must be known to estimate the mass change of an ice sheet. A drawback of satellite gravity measurements is the relatively low spatial resolution compared to satellite altimetry measurements (Zwally et al., 2005). The nature of satellite gravity in combination with the Post-processing is such that leakage effects can be seen in the maps of gravity change as a result of the signal spreading outside the source region (Chen et al., 2007; Velicogna and Wahr., 2005).

In order to deal with GRACE measurement error and leakage effects different approaches have been suggested. By means of averaging kernels, cf. Velicogna and Wahr (2005) and Swenson and Wahr (2007), one can minimize the combined GRACE measurement error and leakage effects to derive an average mass change for the GrIS or for larger sub-regions of the GrIS. Velicogna and Wahr (2005) assume an averaging function that is computed under the assumption of uniform mass change distributed in the coastal zone and zero in the interior of Greenland. However, several studies have indicated that neither the mass change in the coastal zone is evenly distributed nor mass change in the interior of Greenland is zero (Johannessen et al., 2005; van den Broeke et al., 2009). Furthermore, the averaging function for the GrIS extends to the neighboring land areas of northern Canada where mass changes also occur (Luthcke et al., 2013).

The mass concentration (mascon) methods described in Luthcke et al. (2006), Rowlands et al. (2010) and Luthcke et al. (2013) result in mass changes for a global set of mascons directly from the K-band ranging data from the GRACE satellites (the so-called level-1b data) and from information on the orbit of the GRACE satellites determined by GPS tracking and accelerometer measurements. In Luthcke et al. (2013) the mascons are taken to be $1^{\circ}\times1^{\circ}$ blocks. In order to suppress leakage and signal loss as a result of filtering, this approach considers GRACE data with the full GRACE noise covariance. The study of Luthcke et al. (2013) considers anisotropic constraints for neighboring mascons, and it assumes separate GrIS regions below and above 2000 meters. It is shown by Luthcke et al., (2013) that for smaller areas, i.e. for 34 sub-regions of the GrIS, meaningful regional mass changes still can be revealed from the GRACE data when proper constraints are introduced.

Other studies have estimated regional mass changes from the GRACE level-2 potential coefficients. Wouters et al. (2008) (hereafter W^{08}) implement a forward modelling approach similar to the mascon layout used by Luthcke et al (2013) whereby a fixed number of basin shaped regions on the GrIS are considered. For a discussion about the definition of GrIS basins see Rignot and Kanagaratnam (2006). Scaling factors for each region are adjusted iteratively to find a best match

between the equivalent water heights obtained from GRACE and their equivalent that follows from the forward model used by W[08]. Regional mass changes from this approach match the results from the mascon method described in Luthcke et al. (2006) as well as other studies, (Sasgen et al., 2012; Shepherd et al., 2012). A least-squares inversion approach described in Schrama and Wouters (2011) (hereafter SW[11]) also employs the basin shaped mascons, but it is different from the forward method as in W[08], since the least-squares approach is introduced. This approach improves the effectiveness of the approach of W[08] by reducing the required computing power. SW[11] show that the approximated regional mass balance agrees with the results retrieved via the mascon method in eight major GrIS drainage basins.

The least-squares inversion approach described in SW[11] leads to correlation between adjacent regions. An increase in mass loss in one region can be compensated by mass gain in adjacent regions so that the overall mass balance is unchanged. We will address the correlation effect in section 2.2 but here we discuss two solutions to this problem which are given in SW[11]. The first is that the solution becomes more stable when several adjacent regions are combined into a single estimate. The second solution is to implement regularization in the least-squares estimation (Tikhonov 1963), which means that the approximations of the regional mass changes are constrained by priori information. This solution is also referred to as constrained least-squares adjustment (SW[11]). With the second approach, the question is which values should be used as constraint. When the constraints are too tight the regional mass change estimates are biased towards a priori information. On the other hand, the instability can remain in regions if the constraint is too loose. SW[11] applied a loose constraint by assuming that the prior variance imposed on each basin is less than 10^6 relative to the variance of the EWH observation. In SW[11] several basin configurations were considered for the GrIS. The 13-basin configuration where the area above 2000 m on the GrIS was taken as one mascon was preferred in that study because the inter-region correlation was suppressed compared to the 20-basin solution.

To determine the optimal prior variances for the 20-region configuration, Bonin and Chambers (2013) (hereafter BC[13]) implemented the constrained least-squares approach assuming one prior variance (referred to as process noise in their study) for 16 GrIS sub-areas and one for mascons in the surrounding ocean as well as in northern Canada. In BC[13], the constraint variance is optimized by means of a simulation model based on the annual elevation change rate found by Zwally et al. (2005). However, according to BC[13], the mass changes estimated for some regions still contain noticeable errors. We will discuss these errors when applying the same optimal prior variance as constraint in section 2.2. Thus a single constraint for all regions in Greenland yields suboptimal results in least-squares inverted GRACE level 2 data. Another study of constraining the inversion approach using simulation is that of Baur and Sneeuw (2011), in which point masses are used instead of basin shaped mascons. In Baur and Sneeuw (2011), the approximation norm and the residual norm associated with a series of constraint are compared in a L-curve (Hansen, 1992) and the one in the “corner” of the L-curve is considered to be the optimal.

The goal of this paper is to build on SW[11] and BC[13] and to investigate whether an alternative constraint model for the basin shaped mascons can be justified that results in improved mass change

estimates for individual regions

The inversion modelling approach from SW[11] is described in section 2.2. We improve the regional mass balance approximation, in particular in the GrIS interior, by assuming separate constraints for regions above and below 2000 m. Optimal prior variances for different regions are found by applying the inversion approach to simulated monthly mass changes over the GrIS. In this simulation approach, discussed in section 2.3, we rely on RACMO2 model output (Ettema et al., 2009) and satellite radar interferometry observations of the ice discharge (Rignot and Kanagaratnam 2006). In section 2.4 we will introduce an optimization procedure for prior variances for different GrIS regions by searching for the optimal combinations using a genetic algorithm. In section 2.5, we will apply the optimal prior variances in the least-squares inversion modelling approach, and discuss the effect on regional mass changes from GRACE level-2 data. The conclusions are summarized in Section 2.6.

2.2. Inverse modelling of GrIS regional mass changes

The GRACE derived monthly geo-potential changes are represented by potential coefficients. In Wahr et al. (1998) it is shown how monthly geo-potential changes can be converted into surface mass changes expressed in water equivalent thickness under the assumption that one takes away the effects of tides, air pressure loading, mass changes in the ocean, and glacial isostatic adjustment. The inverse modelling approach used here aims at representing the equivalent water changes that follow from Wahr et al. (1998) by average water equivalent changes in predefined regions within the GrIS and the surrounding areas.

A sensible choice for obtaining predefined regions is to divide the GrIS into regions according to their natural drainage system (DS). Here we follow the definition of the DS described in Zwally et al. (2011) so that we arrive at an 8-region layout (figure. 2.1). In addition, we divide each DS at the 2000-meter elevation contour, with the interior region being the one above 2000 m, cf. Thomas et al. (2001), W[08], SW[11] and BC[13]. SW[11] compared multiple layouts for the GrIS as well as the surrounding regions which are Ellesmere Island, Baffin Island, Iceland and Svalbard (EBIS). When considering the GrIS as one single region SW[11] found a mass loss of -150 $Gt \cdot yr^{-1}$ between 2003 and 2010. Their conclusion was that a single mascon results in underestimated mass changes for the GrIS compared to other studies using GRACE data (Schrama and Wouters, 2011). The accuracy of the approximation in SW[11] was improved by applying a 20-region setup which separated the GrIS into 8 DS each divided in a region above and below 2000 m elevation. EBIS areas were treated as 4 separate regions as well. With this configuration SW[11] found an annual mass loss rate of around -250 $Gt \cdot yr^{-1}$ which agrees with other studies. So when using the least-squares inversion approach, it is also possible to approximate the GrIS mass changes in small regions while providing reasonable estimates of the mass change for the whole GrIS. However, when using the GRACE level-2 potential coefficients, the spatial resolution is limited by the maximum degree and order. In this study we use the CSR GRACE coefficients that are truncated at maximum degree and order 60. Therefore, regional mass balances derived from these truncated GRACE level 2 data should not rely on sub regions that are too small. In this study we will use the same number of sub-regions

as SW[11]. Moreover, compared to other region layouts, as described in (Luthcke et al., 2013), we use a more conservative 2000 m divide. The GRACE EWH map used in this study has a spatial resolution of 1° which is close to a 110×110 km square on the equator. In our layout, a grid cell is considered as interior only if 80% of the area of the grid cell has an altitude higher than 2000 m. We find that only 6 grid cells in DS 5 are above 2000 m, so in our layout we chose not to separate DS 5. W[08] and SW[11] found that the mass changes above the GrIS observed by GRACE contain leakage from the EBIS areas which is the reason for including these areas in the inversion. Overall, as depicted in figure 2.1, we define 15 GrIS regions and 4 EBIS regions.

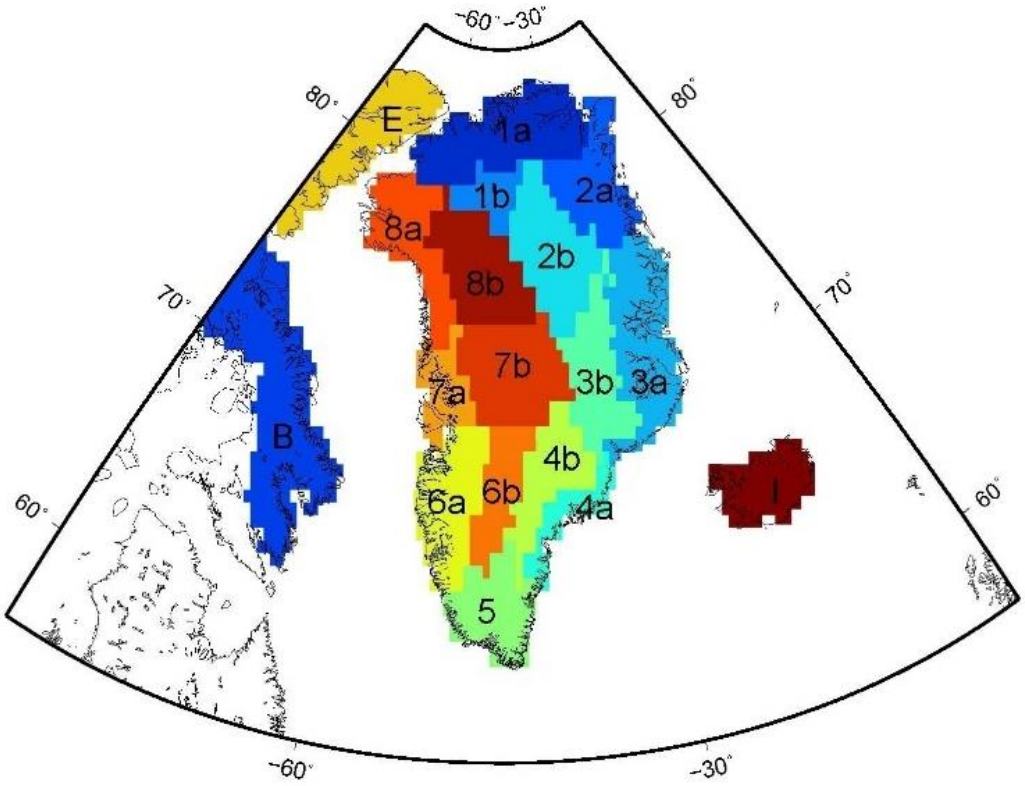

Figure 2.1: Drainage system divides according to Zwally et al. (2012). The digits are the id's of the drainage basins. The sub-region is marked by the character after the decimal. The characters "a" and "b" refer to the GrIS margin and interior regions, respectively. Note that in this figure Svalbard is not displayed but it is included in the 19-region layout.

In order to implement the method, we first assume a uniformly distributed water layer with unit thickness within each region, i.e. $f_k(\theta,\lambda)$=1 when $[\theta,\lambda]$ is within the domain of the region and 0 outside, where the subscript k=1, 2, 3⋯n indicates each region. We convert the mass distribution f_k into potential coefficients up to degree and order 60 which are filtered by an isotropic Gaussian filter as described in Swenson and Wahr (2002) with half width $r_{1/2}$=300 km. Then we convert the coefficients to EWH in the spatial domain and order the values as a column vector, which becomes the influence function $g_k(f_k)$. Both SW[11] and BC[13] have discussed the consequences of using

different half widths in the inversion approach. A half width of $r_{1/2}$=300 km was found in SW[11] and BC[13] to be the best compromise (compared to 0 km, 500 km and 700 km) between suppressing the noise in GRACE data and being able to compute mass changes in our configuration of regions.

We construct a matrix $\mathbf{H} = [g_1, g_2, \dots, g_n]$ and a vector of scaling factors $\mathbf{x} = [a_1, a_2, \dots, a_n]^T$ associated with the assumed mass distribution f_k, so that:

$$\mathbf{y} = \mathbf{H}\mathbf{x} + \boldsymbol{\varepsilon} \tag{2.1}$$

The vector $\boldsymbol{\varepsilon}$ contains the misclosures between the observations y and the model $\mathbf{H}\mathbf{x}$. y contains the global mass changes ordered as a column vector, which in this study is either derived from the simulation model (see Section 2.3) or from the GRACE observations (see Section 2.5). The approximation can be found by minimizing the sum of the squared residuals. To do so, we solve Eq. (2.1) using a least-squares approach. As in SW[11], we define the cost function for the least-squares approach as:

$$J = \boldsymbol{\varepsilon}^T \boldsymbol{\varepsilon} \tag{2.2}$$

the minimization of which yields, under the assumption of a uniform variance of all observations in the vector $\mathbf{y}$,

$$\hat{\mathbf{x}} = (\mathbf{H}^T\mathbf{H})^{-1}\mathbf{H}^T\mathbf{y} \tag{2.3}$$

Eq. (2.3) is an unconstrained solution because no other information was considered than the observations. As a result, the residuals are minimized for the entire GrIS but the solution is numerically unstable. The numerical instability manifests itself in the form of anti-correlation between neighboring regions so that we can see the typical high-low-high patterns as demonstrated by BC[13], also cf. Baur and Sneeuw (2011). Such a pattern will be called anti-correlation error in the following. One way to deal with this problem is to average the mass changes in the anti-correlated neighboring regions, e.g. by combining the area above and below 2000 m in one drainage system (Sasgen et al., 2012) or by combining the interior regions cf. SW[11]. Although the errors are reduced by combining regions, they still exist in sub areas. For instance, in SW[11], when separating each drainage area by the 2000 m elevation contour, the approximated mass balance of the entire GrIS is obtained with a relatively low uncertainty, i.e. -201.4±21.0 Gt·yr^{-1} during 2003–2010. However, the uncertainties for separated GrIS margin and interior areas became larger, i.e. -263.3±55.6 Gt·yr^{-1} and 62.0±46.5 Gt·yr^{-1} respectively.

The regional instability can be reduced by introducing prior variances as constraints on the mass changes for each region, also known as the Tikhonov regularization, (Tikhonov, 1963). Note that in general Tikhonov regularization, $\mathbf{P} = \lambda\mathbf{R}$ where $\mathbf{R}$ is the regularization matrix and λ is the regularization parameter. In this study we assume that in the prior matrix, all the regions are equally weighted, yielding $\mathbf{R} = \mathbf{I}$. Also we use the prior variance σ^2 of the regional mass variations in each regions as the regularization parameter so that the constraint can be written as $\mathbf{P} = \sigma^2\mathbf{I}$, and the cost function becomes:

$$J = (\boldsymbol{\varepsilon}^T\boldsymbol{\varepsilon} + \mathbf{x}^T\mathbf{P}^{-1}\mathbf{x}) \tag{2.4}$$

where the residual norm $\boldsymbol{\varepsilon}^T\boldsymbol{\varepsilon}$ is associated with the observations with unit weight and the approximation norm $\mathbf{x}^T\mathbf{P}^{-1}\mathbf{x}$ contains the priori information. With this information we restrict the variance of the regional scaling factor $\mathbf{x}$, in order to reduce the anti-correlation errors cf. SW[11]. In this case Eq. (2.3) becomes:

$$\hat{\mathbf{x}} = (\mathbf{H}^T\mathbf{H} + \mathbf{P}^{-1})^{-1}\mathbf{H}^T\mathbf{y} \quad \textbf{(2.5)}$$

All regions are considered to have the same prior variance in SW[11] and BC[13]. However, it has been found in BC[13] that with the optimized prior variance σ^2, the anti-correlation still remained in some over-sensitive regions that have a higher than average mass change per grid cell. For instance, in DS 6, the area of the coastal region is around 1.6×10^5 km^2 and for the interior region it is around 1.2×10^5 km^2. In these two similar sized regions, the mass change rates are significantly different. According to the modelling of the surface mass balance, the mass changes in this interior region are smaller than in the margin region (Ettema et al. 2009; Fettweis et al. 2011). Also in the same DS, from GRACE data, Luthcke et al., (2013) found a much lower mass change rate in the interior and much more mass loss near the margin by using the direct mascon approach with geolocatable constraints for the mascons below and above 2000 m. However, when applying the same constraint as in BC[13], the mass change estimates for DS 6 from GRACE data were -8.9±4 Gt·yr^{-1} and -9.8±3.7 Gt·yr^{-1}, for the margin and for interior regions, respectively. So the mass balance approximations in both regions are likely in error because the interior region should lose less mass than the margin because run-off is smaller. BC[13] quantified this type of errors with a simulation method and found that in DS 6, when using the same optimal constraint, the regional mass estimates were anti-correlated, and the associated error was –8.4 Gt·yr^{-1} for the GrIS margin area and +11.2 Gt·yr^{-1} for the interior region. Hence in order to further improve the least-squares approximation in regions, the constraint **P** matrix will be composed of a group of non-identical prior variances. In our case an optimal **P** is based on a full time series simulation model which will be described in section 2.3.

2.3. Simulation of the GrIS mass balance

In this section we introduce a simulation model that produces a reasonable representation of monthly mass changes on Greenland and its surrounding areas so that optimal prior constraint variances can be determined. For this purpose, we use the RACMO2 model and discharge data to simulate 108 months (January 2003 to April 2012) of surface mass changes on the spatial domain with a resolution of 1º x 1º. RACMO2 estimates the SMB by modelling the regional precipitation, runoff, refreezing and evaporation/sublimation and is accurate to within ~18%, according to Sasgen et al., (2012). To compute the total mass balance for Greenland we also use ice discharge data that have been derived from SAR data (Rignot and Kanagaratnam 2006) to yield a discharge mass flux at the glacier boundary. The remainder areas of the world are set to zeroes. This model describes the mass conservation of GrIS and will be referred to as input-output model (IOM) in the following, cf. (Shepherd et al., 2012).

In figure 2.2(a), the IOM output is in the form of the gridded annual EWH change rate for

Greenland and the surrounding EBIS regions. We convolve the gridded mass distribution over the Earth's surface and obtain the potential coefficients in response to this distribution up to degree l=60. Additionally, the noise in GRACE level-2 data potentially increases the variability of the monthly regional mass balance. Therefore we also simulate the GRACE noise by applying the approach of BC[13]. In this approach the noise is isolated from the GRACE data by removing from it all known components, including the continental hydrology, all the glacier regions and GIA, using the following external information:

1. The model output from the Global Land Data Assimilation System (Rodell et al., 2004) (GLDAS) using the Noah Land Surface Model.
2. Annual mass changes on land glaciers outside the GrIS from Jacob et al. (2012).
3. The GrIS regional mass changes from Sasgen et al. (2012).
4. The GIA model of Paulson et al. (2007).

This information is converted into monthly potential coefficients complete up to degree and order 60 and removed from GRACE potential coefficients. From the remaining coefficients, a covariance matrix is constructed, which is subsequently used to generate random potential coefficients according to the procedure in appendix A of BC[13]. In this study, we simulate the GRACE noise for every month, then add it to the potential coefficients of the IOM model. We apply a Gaussian filter with a smoothing radius $r_{1/2}$=300 km on the combined coefficients and calculate the EWH map for the complete simulation model. The simulation model in terms of annual EWH change is shown in figure 2.2(b).

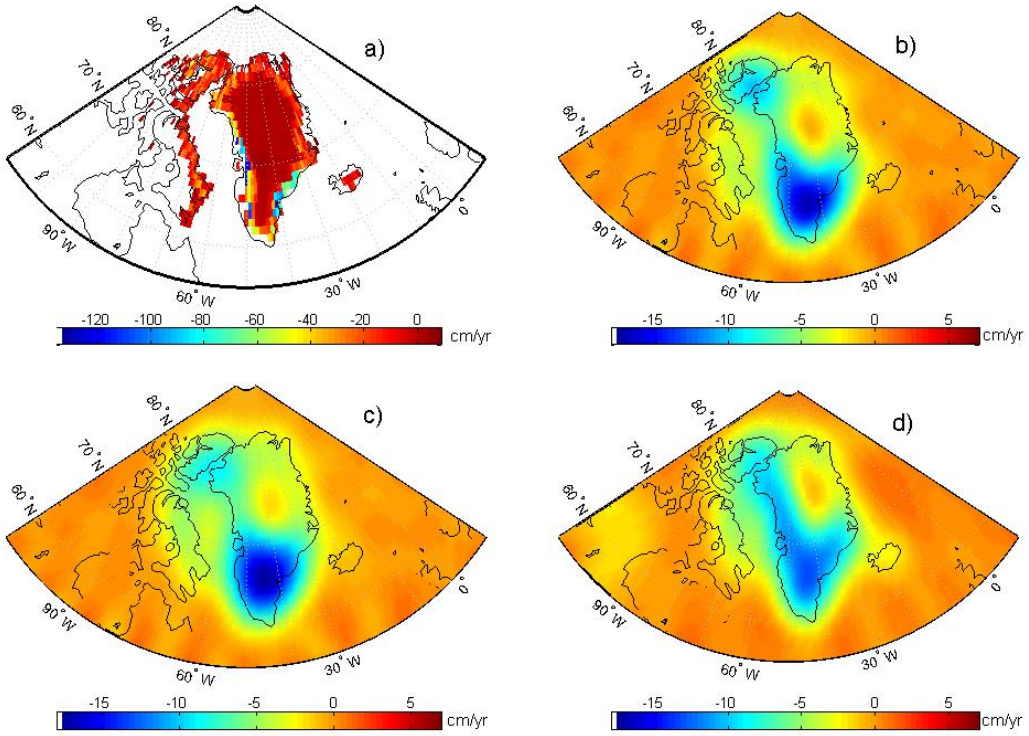

Figure 2.2: Mass change simulation model results based on the IOM. a) shows the gridded EWH change trend on a 1ºx1º grid for the time period January 2003 to April 2012. The unit is cm/yr. b) shows EWH change trend of the simulation model **y**. The simulation is based on a) after spherical harmonic analysis and synthesis up to degree and order 60 and Gaussian filtering ($r_{1/2}$=300 km), and also includes noise in the GRACE data. The average EWH change trend for each region computed from the IOM is $\mathbf{x}'$, and the associated simulated GRACE data (after smoothing) $\mathbf{y}' = \mathbf{H}\mathbf{x}'$ is shown in c). d) shows the annual EWH trend retrieved from the GRACE data for the same time span.

Due to the uncertainty in the RACMO2 and discharge estimates, there will be regional differences between the simulation model and GRACE observations as can be seen in figure 2.2(b) and figure 2.2(d), but we use the simulation only as a reasonable mass change signal to derive constraints. In the next section we will use the above described simulation model to optimize the prior covariance matrix **P** in our inversion algorithm.

2.4. Optimization of the constraints in least-squares approach

In order to find the optimal covariance matrix **P**, we apply Eq. (2.5), replacing **y** by simulated data. Since $\hat{\mathbf{x}}$ is supposed to represent the average regional mass balances, we compare them to the regionally averaged simulated data without noise, being just the IOM model output averaged by region, see figure 2.2(c). To distinguish from the simulated data, we label the regionally averaged IOM model output with $\mathbf{y}'$. Note that the GRACE noise is not included in $\mathbf{y}'$.

2.4.1. Optimization of constraint

The optimal constraint covariance matrix **P** is achieved when the differences between the approximation $\mathbf{H}\hat{\mathbf{x}}$ and the averaged model $\mathbf{y}'$ reaches a minimum. Using Eq. (2.5) the difference is a function of the prior covariance matrix **P**:

$$f(\mathbf{P}) = \mathbf{y}' - \mathbf{H}(\mathbf{H}^{\mathrm{T}}\mathbf{H} + \mathbf{P}^{-1})^{-1}\mathbf{H}^{\mathrm{T}}\mathbf{y} \qquad \textbf{(2.6)}$$

Note that Eq. (2.6) is different from the cost function in Eq. (2.4) for the least-squares inversion, because $\mathbf{y}'$ contains only the regionally averaged IOM model output, which means that $f(\mathbf{P})$ is not equivalent to the residual $\boldsymbol{\varepsilon}$ from the least-squares approach.

BC[13] considered a uniform prior variance factor σ^2 for all regions to form the **P** matrix (which we denote as constraint matrix $\mathbf{P}_1$), so that $\sigma_1^2 = \sigma_2^2 = \cdots = \sigma_n^2 = \sigma^2$ and $\mathbf{P}_1 = \sigma^2\mathbf{I}$. Here we consider different variances on the diagonal of the P matrix. We use the notation $\mathbf{P}_3$ to define our **P** matrix because we define 3 prior variances factors. To form the $\mathbf{P}_3$ matrix, for the regions below 2000 m we define the associated prior variance elements as $\sigma_{1\ldots8}^2 = \sigma_d^2$. For the regions above 2000 m, a different prior variance is applied, i.e. $\sigma_{9\ldots15}^2 = \sigma_u^2$ and we use $\sigma_{16\ldots19}^2 = \sigma_{EBIS}^2$ to describe the prior variance of the EBIS areas.

We evaluate Eq. (2.6) and take the Root Mean Squares (RMS) difference to the simulation as the first objective function:

$$G_1 = \sqrt{\frac{\iint_{\Omega} f^2(\mathbf{P})}{A}} \qquad \textbf{(2.7)}$$

Ω defines the area which we use for comparison, between 40°–85°N and 255°–385°W, and A is the total surface area of Ω.

Since the evaluation is based on the trend difference during the simulated time span, it only describes the long-term behavior of the mass change rate in each region. As discussed in W[08] and BC[13], the inter-region correlation should also be taken into account for assessing the quality of approximated solutions. Hence, we introduce a second objective function during the optimization:

$$G_2 = \sqrt{\frac{\sum_{i,j=1}^{n}\left(r_{ij}^2 - \hat{r}_{ij}^2\right)^2}{n^2}} \qquad \textbf{(2.8)}$$

It is the RMS of the difference between the inter-region correlation coefficient matrix for the simulation model $\mathbf{R} = \left[r_{ij}^2\right]$ and the inter-region correlation coefficient matrix for the approximation $\widehat{\mathbf{R}} = [\hat{r}_{ij}^2]$, where r_{ij}^2 and $\hat{r}_{ij}^2$ are the correlation coefficients between the time series

of approximated monthly regional mass changes in region i and region j from 2003 to 2012, in the simulation and the approximation respectively. They state the correlation in monthly mass changes between two regions. n is the total number of mascon regions in the least-squares inversion. Examples of the inter-region correlation can be found in figure 2.5, which will be discussed in section 2.4.4.

2.4.2. Evaluation of objective functions

Firstly, we evaluate the objective function Eq. (2.7) and Eq. (2.8) using a priori covariance matrix $\mathbf{P}_1$ as the constraint where varies σ^2 from 0.001 m^2 to 1000 m^2. We find that when σ^2=1000 m^2 the influence of $\mathbf{P}_1$on the approximation in Eq. (2.5) becomes negligible, so that an unconstrained approximation is obtained. The corresponding RMS difference of the EWH trend G_1=0.44 cm•yr^{-1}. For σ^2 < 1 m^2 G_1 is larger than the unconstrained solution thus these variances are rejected. The objective function as a function of the prior variance is shown in figure 2.3(a). As can be seen in this figure, the minimum of the objective function G_1=0.35 cm•yr^{-1} is achieved when σ^2=3 m^2. However, we find the minimum of the inter-region correlation difference G_2=0.44 when σ^2=5 m^2. Also when we gradually increase the value of σ^2 from 3 m^2 to 5 m^2, the evaluation of G_1 diverges from the minimum while the evaluation of G_2 is converging towards to its minimum. Thus, there is a trade-off between these two objective functions within the range where the optimal σ^2 is mostly likely to be found. In this study, in order to choose from two values for the prior variance which both yield the optimal scores but for different objective functions, we assess the overall return when altering the solution. For instance, we chose σ^2=5 m^2 as the optimal solution for $\mathbf{P}_1$, because when comparing to σ^2=3 m^2, the evaluation of G_2 is reduced by 6% while G_1 is increased by only 1%. One may argue that the differences are small. However, the objective functions G_1 and G_2 are computed as spatial averages, and when the averaged difference is integrated over the indicated region with a total area of approximately 2.6×10^7 km^2, significant differences can be found. We will discuss the spatial differences in section 2.4.3.

The optimization process becomes more complicated when $\mathbf{P}_3$ is used as the constraint covariance matrix, since the dimension of the search space of $\mathbf{P}_3$ increases by 2 compared to $\mathbf{P}_1$. Manually testing each possible $\mathbf{P}_3$ to locate the minimum with both objective functions turns out to be time consuming. For this reason, we employ a genetic algorithm (GA) technique, the Non-Dominating Sorting Genetic Algorithm (NSGA-II) (Deb et al., 2002), that is built-in the Matlab optimization toolbox, version 2012. NSGA-II is a fast multi-objective optimization algorithm that is designed to find the optimal solution in case there are multiple objectives that need to be minimized/maximized and also allows easy extension of the method to more than 3 prior constraints. NSGA-II iteratively evaluates and updates the solution. In GA the term population is defined as a group of solutions each consisting of different combinations of variables. In this study these variables are the variance factors in $\mathbf{P}_3$. In the NSGA-II algorithm the population is evaluated at every iteration through the objective functions, and the populations are ranked based on the outcome. The NSGA-II algorithm ranks the population by applying the "*non-domination*" rule. If an individual is worse than at least one other individual regarding all the objectives, then it is

dominated by those individuals. Individuals which are not dominated by any others are the dominating individuals and the collection of the dominating individuals is Pareto front. For instance, in figure 2.3(a) when using the covariance matrix $\mathbf{P}_1$ as the constraint and letting σ^2=3 m^2, 5 m^2 and 20 m^2, we find that G_1 is 0.35 cm, 0.36 cm, 0.40 cm and G_2 is 0.51, 0.45, 0.49, respectively. The solution σ^2=20 m^2 yields the largest approximation error in both objective functions, so it is a dominated solution and will not be selected. Although σ^2=3 m^2 is a better solution than σ^2=5 m^2 regarding the cost function G_1, the opposite is true when considering the cost function G_2. So σ^2=3 m^2 and σ^2=5 m^2 are both dominating solutions. In NSGA-II, during every generation, the individuals on the Pareto fronts are given the top rank, while the individuals on the second best front are given the second rank, and so on. NSGA-II repeats this process until the entire population in the current generation is ranked.

Individuals with parents with high rank will provide the information used for creating a new population in the next generation, also referred to as children. For instances, if the covariance matrix $\mathbf{P}_i^t$ and $\mathbf{P}_j^t$ are the parents at generation t, then in generation t+1, NSGA-II will create a new $\mathbf{P}^{t+1}$ which is identical to either $\mathbf{P}_i^t$ or $\mathbf{P}_j^t$ in part of the dimensions. In addition, we apply a mutation in one or more of the dimensions during the process of generating children, in order to avoid the solutions converging to a local minimum or maximum. NSGA-II will stop when it reaches the maximum specified number of generations. We also restrict the value of σ in $\mathbf{P}_3$ to fall in the range [0.001, 1000]. Moreover, we define the size of population to be 100 and the maximum number of generations to be 50. During the optimization, we found that the size of the population and the maximum number of generations is sufficient to find the global optimum. The final Pareto front, consisting of 70 different cases of $\mathbf{P}_3$, is shown in figure 2.3(b) in which the evaluations of the objective functions are normalized to a range of 0–1. After normalization, the minimum and maximum evaluations of G_1 and G_2 become 0 and 1, respectively.

In figure 2.3(b) it can be observed that these solutions naturally fall into two distinguishable categories. The solutions within the pink box show a small change in the normalized objective function G_1, but a large change in the normalized cost function G_2. Two points in this group that yield the local minimum in either G_1 or G_2 are shown by solid red circles, i.e. A_1 and A_2. For G_1 the scores of these two points are ${G_1}^{A_1}$=0 and ${G_1}^{A_2}$=0.13. On the other hand, the evaluations of G_2 are ${G_2}^{A_1}$=1 and ${G_2}^{A_2}$=0.4. The slope of the normalized vector $\overrightarrow{A_1A_2}$ is around -0.2, which indicates that if we chose A_2 over A_1, we gain 1-unit improvement in G_2 while losing 0.2 unit of G_1. Because of the relatively small increase in G_1, we choose the solution $\mathbf{P}_3$ associated with the point A_2 to be the local optimal solution in this group.

Similarly, for another group, we identify the boundary points B_1 and B_2 inside the green box, with scores of ${G_1}^{B_1}$=0.23 and ${G_1}^{B_2}$=1, ${G_2}^{B_1}$=0.38 and ${G_2}^{B_2}$=0. The slope of the normalized vector $\overrightarrow{B_1B_2}$ is -2.0, which means that when we move from point B_1 to point B_2, in order to reduce G_2 by 1 unit we will increase G_1 by 2.0 units. Regarding the overall return B_1 is better than B_2 in this group. Thus, we have found two local optimal solutions for $\mathbf{P}_3$, A_2 and B_1. If we select B_1 over A_2, G_2 is reduced by only 0.02 while G_1 is increased by 0.2. Thus A_2 is selected to be the optimal point,

and the associated solution is $\mathbf{P}_3$ with the diagonal elements [10.0, 0.1, 1.9] m^2.

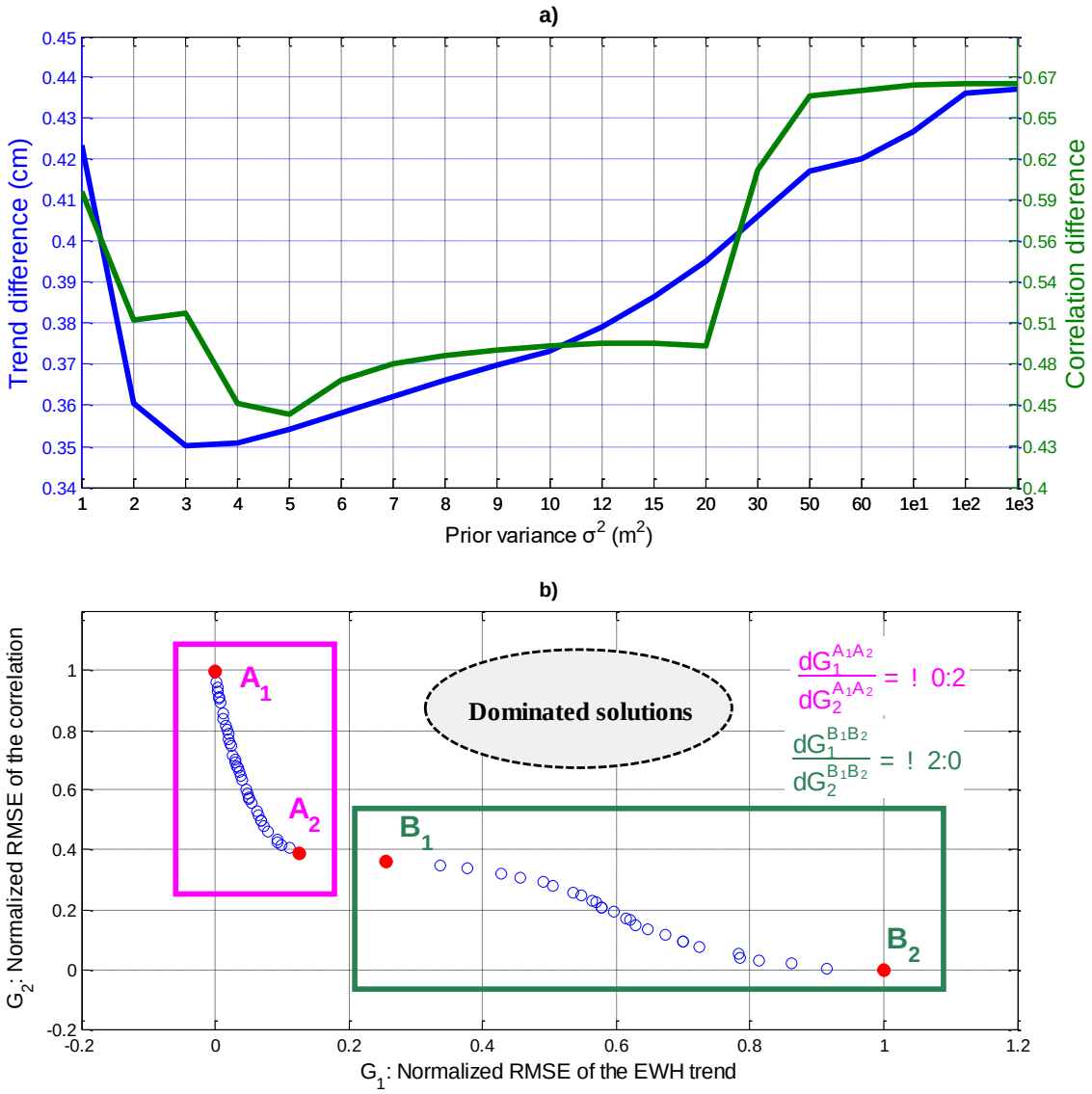

Figure 2.3 a) the blue line shows the RMS differences in the annual trend between the approximated solution and the simulation model, i.e. the objective function G_1. The green line shows the objective function G_2 which is the RMS difference of the inter-region correlation matrix for the simulation and for the approximation.
b) shows the performance of all the dominating solutions $\mathbf{P}_3$ (blue circles) along the Pareto front with respect to the objective functions G_1 (x-axis) and G_2 (y-axis). The values are normalized to a range of 0–1. The dominating solutions are categorized into two groups, the dominating solutions in the pink box are better for the objective function G_1; the green box contains the solutions that yield a smaller objective function G_2. For each box, we compute the slope of the vector from the upper-left point to the bottom right point, marked by solid red circles.

2.4.3. Trend differences

This section discusses the differences between the approximated simulation and the simulation, or G_1 in Eq. (2.7). Note that we do not consider the uncertainty in the RACMO2 and discharge data when we use them to create the simulation model as a reasonable benchmark. The actual uncertainty of the simulation model is discussed in section 2.5. The uncertainty of the trend in the simulation and approximated simulation only reflects the uncertainty caused by linear interpolation for a 95% confidence interval.

In the simulation model a mass change of -249.7±4.9 Gt·yr^{-1} is found for the entire GrIS (15 regions) from January 2003 to April 2012. The mass change trends from the approximation are -242.2±4.3 Gt·yr^{-1}, -247.5±4.3 Gt·yr^{-1} and -251.2±4.3 Gt·yr^{-1} when the least-squares inversion approach is unconstrained and constrained using the optimal $\mathbf{P}_1$ and constrained using the optimal $\mathbf{P}_3$, respectively. All three approximations are similar for the whole GrIS, however the differences between regional mass change trends are significant.

In figure 2.4, we compare the EWH rate differences between the approximations and the simulation model. We find that the differences are spatially anti-correlated. For example, in figure 2.4(a) where the approximation is the unconstrained solution, one can see underestimated mass loss rate in the west coastal regions. To compensate the insufficient mass loss, the least-squares approach increases the mass loss in adjacent regions, which leads to overestimated mass loss in the neighboring Baffin Island region and over-estimated mass gain in the adjacent interior regions (both result in negative differences). This manifestation of the anti-correlation error during the least-squares inversion can be quantified by comparing with the simulation model. In table 2.1 we find that the annual mass change trend in region 6a and 7a (margin of western GrIS) is -52.9±1.7 Gt·yr^{-1}and -16.6±0.4 Gt·yr^{-1} in the simulation model, whereas the unconstrained least-squares solution gives -64.3±1.9 Gt·yr^{-1} and -32.1±0.4 Gt·yr^{-1}, respectively. Inland we can see from this table a considerable mass gain in the approximation for both region 6b and region 7b, i.e. 17.1±0.4 Gt·yr^{-1} and 12.2±0.2 Gt·yr^{-1} while in the simulation model there is only 1.0±0.3 Gt·yr^{-1} and 2.8±0.2 Gt·yr^{-1} mass gain in regions 6b and region 7b respectively.

When we use the optimal $\mathbf{P}_1$ as constraint, and compare the EWH differences in figure 2.4(b), we find that the approximated mass change rate for the western coastal regions and the interior regions are closer to the simulation model, see table 2.1. However, anti-correlation errors still exist in the interior. For instance, in region 7a and 7b the differences with respect to the simulation are -7.3 Gt·yr^{-1} and 6.2 Gt·yr^{-1}.

Apparently, one can easily cancel the errors by combining DS number 7a and 7b. However, this lowers the resolution of the approximation, so we apply the optimal $\mathbf{P}_3$ matrix as constraint instead. After introducing a specific constraint for the interior regions with the optimal $\mathbf{P}_3$ matrix, one can clearly see that the EWH rate differences with respect to the simulation model, figure 2.4(c), are reduced compared to figure 2.4(b), although the approximated mass change rates are still higher in region 7b and lower in region 7a. However, the error in this DS with respect to the simulation value is reduced to 10% in the margin and 14% in the interior.

The benefits of applying the constraint $\mathbf{P_3}$ can also be seen when we combine all the regions above 2000 m. As shown in table 2.1, in the simulation model the mass slowly accumulates during the time span with a rate of 9.0±0.6 Gt·yr^{-1}. This rate is poorly approximated with a value of 47.8±0.2 Gt·yr^{-1} when no constraint is used, and 21.8±0.5 Gt·yr^{-1} when the constraint $\mathbf{P_1}$ is used. Our main conclusion is that we obtain the best approximated rate of 7.6±0.1 Gt·yr^{-1} for the combined interior regions when using $\mathbf{P_3}$.

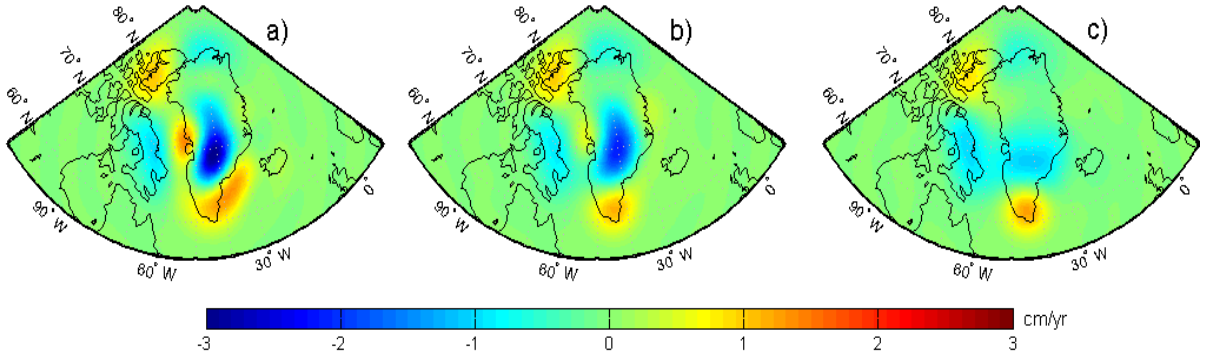

Figure 2.4: The linear trend of the approximated solutions after least-squares inversion minus the trend from the simulation (based on the RACMO2 model output and the discharge data). Three strategies are used for the constraints. a) unconstrained, b) using the optimal $\mathbf{P_1}$ as constraint and c) using the optimal $\mathbf{P_3}$ as the constraint. The unit is cm per year.

Table 2.1: The trend in monthly mass changes for all regions in Gt·yr^{-1}. The uncertainties only refer to the uncertainty caused by linear interpolation for a 95% confidence interval. For some regions, the uncertainty is 0.0 due to rounding. "*IOM*" refers to the solutions derived from the IOM model, and the symbol "NC" means that no constraint is applied. Similarly, P_1 and P_3 indicate the scenarios in which the optimal prior covariance matrix $\mathbf{P_1}$ and $\mathbf{P_3}$are applied respectively. Note that the mass change rates in this table refers to the time span from 2003 to 2012.

	GrIS region layout (Zwally et al., 2012)							
	DS 1	DS 2	DS 3	DS 4	DS 5	DS 6	DS 7	DS 8
	region 1a	region 2a	region 3a	region 4a	region 5	region 6a	region 7a	region 8a
IOM	-23.7±0.5	-10.6±0.5	-34.3±0.7	-62.4±1.1	-32.1±0.6	-52.9±1.7	-16.6±0.4	-26.0±1.2
NC	-11.6±0.3	-12.1±0.6	-25.4±0.6	-86.4±1.0	-30.1±0.6	-64.3±1.9	-32.1±0.4	-28.4±0.9
$\mathbf{P_1}$	-18.9±0.3	-11.4±0.6	-30.0±0.6	-72.0±0.8	-33.2±0.6	-51.0±1.7	-23.9±0.3	-28.9±0.9
$\mathbf{P_3}$	-21.2±0.4	-11.6±0.6	-31.9±0.6	-62.0±0.9	-34.8±0.6	-49.3±1.9	-18.3±0.4	-29.8±1.0
	region 1b	region 2b	region 3b	region 4b		region 6b	region 7b	region 8b
IOM	0.4±0.1	3.0±0.1	0.7±0.1	0.3±0.1		1.0±0.3	2.8±0.2	0.8±0.1
NC	-7.6±0.1	3.2±0.3	-4.5±0.1	19.5±0.4		17.1±0.4	12.2±0.2	7.9±0.3
$\mathbf{P_1}$	-3.8±0.1	3.0±0.2	3.5±0.1	5.0±0.1		2.1±0.2	9.0±0.2	3.1±0.2
$\mathbf{P_3}$	-0.1±0.0	2.2±0.1	0.6±0.0	0.4±0.0		0.5±0.0	3.2±0.0	0.9±0.0
	EBIS regions				Combined areas			
	Svalbard island	Elsmere island	Baffin island	Iceland	<2000 m	≥2000 m	GrIS	GrIS+EBIS
IOM	-1.2±0.3	-36.0±1.2	-47.2±1.4	-6.0±0.2	-258.7±4.7	9.0±0.6	-249.7±4.9	-340.1±5.5
NC	-0.5±0.3	-29.8±1.0	-51.7±1.5	-4.4±0.1	-290.2±4.5	47.8±0.6	-242.4±4.3	-328±5.0
$\mathbf{P_1}$	-0.4±0.3	-30.5±1.0	-50.6±1.4	-3.6±0.1	-269.4±4.2	21.8±0.5	-247.5±4.3	-332.6±9.4
$\mathbf{P_3}$	-0.4±0.3	-29.4±1.0	-49.3±1.4	-3.0±0.1	-258.8±4.4	7.6±0.1	-251.2±4.3	-333±4.9

2.4.4. Inter-region correlation of the monthly mass balance

We also assess the approximations by comparing the inter-region correlations. As in Eq. (2.8), we compute the correlation coefficient matrix **R** of the monthly regional mass change approximations using different constraints. In figure 2.5, we plot the inter-region correlation coefficients of matrix **R**, with each pixel in these plots referring to the correlation between the monthly mass changes for region *i* on the x-axis and region *j* on the y-axis.

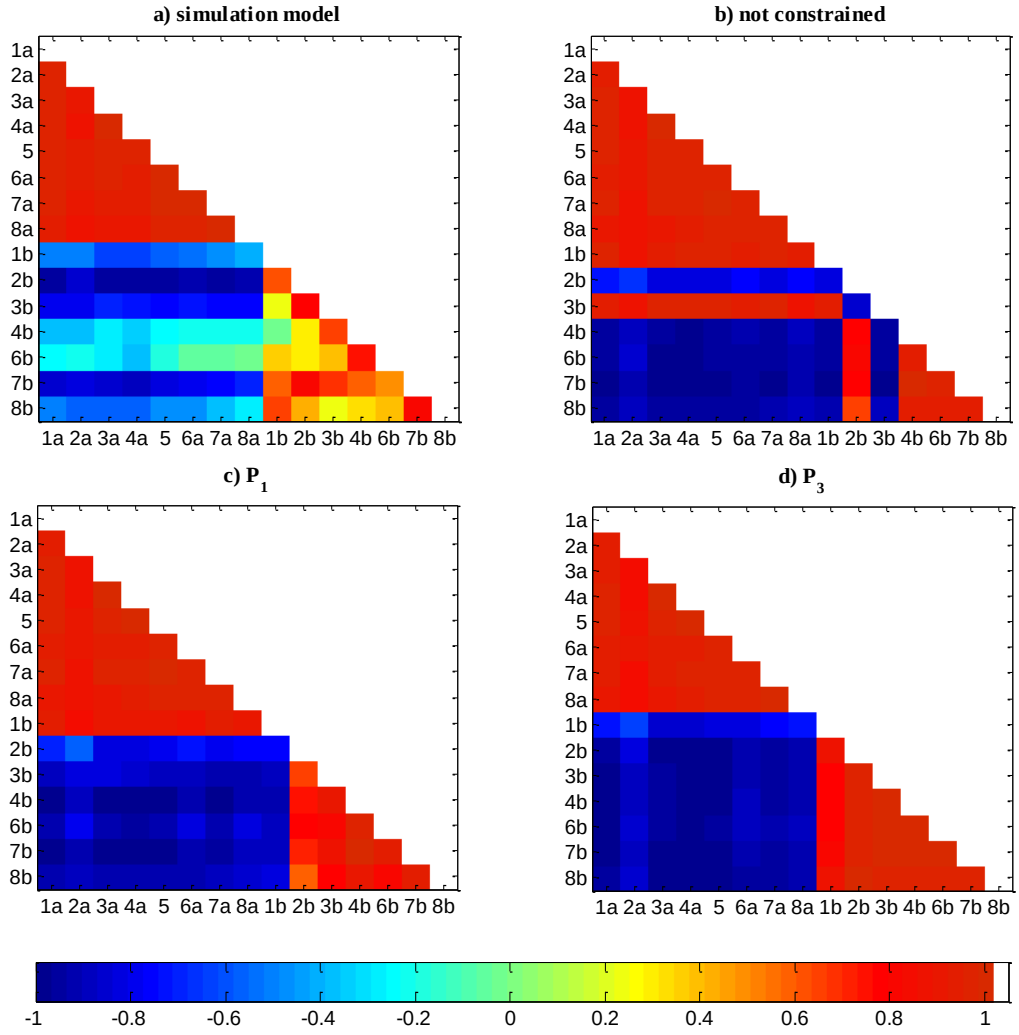

Figure 2.5: The correlation coefficients of monthly mass balance between the different regions. Each plot is derived from the simulated (a) or the approximated (b, c, d) monthly mass balances.

As the baseline, we show the correlation coefficient matrix $\mathbf{R}_{sim}$ from the simulation model in figure 2.5(a). One can notice from this plot that there are three different "blocks" in the matrix **R**: 1) The triangular block on the top left; 2) The square block on the bottom left; 3) Another triangle block on the bottom right. They contain the correlations between margin regions (block 1), the

correlations between margin and interior regions (block 2) and the correlations between interior regions only (block 3). In the simulation model, we find that in block 1 all correlations are positive and have high values (≥ 0.6). The regions above 2000 m are also positively correlated but some regions have relatively low correlation with some other interior regions, for instance $r_{3b,8b}$=+0.2 and $r_{1b,8b}$=+0.8. In block 2, the correlations between regions below and above 2000 m are all negative. Since the run-off is absent from the interior regions, the mass is slowly accumulating in the interior regions in the simulation model, whereas in all the regions below 2000 m the mass is decreasing over time, cf. van den Broeke et al. (2009). In the following, we will show that we can obtain the same (positive/negative) correlation pattern by using separate constraints for the interior and coastal regions.

In figure 2.5(b), (c) and (d) we compare matrix **R** associated with the solutions which are unconstrained, constrained by $\mathbf{P}_1$, $\mathbf{P}_3$, respectively. Pattern errors are noticeable in the first two approximations. For instance, in plot b (unconstrained) we find that the approximated monthly mass balances in region 3b are positively correlated with all the margin regions and negatively correlated with the internal regions, which is opposite to the pattern that we find in plot a). Since we have considered the inter-region correlation as one of the objective functions in the optimization of $\mathbf{P}_1$, the incorrect correlation pattern in region 3b is solved, see figure 2.5(c). However, the problem remains in region 1b. As in plot d), we have restored the correct sign for almost all the regional mass balance by using the constraint $\mathbf{P}_3$.

Nevertheless, one may argue that in spite of the sign of the correlation being correct in plot d), the values of the correlation coefficients are different from the simulation. For instance, we find $|r_{8a,6b}|$=0.02 in the simulation model, which means that the mass balance in region 8a and in region 6b are not correlated. However, in plot d) the absolute correlation coefficient between these two regions becomes $|r_{8a,6b}|$=0.89, thus the approximated correlation is much stronger. The correlation is also enhanced when applying the constraint $\mathbf{P}_1$ as well as in the unconstrained results. Despite the remaining inter-region correlation differences with respect to the simulation, we minimize the correlation difference by using optimal constraints based on only the objective function for the inter-region correlation. From table 2.2 it is clear that we reduce the errors in the inter-region correlation using the optimal $\mathbf{P}_3$ as constraint. It might be possible to further reduce the incorrect correlation by introducing more constraints, which we leave to future work.

Table 2.2: The RMS differences of the inter-region correlation between three approximations with different constraints and the simulation model. Block 1) refers to the correlation between regions below 2000 m. Block 2) refers to the correlation between regions below and above 2000 m and Block 3) refers to the correlation between regions above 2000 m.

	Not constrained	$\mathbf{P}_1$	$\mathbf{P}_3$
Block 1	0.17	0.11	0.11
Block 2	0.71	0.51	0.30
Block 3	0.78	0.63	0.33

2.5. Approximating the regional mass changes from GRACE data

In this section we approximate the monthly mass changes in GRACE observations using the least-squares inversion approach with the optimal constraints $\mathbf{P}_1$ and $\mathbf{P}_3$. We use the release 5 level 2 GRACE monthly potential coefficients from CSR which have a maximum spherical harmonic degree 60. The time interval is January 2003 to December 2012, with a few months excluded because of insufficient observations (July 2003, January 2004, January 2011 and June 2011). We remove a mean over 2003 to 2012 to obtain monthly mass changes. GRACE data is less accurate in C_{20} (Chen et al., 2005 and Chen et al., 2011), hence we replace the C_{20} coefficient with estimates from Satellite Laser Ranging (SLR) (Cheng et al., 2013). Since the orbit center of GRACE satellites is identical to the instantaneous center of mass of the Earth, degree 1 potential coefficients cannot be obtained from GRACE. We use the degree 1 coefficients provided by CSR, which are potential coefficients recovered using GRACE coefficients above degree 2 together with output from an ocean model (Swenson et al., 2008).

The mass changes on GrIS are also influenced by continental hydrology and the GIA effect. We use the monthly GLDAS-Noah model described in Rodell et al. (2004) to remove the continental hydrology leakage, and use the GIA model from Paulson et al. (2007) to correct for GIA. To reduce high-frequency noise and inter-coefficient correlation that manifests as so-called stripes (Swenson and Wahr, 2006). We use a Gaussian filter (Wahr et al., 1998) with a half width of $r_{1/2}$=300 km, the same as used in simulation model. Potential coefficients are converted to monthly EWH changes in the spatial domain and the constrained least-squares inversion approach is applied with the optimal constraints $\mathbf{P}_1$ and $\mathbf{P}_3$, to obtain an approximation of the GrIS monthly mass balances observed by the GRACE satellites.

We first assess the approximation in combined areas as shown in table 2.3. Note that the estimated errors in the annual mass changes consist of the vector sum of 1) the standard deviations of the GRACE data which is also provided by CSR, 2) the estimated uncertainty of 20% in the GIA model (Paulson et al., 2007) which is a guess of the inherent uncertainty in the implemented ice model ICE-5G (Peltier, 2004), and 3) the estimated 30% average uncertainty in GLDAS-NOAH model (Fang et al., 2009). The uncertainty from estimating a linear trend with a 95% confidence interval is considered as well. In table 2.3, for the entire GrIS and for sub-regions, not using constraints or using $\mathbf{P}_1$ and $\mathbf{P}_3$ as constraint all yield consistent mass change trends. It indicates that the anti-correlation errors disappear when regions with negative correlation are combined.

Table 2.3: Approximated annual trend from GRACE data using different constraints on combined areas. The unit is Gt/yr.

	Not constrained	$\mathbf{P}_1$	$\mathbf{P}_3$
< 2000 m	-272.3±17.4	-263.4±17.2	-266.1±17.2
≥2000 m	13.1±9.7	7.5±8.6	8.2±8.6
GrIS	-259.1±19.9	-255.9±19.2	-257.9±19.2
EBIS	-90.9±22.6	-87.2±22.1	-81.4±22.1

In figure 2.6, one can observe that the anti-correlation errors are reduced using the optimal $\mathbf{P}_3$. For instance, in region 1b, when using the constraint $\mathbf{P}_1$ the rate is 10.8±5.5 Gt·yr^{-1} while in the neighbouring region 8b, the rate is -9.7±5.3 Gt·yr^{-1} which is significantly different. The difference is caused by the numerical instability of the inversion which manifests as anti-correlation between adjacent regions, because when comparing the values to the rates found with the RACMO2 model for the same time period, the two regions show similar mass change rates, with 0.4±0.1 Gt·yr^{-1} in region 1b and 0.5±0.1 Gt·yr^{-1} in region 8b. Due to the fact that the run-off and ice-discharge is absent in this area, the RACMO2 model output is more accurate there (Ettema et al., 2009). In order to improve the incorrectly distributed regional mass change between these two regions one can use the constraint $\mathbf{P}_3$ in which case the rate becomes similar to RACMO2 model output, i.e. 1.7±5.5 Gt·yr^{-1} and 0.8±5.3 Gt·yr^{-1} in region 1b and region 8b, respectively.

When using the constrained least-squares approach, the approximated solution is determined by both the GRACE observation and the simulation model. The mass balance of the interior regions is influenced by the external information in the form of $\mathbf{P}_1$ or $\mathbf{P}_3$. Moreover, as in figure 2.6(a), when considering the uncertainties of the rate estimation, we find that the approximations in most of the regions below 2000 m are consistent between the cases unconstrained, or optimal constraints for $\mathbf{P}_1$ and $\mathbf{P}_3$. Hence during the least-squares inversion, the mass balance of these regions is not sensitive to changes in the constraints. Only in region 4a and region 7a, which are the GrIS margin regions located at the south east and west, we find that the rate estimations change by a value larger than the error bars when we alter the constraints. The sensitivity becomes more obvious for regions above 2000 m. For instance, on region 2b, the rate difference between the solution using $\mathbf{P}_1$ and the unconstrained solution is insignificant, (17.1±2.6 Gt·yr^{-1} compared to 17.6±2.6 Gt·yr^{-1}), whereas we obtain a much lower increasing rate with 5.4±2.6 Gt·yr^{-1} using $\mathbf{P}_3$. However, for region 7b, using $\mathbf{P}_1$ and $\mathbf{P}_3$ results in similar estimates of -0.3±4.3 Gt·yr^{-1} and 0.6±4.4 Gt·yr^{-1} mass change, respectively, both of which are much lower than the rate of 32.7±4.4 Gt·yr^{-1} from the unconstrained solution.

The constrained mass change rates derived from the GRACE data is similar to the IOM solution for the whole GrIS, i.e. -258±19 Gt·yr^{-1} and -249.7±34 Gt·yr^{-1} respectively. However, differences can be noticed in the southeast and northwest coastal regions. We compare the regional mass changes trend in the IOM (see table 2.1) with the ones in the approximations from GRACE data (see figure 2.6). Note that in table 2.1, the uncertainties for the IOM mass changes only refers to the uncertainties of the linear interpolation, the uncertainties in the RACMO2 model and the discharges estimations are considerably larger (~20%), cf. (Ettema et al., 2009; Rignot et al., 2008; Sasgen et al., 2012). In the southeast coastal region 4a, the IOM presents more mass loss trend than in the approximations from GRACE data, i.e. -62 Gt·yr^{-1} and -52 Gt·yr^{-1}, while the difference can be explained by the large uncertainties (~30%) of the surface mass balance model in this region, cf. (Sasgen et al., 2012; Vernon et al., 2013; Andersen et al., 2015). In the northwest region 8a, when applying $\mathbf{P}_3$ the mass change rate is -44.1 Gt·yr^{-1} from the GRACE data but only -26.0 Gt·yr^{-1} mass loss rate is given by the simulation, as it has been discussed by Sasgen et al. (2012), this difference can be caused by the high uncertainties of the discharge estimation in this region and the

uncertainties in the simulation model for this region can be approximately 50%. These regional differences to the IOM model are also seen in the GRACE inferred EWH map, as in figure 2.2. If we compare the GRACE data (without approximating the regional mass changes) to the IOM based simulation model, it also shows more mass loss in the northwest and less in the southeast. It indicates that although the optimized constraint is based on the simulation model, the approximations are still mainly determined by the observations, e.g. GRACE data.

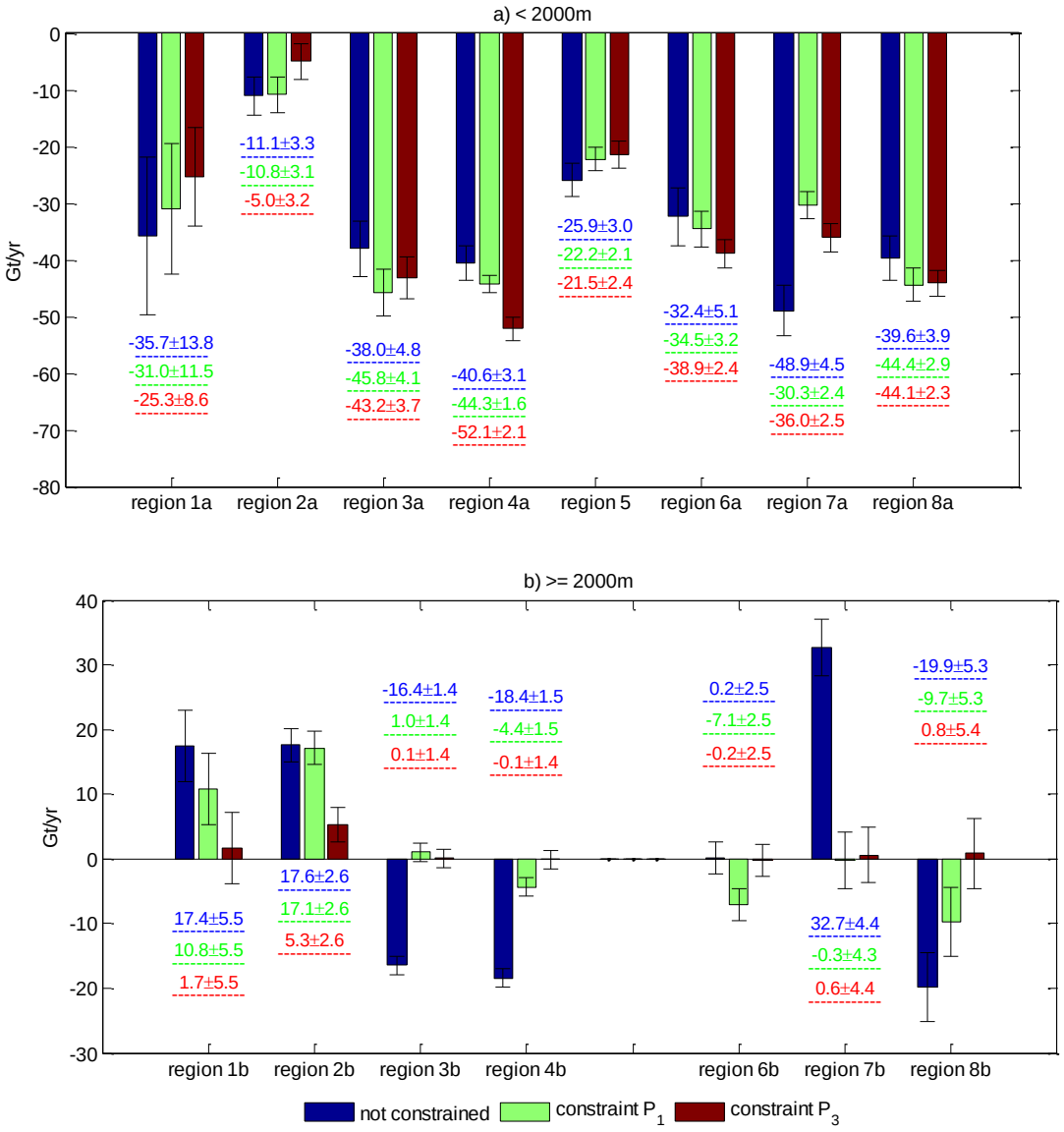

Figure 2.6: The annual mass change rates of the approximated GrIS regional solution for three different cases: unconstrained (blue), optimal $\mathbf{P_1}$ (green) and optimal $\mathbf{P_3}$ (red). The error bars include errors in the GRACE data, GIA model, GLDAS model as well as the errors caused by the linear interpolation.

2.6. Discussion

Least-squares inversion of mass change rates on Greenland from GRACE data requires the use of constraints on the variance. It was shown by BC[13] that the value of the constraint should be optimized, otherwise incorrect regional mass balance estimates can result. We build on their results and find that the use of a single constraint can result in incorrect estimated mass changes for individual regions. The main problem is that in regions of small mass change, the inversion will place negative mass changes next to positive mass change. In our study we propose to use different constraints for regions below and above 2000 m. We are motivated to do this because the mass changes from the surface mass balance models clearly show smaller variance in regions above 2000 m than in the regions below 2000 m.

In order to determine the optimal $\mathbf{P}_3$ a model based simulation is employed, following BC[13]. We extended the optimization approach by adding as another objective function a measure of inter-region correlation of the regional mass balance from the output of the IOM model. By doing so the mass balance approximations in large areas yield a good agreement with similar regional GrIS studies, e.g. Luthcke et al., (2013)), the approximated mass changes from December 2003 to December 2010 were -223.7±19.8 $Gt \cdot yr^{-1}$ (for the margin regions) and -6.6±8.6 $Gt \cdot yr^{-1}$ (for the interior regions). When applying the same time span, we find that the corresponding mass change trends constrained by $\mathbf{P}_3$ are -232.2±11.7 $Gt \cdot yr^{-1}$ and 8.2±7.7 $Gt \cdot yr^{-1}$. Meanwhile we have successfully reduced anti-correlation errors caused by the over-sensitivity of some regions, particularly in the GrIS interior. Thus, the use of separate constraints for higher parts of an ice sheet improves the regional mass balance estimates from GRACE. This suggests that our approach could also improve mass balance estimates for Antarctica where there are also regions of high and low mass variability.

When optimizing the constraints, we used an IOM model which comes with approximately 18% uncertainty. We modify the output of the IOM model by removing (minimum scenario) or adding (maximum scenario) 18% of the original EWH to investigate the influence of the IOM uncertainty during the optimization. When repeating the optimization procedure, we find that the optimal prior variances for the GrIS margin are 9.2 m^2 or 17.3 m^2, for the minimum and maximum scenario, respectively. However, the changes of the constraints for the interior regions are less than 0.02 m^2 compared to using the un-changed scenario in which the IOM model remains the same. The conclusion is that the optimization is more robust in the interior than in the margin, when considering the RACMO2 output and the discharge estimation as reference. The mass balance estimates only differ by 0.9 $Gt \cdot yr^{-1}$ in the GrIS margin, and 0.3 $Gt \cdot yr^{-1}$ in the interior regions from the original IOM. The differences are small when considering the uncertainties in the approximations, see the error bars in figure 2.6.

There are a few issues in the approach that can be further developed in future work:

1) Even though we use three prior variances in the least-squares inversion, there are still differences between GRACE and the combination of modelled surface mass balance in RACMO2 and the estimated ice discharge in the west of Greenland, as can be seen in figure 2.2. In addition to distinguishing the regional mass changes between regions below and above 2000 m, different

constraints can be used for the southern regions in the GrIS (region 4a~region 6a). However, this will add an extra unknown, and the method will rely more on prior knowledge. In addition, the method becomes computationally more demanding than for example the iterative forward modelling approach of W[08].

2) Another way to improve the regional mass changes approximation might be to introduce weights in the least-squares estimation. In Eq. (2.5), we assume that each region in the system has equal weight. Thus a small area has the same weight as a larger area even though there are fewer observations that are sensitive to the smaller area. If we are able to properly weight all the regions in the system, then the over-sensitivity of smaller regions can become less significant.

Acknowledgements We are grateful to the Institute for Marine and Atmospheric research (IMAU), at Utrecht university for providing the RACMO2 model output for this study. Furthermore, the authors acknowledge thoughtful comments by Oliver Baur and an anonymous reviewer of this manuscript.

Chapter 3

Improved GRACE regional mass balance estimates of the Greenland ice sheet cross-validated with the Input-output method

Z. Xu, E. Schrama, W. van der Wal, M. van den Broeke, E. Enderlin

The Cryosphere, Vol. 10, No. 2. (26 April 2016), pp. 895–912, https://doi.org/10.5194/tc-10-895-2016

Abstract

In this study, we use satellite gravimetry data from the Gravity Recovery and Climate Experiment (GRACE) to estimate regional mass change of the Greenland ice sheet (GrIS) and neighboring glaciated regions using a least-squares inversion approach. We also consider results from the input–output method (IOM). The IOM quantifies the difference between the mass input and output of the GrIS by studying the surface mass balance (SMB) and the ice discharge (D). We use the Regional Atmospheric Climate Model version 2.3 (RACMO2.3) to model the SMB and derive the ice discharge from 12 years of high-precision ice velocity and thickness surveys.

We use a simulation model to quantify and correct for GRACE approximation errors in mass change between different sub-regions of the GrIS, and investigate the reliability of pre-1990s ice discharge estimates, which are based on the modeled runoff. We find that the difference between the IOM and our improved GRACE mass change estimates is reduced in terms of the long-term mass change when using a reference discharge derived from runoff estimates in several subareas. In most regions our GRACE and IOM solutions are consistent with other studies, but differences remain in the northwestern GrIS. We validate the GRACE mass balance in that region by considering several different GIA models and mass change estimates derived from data obtained by the Ice, Cloud and land Elevation Satellite (ICESat). We conclude that the approximated mass balance between GRACE and IOM is consistent in most GrIS regions. The difference in the northwest is likely due to underestimated uncertainties in the IOM solutions.

Key words: GRACE, RACMO2, cross-validation, regional mass balance.

3.1. Introduction

During the last decade, the ice mass loss from the Greenland ice sheet (GrIS) has become one of the most significant mass change events on Earth. Because of its ongoing and potentially large future contribution to sea level rise, it is critical to understand the mass balance of the GrIS in detail. As a result of increasing runoff and solid ice discharge (D), the GrIS has been experiencing a considerable and increasing mass loss since the mid-1990s (Hanna et al., 2005; Rignot and Kanagaratnam, 2006; van den Broeke et al., 2009). The changes in mass loss rates are due to different processes. For instance, mass loss acceleration in the northwestern GrIS is linked to the rapidly increasing discharge in this region (Enderlin et al., 2014; Andersen et al., 2015), while in the southeast the increase in mass loss rate after 2003 is mainly due to enhanced melting and less snowfall (Noël et al., 2015).

To quantify the recent changes in the GrIS mass balance, three methods are used: satellite altimetry, satellite gravimetry and the input–output method (IOM) (Andersen et al., 2015; Colgan et al., 2015b; Sasgen et al., 2012; Shepherd et al., 2012; Velicogna et al., 2014; Wouters et al., 2013). We will concentrate on the latter two methods in this study, using results from satellite altimetry for validation purposes.

The IOM is used to evaluate the difference between mass input and output for a certain region. It considers two major mass change entities: surface mass balance (SMB) and solid ice discharge. SMB is commonly estimated using climate models (Ettema et al., 2009; Fettweis, 2007; Tedesco et al., 2013; van Angelen et al., 2012), whereas D can be estimated from combined measurements of ice velocities and ice thicknesses, e.g., Rignot and Kanagaratnam (2006), Enderlin et al. (2014) and Andersen et al. (2015). To reduce the uncertainties in the mass change of SMB and D, the SMB and D from 1961 to 1990 are sometimes used as a reference when applying the IOM method (van den Broeke et al., 2009; Sasgen et al., 2012). However, introducing SMB and D as reference may introduce new uncertainties in the IOM. We will discuss the details of the IOM, as well as the uncertainties of the reference SMB and D, in section. 3.2.

The satellite gravity observations from GRACE (Gravity Recovery and Climate Experiment) provide snapshots of the global gravity field at monthly time intervals, which can be converted to mass variations. Mass variation solutions of a given area that are obtained from GRACE observations are, however, influenced by measurement noise and leakage of signals caused by mass change in neighboring areas. Furthermore, the GRACE monthly gravity fields contain north– south oriented stripes as a result of measurement noise and mis-modeled high-frequency signal aliasing. Therefore, to estimate the mass balance for GrIS sub-regions from GRACE data, we apply the least-squares inversion method (Schrama and Wouters, 2011) in this study with an improved approach (Xu et al., 2015). However, as shown by Bonin and Chambers (2013) in a simulation study, the least-squares inversion method introduces additional approximation errors.

Previous studies have compared regional GrIS mass change from different independent methods. In Sasgen et al. (2012), the mass balance in seven major GrIS drainage areas was derived from the IOM and GRACE data using a forward modeling approach developed by Sasgen et al. (2010). When separating out the IOM components and comparing them with the seasonal variability in the

derived GRACE solution, the relative contributions of SMB and D to the annual mass balances were revealed. In the northwestern GrIS, important differences between IOM and GRACE were noted, which were attributed to the uncertainty in the regional discharge component in this area, where detailed surveys of ice thickness are lacking. The comparison between two approaches shows a mass loss difference of 24±13 Gt yr^{-1} in this region, and as a result the uncertainty in the regional mass balance estimate is estimated at ~46 %. However, using new discharge estimates and the corresponding IOM regional mass change in the northwestern GrIS, Andersen et al. (2015) found that the difference between GRACE and IOM mass loss estimates fell within the combined uncertainty range. However, using the least-squares based inversion approach of Schrama and Wouters (2011), we find that the mass change differences between results obtained from GRACE and the IOM in the southern GrIS increase and cannot be explained by the assumed uncertainties. An example of the regional differences between the GRACE data and the IOM solution can be seen in figure A3.1. The details of this difference will be discussed in section 3.4.

In this study, we aim to investigate the two aforementioned sources of uncertainties in GRACE and IOM mass balance estimations: (i) we present a way to reduce the error from the inversion approach and (ii) we investigate different discharge estimates. We then evaluate our results by comparing the GRACE and IOM estimates both with each other and with published estimates from satellite altimetry.

The GrIS drainage system (DS) definition of Zwally (2012) is employed here to investigate the mass balance in GrIS subregions. This definition divides the whole GrIS into eight major drainage areas, and each drainage area is further separated by the 2000 m elevation contour line, creating interior and coastal regions for each drainage area. This GrIS DS definition is employed by several other studies (Andersen et al., 2015; Barletta et al., 2013; Colgan et al., 2015a; Luthcke et al., 2013; Sasgen et al., 2012). The regional GrIS mass change estimated with GRACE are influenced by mass change from areas outside the ice sheet, i.e., from Ellesmere Island, Baffin Island, Iceland and Svalbard (EBIS) (Wouters et al., 2008). Therefore, we include four additional DSs to reduce the leakage from these regions. The overall mascon definition used in this study is shown in figure. 3.1.

The main topic of this study is to provide improved GrIS regional mass balance estimates from GRACE and the IOM. We show that the improved GRACE solution reduces the regional differences between two mass change estimates, especially in the southeastern GrIS region. Furthermore, we compare the GRACE solution with the IOM, which employs different reference discharge estimates, showing that the uncertainties in the reference discharge can result in an under estimated mass loss rate in the IOM regional solution, in particular in the northwestern GrIS region.

In section 3.2, we present SMB mass change from a recently improved regional atmospheric climate model (RACMO2.3) (Noël et al., 2015) and discharge estimates of Enderlin et al. (2014), which are based on a near-complete survey of the ice thickness and velocity of Greenland marine-terminating glaciers. In section 3.3, we introduce the least-squares inversion approach. In section 3.4, we start by investigating different methods to calculate mass change in GrIS drainage areas using the modeled SMB and D estimates. Subsequently, we identify the approximation errors

in regional mass change estimates from GRACE data, followed by a comparison of mass change estimates from GRACE and the IOM and a discussion of the remaining differences. The conclusions and recommendations are given in section 3.5.

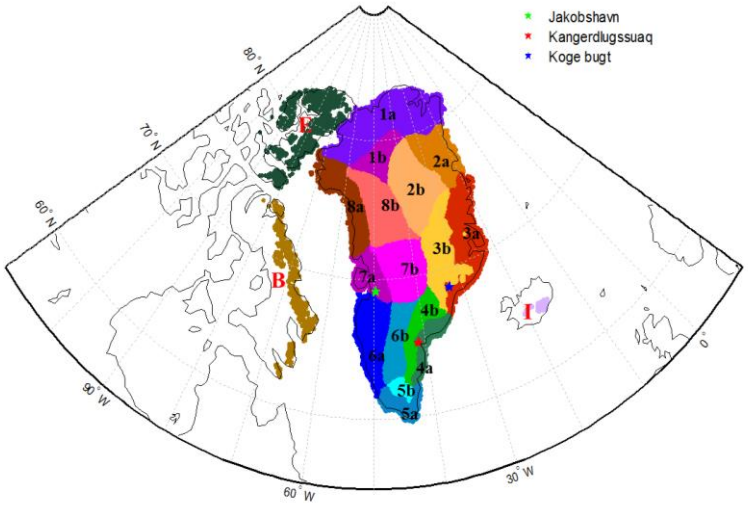

Figure 3.1. The GrIS mascon layout, based on the basin definition by Zwally (2012). The mascons with the same digits refer to a region belonging to the same drainage system. The characters "a" and "b" indicate the GrIS margin (<2000 m) and GrIS interior (≥2000 m), respectively. There are 16 GrIS mascons and 4 neighbouring Arctic mascons. The location of the three largest discharge outlets are marked with a star, i.e. Jakobshavn (green), Kangerdlugssuaq (red) and Koge Bugt (blue) glaciers. The glacier area is defined in the RACMO2 model. In this study, we will use the index of the drainage systems to label each mascon, e.g.: mascon DS7 is drainage system No.7

3.2. IOM method

3.2.1. SMB and D

For the GrIS, precipitation (P) in the form of snowfall is the main contribution to the mass input, while mass loss is a combination of sublimation (S), melt water runoff (R), and solid ice discharge (D). Surface mass balance (SMB) equals to P-S-R, and subtracting D from SMB yields the total mass balance (TMB). In this study, we use the Regional Atmospheric Climate Model, version 3 (RACMO2.3) to model the SMB of the GrIS. RACMO2 (Ettema et al., 2009; Van Angelen et al., 2012; van den Broeke et al., 2009) is developed and maintained at the Royal Netherlands Meteorological Institute (KNMI) and has been adapted for the polar regions at the Institute for Marine and Atmospheric Research, Utrecht University (UU/IMAU). RACMO2 model output is currently available at ~ 0.1° spatial resolution for Jan 1958 to Dec 2014. The differences between a previous model version (RACMO2.1) and other SMB models are discussed by Vernon et al. (2013). In RACMO2 we assume 20% uncertainties for the P and R components in each grid cell. Assuming both components to be independent, the uncertainty of the SMB is the quadratic sum of

uncertainties of P and R. The magnitude of S is small and its absolute uncertainty negligible compared to those in P and R. The RACMO2 model also provides the estimates of SMB in the peripheral glacier areas, which we have included in this study.

Ice discharge (D) estimates from Enderlin et al. (2014) (hereafter Enderlin[14], with the associated discharge estimates D-14) are used in this study. In Enderlin[14], the ice thickness of 178 glaciers is estimated as the difference in ice surface elevations from repeat digital elevation models and bed elevations from NASA's Operation IceBridge airborne ice-penetrating radar data. The ice surface velocity is obtained from tracking the movement of surface features visible in repeat Landsat 7 Enhanced Thematic Mapper Plus and Advanced Spaceborne Thermal and Reflectance Radiometer (ASTER) images. For glaciers with thickness transects perpendicular to ice flow (i.e., flux gates), the ice flux is estimated by summing the product of the ice thickness and surface speed across the glacier width. Ice flux for glaciers with no thickness estimates is retrieved using the empirical scaling factors as derived in Enderlin et al. (2014). Because the ice fluxes are calculated within 5 km of the estimated grounding line locations, SMB gain/loss between the observations and the grounding lines will be small and the ice discharge is estimated directly from the fluxes (Enderlin et al., 2014). The estimation of discharge uncertainty of 1~5% D for each glacier is smaller than in previous studies, e.g. Rignot et al. (2008) (hereafter Rignot[08], and the associated estimates are denoted by D-08), which relied on interior ice thickness estimates that were assumed constant in time.

3.2.2. Cumulative TMB anomaly

For the whole GrIS or a complete basin from ice sheet maximum height to the coast, the total mass balance is:

$$\mathrm{TMB} = \mathrm{SMB} - \mathrm{D} \tag{3.1}$$

In this study, we further separate each GrIS basin in a downstream (I) and upstream (II) region separated by the 2000 m surface elevation contour line. Thus, for the sub-divided regions Eq. (3.1) becomes:

$$\mathrm{TMB} = \mathrm{TMB}^{\mathrm{I}} + \mathrm{TMB}^{\mathrm{II}} \tag{3.2}$$

where

$$\mathrm{TMB}^{\mathrm{II}} = \mathrm{SMB}^{\mathrm{II}} - \mathrm{F}^{\mathrm{II}} \tag{3.3}$$

and

$$\mathrm{TMB}^{\mathrm{I}} = \mathrm{SMB}^{\mathrm{I}} + \mathrm{F}^{\mathrm{II}} - \mathrm{F}^{\mathrm{I}} \tag{3.4}$$

in which F^{II} refers to the ice flux across the 2000 m elevation contour, and F^{I} refers to the ice flow across the flux gate. Note that F^{II} is cancelled if the study area includes both the regions below and above the 2000 m contour, but F^{II} has to be considered when the upstream and downstream regions are considered separately. As described above, we assume that SMB changes downstream of the Enderlin[14] flux gates are negligible and that $\mathrm{F}^{\mathrm{I}} = \mathrm{D}$.

In order to fit the temporal resolution of the modeled SMB data, we interpolate the yearly D on

a monthly basis. Significant seasonal variations in ice velocity have been observed along Greenland's marine-terminating outlet glaciers (Moon et al., 2014). However, since we focus mostly on long-term changes in mass in this study, monthly variations in D should have a negligible influence on our analysis and we assume that D is approximately constant throughout the year. Contrary to the GRACE data which measures a thin layer of mass near to the Earth's surface (Wahr et al., 1998), the SMB, D and TMB are estimates of rates of mass change (i.e., mass flux) in Gt per month. Hence in order to compare with GRACE, one has to integrate the SMB and D from a certain month (or year), which yields:

$$\Delta\mathrm{TMB}_i = \int_{i_0}^{i} (\mathrm{SMB}_t - \mathrm{D}_t) dt \quad \textbf{(3.5)}$$

where $\Delta\mathrm{TMB}_i$ is the cumulative mass change at month i in IOM (unit is Gt) and the integration time period is from a certain initial month i_0 to month i.

In previous study of mass balance IOM, when estimates of D are not available for some regions (Rignot et al., 2008), the 1961 to 1990 reference SMB is used to approximate the missing regional D (Sasgen et al., 2012). Also, due to the uncertainties in the SMB model, accumulating the TMB over a long time period may also lead to unrealistic mass gains or losses (van den Broeke et al., 2009). By removing the reference, the influence of the large uncertainties and inter-annual variability in SMB and D can be reduced (van den Broeke et al., 2009). For instance the uncertainties due to model configurations could be the similar in every monthly SMB estimate, and cumulating over long period may result to a large uncertainty. The reference period is chosen based on the assumption that the mass gain from the surface mass balance during that period is compensated by ice discharge, so the GrIS was in balance (i.e. no mass change).

For the reference period we defined the month index to run from i_0 to i_1, from i_2 to i_n afterwards. Since we assume the GrIS was in balance during this period, $\int_{i_0}^{i_1} (\mathrm{SMB}_t - \mathrm{D}_t) dt = 0$. By removing the reference SMB and D (i.e. SMB_0 and D_0) Eq. (3.5) becomes:

$$\Delta\mathrm{TMB}_i = \int_{i_2}^{i} (\delta\mathrm{SMB}_t - \delta\mathrm{D}_t) dt \quad \textbf{(3.6)}$$

where $i \geq i_2$, $\delta\mathrm{SMB}_i = \mathrm{SMB}_i - \mathrm{SMB}_0$ and $\delta\mathrm{D}_i = \mathrm{D}_i - \mathrm{D}_0$. Note that SMB_0 and $\delta\mathrm{SMB}_i$ are both rates of mass change, similar to the discharge.

As explained before, when Eq. (3.6) is used to compute the mass balance for the regions below and above 2000 m separately, the ice flux across the 2000 m contour (F^{II}) has to be considered. Therefore we introduce two assumptions, i.e.: 1) F^{II} is constant over time, which means $\mathrm{F}^{\mathrm{II}} = \mathrm{F}_0^{\mathrm{II}}$ ($\mathrm{F}_0^{\mathrm{II}}$ is the F^{II} during the reference period), so $\int_{i_2}^{i} \delta\mathrm{F}_t^{\mathrm{II}} dt = 0$; 2) The separate GrIS interior and coastal regions are all in balance during the 1961 – 1990 reference period, i.e. $\int_{i_0}^{i_1} (\mathrm{SMB}_0^{\mathrm{II}} - \mathrm{F}_0^{\mathrm{II}}) dt = 0$ and $\int_{i_0}^{i_1} (\mathrm{SMB}_0^{\mathrm{I}} + \mathrm{F}_0^{\mathrm{II}} - \mathrm{D}_0) dt = 0$ Assumption 1) is necessary since there is a lack of yearly measurements of ice velocity across the 2000 m contour. An estimate of decadal change by Howat et al. (2011) suggests it is reasonable to assume a constant F^{II} for the entire GrIS, except for a few glaciers, such as the Jakobshavn glacier in basin 7 where the F^{II} may be higher than $\mathrm{F}_0^{\mathrm{II}}$ after

2000. In Andersen et al. (2015), the mass balance of the interior GrIS (in their study defined as the ice sheet above the 1700 m elevation contour) was 41±61 Gt·yr^{-1} during the 1961–1990 reference period and in Colgan et al. (2015) the ice flux across the 1700 m contour was estimated to be 54±46 Gt·yr^{-1} for the same time period, indicating the assumption of balance approximately holds within the uncertainties.

Based on these two assumptions, we apply Eq. (3.6) for the interior and coastal GrIS regions, yielding:

$$\Delta \mathrm{TMB}_i^{\mathrm{II}} = \int_{i_2}^{i} \delta \mathrm{SMB}_t^{\mathrm{II}} dt \tag{3.7}$$

and

$$\Delta \mathrm{TMB}_i^{\mathrm{I}} = \int_{i_2}^{i} (\delta \mathrm{SMB}_t^{\mathrm{I}} - \delta \mathrm{D}_t) dt \tag{3.8}$$

We quantify the combined uncertainties of assumptions 1) and 2) by comparing the results from Eq. (3.8) to the regional mass balance derived from GRACE by Wouters and Schrama (2008) and derived from ICESat by Zwally et al. (2011), resulting in ~±15 Gt·yr^{-1} uncertainties for the entire interior GrIS. The regional uncertainties are summarized in table A3.3. Note that for each region, the same uncertainty is applied to both the interior and coastal areas. For the whole basin the uncertainties associated with assumption 1) and 2) will vanish, because these two assumptions are needed only when we separate the coastal and interior regions.

3.3. GRACE

3.3.1. Post-processing GRACE data

In this study we use the GRACE release 5 level 2 monthly spherical harmonics coefficients C_{lm} and S_{lm} ('*GSM*') produced by the University of Texas Center for Space Research (CSR). The time interval is from Jan 2003 to Jan 2014 and the maximum spherical harmonic degree l=60. We add C_{10}, C_{11} and S_{11} coefficients (related to the motion of the Earth's geocenter) obtained from GRACE data and independent oceanic and atmospheric models (Swenson et al., 2008). The geopotential flattening coefficients (C_{20}) in GRACE data are less accurate than those from the Satellite Laser Ranging (SLR) measurements (Chen et al., 2004). We replace these coefficients with the ones from Cheng et al. (2013). The GRACE potential coefficients are averaged between Jan 2003 and Jan 2014 and this average field serves as a reference to obtain monthly anomalies ΔC_{lm} and ΔS_{lm}.

GRACE observations of mass change within a sub-region of the GrIS are affected by mass changes in neighboring areas, a phenomenon known as leakage (Wahr et al., 1998). But GRACE data should also be corrected for known oceanic and atmospheric mass motions, continental hydrology and Glacial Isostatic Adjustment (GIA). The oceanic and atmospheric mass changes are already removed from the coefficients provided by CSR. The Global Land Data Assimilation System (GLDAS) model (Rodell et al., 2004) is employed to simulate the continental hydrology,

which is then removed from the GRACE monthly coefficients. Note that permafrost regions are excluded in the GLDAS version 2 1.0 degree monthly data that are obtained from the Goddard Earth Sciences Data and Information Services Center.

The GIA effect in the GRACE data for the GrIS is compensated via the model output of Paulson et al., (2007), which is based on the ICE-5G ice loading history and the VM2 Earth model (Peltier 2004). Hereafter we refer to this model by Paulson-07. In addition to this model, 11 alternative GIA models are employed based on different ice history and viscosity models to determine the uncertainty in the GIA correction. For instance, the models of van der Wal et al., (2013) include 3D changes in viscosity and the model of Simpson et al. (2009) uses a different ice loading history, see the summary of the GIA models used in this study in table A3.3. An isotropic Gaussian filter is employed to reduce the noise in GRACE data (Wahr et al. 1998), with a half width of $r_{1/2}$=300 km.

3.3.2. Inversion of the regional mass balance

To estimate the regional mass balance in separate GrIS basins, we apply a constrained least-squares inversion approach (Bonin and Chambers, 2013; Schrama and Wouters, 2011).

$$\hat{\mathbf{x}} = (\mathbf{H^T H} + \mathbf{P^{-1}})^{-1}\,\mathbf{H^T y} \tag{3.9}$$

The vector $\mathbf{y}$ contains the monthly GRACE data. To compute the influence functions in the design matrix $\mathbf{H}$ we assume a layer of water with unit height uniformly distributed over the mascon, then express the mass change in spherical harmonic coefficients up to d/o 60, similar to the GRACE data. The vector $\hat{\mathbf{x}}$ represents the scale factors for the unit mass changes in each basin that we aim to find. $\mathbf{P}$ is the covariance matrix of the mass changes in each mascon. When assuming that the mass changes in each equally weighted mascon are independent then $\mathbf{P} = \lambda\mathbf{I}$, with λ the prior variance of the regional mass changes. In our previous study, we demonstrated that three different prior variances for the GrIS regions below and above 2000 m, as well as for the surrounding Arctic regions respectively improved the recovery of regional mass changes (Xu et al. 2015). Using a simulation model based on the IOM (see section A3.3) optimal regional constraints were determined, i.e. for coastal mascons $\boldsymbol{\lambda_a}$=13 m^2, for inland mascons $\boldsymbol{\lambda_b}$=0.1 m^2 and for the nearby surrounding EBIS regions (Ellesmere Island, Baffin Island, Iceland and Svalbard) regions $\boldsymbol{\lambda}_{\mathrm{EBIS}}$=11 m^2. One may notice that the constraints $\boldsymbol{\lambda_a}$ and $\boldsymbol{\lambda}_{\mathrm{EBIS}}$ are slightly different from the ones we found in chapter 2. This is because we use a newer version of RACMO2 in this chapter. The influence on the approximation is found to be negligible.

3.4. Cross-validation

3.4.1. Reference SMB and D

In this study, the error in SMB_0, hereafter σSMB_0 involves the systematic error caused by the assumption of a reference period and the fact that averaging within the chosen reference period results in an error. Both parts will be explained hereafter.

The systematic error is the uncertainty in the SMB derived from model output and the averaging

error is related to the variability of the reference SMB_0 during 1961–1990. To quantify the later, we apply a Monte-Carlo simulation to evaluate the standard deviations of the SMB_0 resulting from using different combinations of 20-year average of SMB. The sampled combinations are randomly chosen from the months between 1961 and 1990, following van den Broeke et al. (2009). For RACMO2, we find 20 Gt·yr^{-1} averaging errors in σSMB_0. The SMB_0 from RACMO2 yields 403 Gt·yr^{-1} hence the systematic error is approximately 73 Gt·yr^{-1} (considering 18% uncertainty in RACMO2). If we assume both errors are independent, then σSMB_0=75 Gt·yr^{-1}.

We also investigate the uncertainties of the 1961 – 1990 reference discharge. In this study we employ D-14 as the D estimates in IOM. However, D-14's time series starts from the year of 2000 when the GrIS already was significantly out of balance. In order to retrieve D_0 for D-14 (D_0-14), we employ the D_0=413 Gt·yr^{-1} in 1996 from D-08 (D_0-08) for the entire GrIS, and assume that the regional D changes from 1990 to 2000 in D-08 should be proportional to the changes in D-14 in each region, i.e. D-14 and D-08 are linearly correlated. The details of the interpolation of regional D_0 are given in section A3.1. Note that the averaging error in D_0 is minimized via an iteration process, the details can be found in Rignot et al. (2008). Due to the lack of ice thickness information before 2000, the reference D_0 in Rignot^{08} has high uncertainty, especially in the northwest of the GrIS.

Another way to obtain historic discharge estimates is by using the presumed correlation between discharge and SMB or runoff (Rignot et al., 2008; Sasgen et al., 2012). The approach assumes that the anomaly of the discharge with respect to a reference SMB ($\delta \mathrm{D} = \mathrm{SMB}_0 - \mathrm{D}$) is correlated with the anomaly of the 5-year averaging runoff with respect to a reference runoff ($\delta \mathrm{R} = \mathrm{R} - \mathrm{R}_0$). Note that the lagging correlation is discussed in Bamber et al. (2012) and Box and Colgan (2013). In this study we choose to use the runoff output from the RACMO2 model. We consider three estimates of D, i.e. by Rignot^{08}, Enderlin^{14} and Andersen et al. (2015), based on different measurements of the ice thickness and flux velocity changes, integration areas (areas between the flux gate and the grounding line), SMB and ice storage corrections and whether the peripheral areas are included or not. In this study we provide runoff-based estimates D_0 only for those ice sheet basins where the correlation between δD and δR is strong (figure 3.2). For the entire GrIS, we obtain a high correlation (R^2=~0.86), similar to the correlation found by Rignot et al. (2008), but the regional correlations are lower and vary from 0.19 to 0.94. In DS7 and DS8, the discharge anomaly is obviously correlated with the runoff anomaly ($R^2 > 0.9$), while in other regions (i.e. in DS2, DS4, DS5 and DS6), the correlation is low ($R^2 < 0.5$). In DS3a, when we consider only the D estimates from Enderlin-2014 and Andersen-2015, the correlation increases to R^2=0.72. Note that, the regions with high correlation are also those that have a large fraction of marine-terminating glaciers. We derive the linear relation between δD and δR for 8 major GrIS DS and calculate the regional annual δD from 1960 to 2013 using this linear relation.

Hereafter, the regional cumulative discharge anomaly (δD), which is derived from the RACMO2.3 run-off, is denoted as δD^R, while δD-08 and δD-14 refer to δD based on Rignot^{08} and Enderlin^{14}, respectively. We compare δD^R, δD-08 and δD-14 in figure 3.3 for the time interval 2000 to 2007, which is common to both δD-08 and δD-14. In DS7 we find a correlation of R^2=0.94. In

that region, δD-08 and δD-14 are similar, i.e., 20.1±1.9 and 17.6±2.2 Gt yr^{-1}, respectively, but δD^R is 8.9±4.7 Gt yr^{-1}. The difference between the runoff-derived and flux gate D estimates may indicate that the reference D_0 for this region should be ~9 Gt yr^{-1} lower than D_0 estimated by Rignot^{08}. A similar difference can be seen in DS4 where we obtain 36.2±2.5 Gt yr^{-1} for δD-14 and 37.9±2.8 Gt yr^{-1} for δD-08, but δD^R is 8.4±3.3 Gt yr^{-1}. However, in DS4, δD^R is probably not reliable, since the runoff-to-discharge correlation is weak in this region (R^2=0.38). For the entire GrIS, the reference discharge D_0 is 427±30 Gt yr^{-1} for δD-08 and 414±44 Gt yr^{-1} for δD-14. When applying the runoff-based interpolated D_0 only for DS1, DS3, DS7 and DS8, with the rest of drainage areas using δD-14, D_0 becomes 410±37 Gt yr^{-1} and all three versions of reference discharge agree within their respective uncertainties.

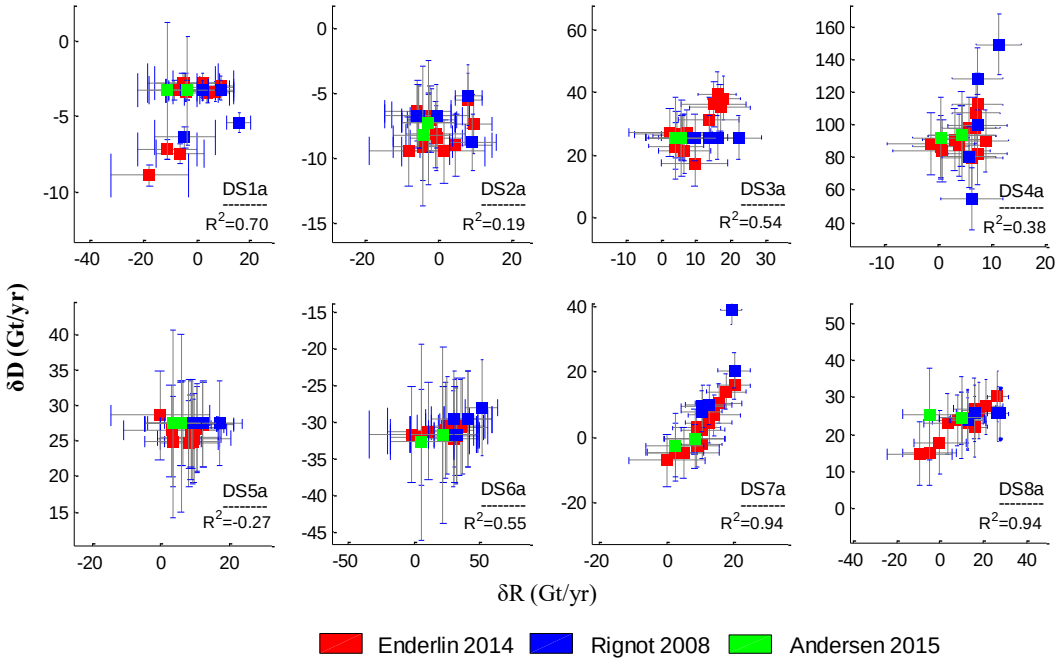

Figure 3.2: Correlation between the anomaly of the discharge ***δD*** with respect to a reference SMB (y-axis) and the 4-year averaging runoff ***δR*** (x-axis) in GrIS regions. The symbols with different colours refer to different estimations of D. The grey bars for both ***δD*** and ***δR*** indicate the errors. The correlation coefficients R2 are also shown in each plot.

To evaluate the SMB_0 and D_0 used in this study, we compare the IOM regional mass balance in eight major drainage areas (interior and coastal regions are combined) and apply both Eq. (3.5) and Eq. (3.6). The latter equation relies on the determination of the SMB_0 and D_0 while Eq. (3.5) does not, so the comparison can provide an indication about the reliability of the SMB_0 and D_0 for some basins. For the application of Eq. (3.6) we use two methods. Method 2 uses δD-14 while method 3 uses δD^R in DS1, DS3, DS7 and DS8. As can be seen in figure 3.3, the three methods agree for the whole GrIS, as well as for most of the drainage areas, within their uncertainties. In DS4, DS7 and

DS8, however, methods 1 and 2 are significantly different, which may be caused by underestimated cumulative errors in Eq. (3.5) or a less accurate reference surface mass balance SMB_0 and reference discharge D_0. This is further discussed in section 3.4.3.

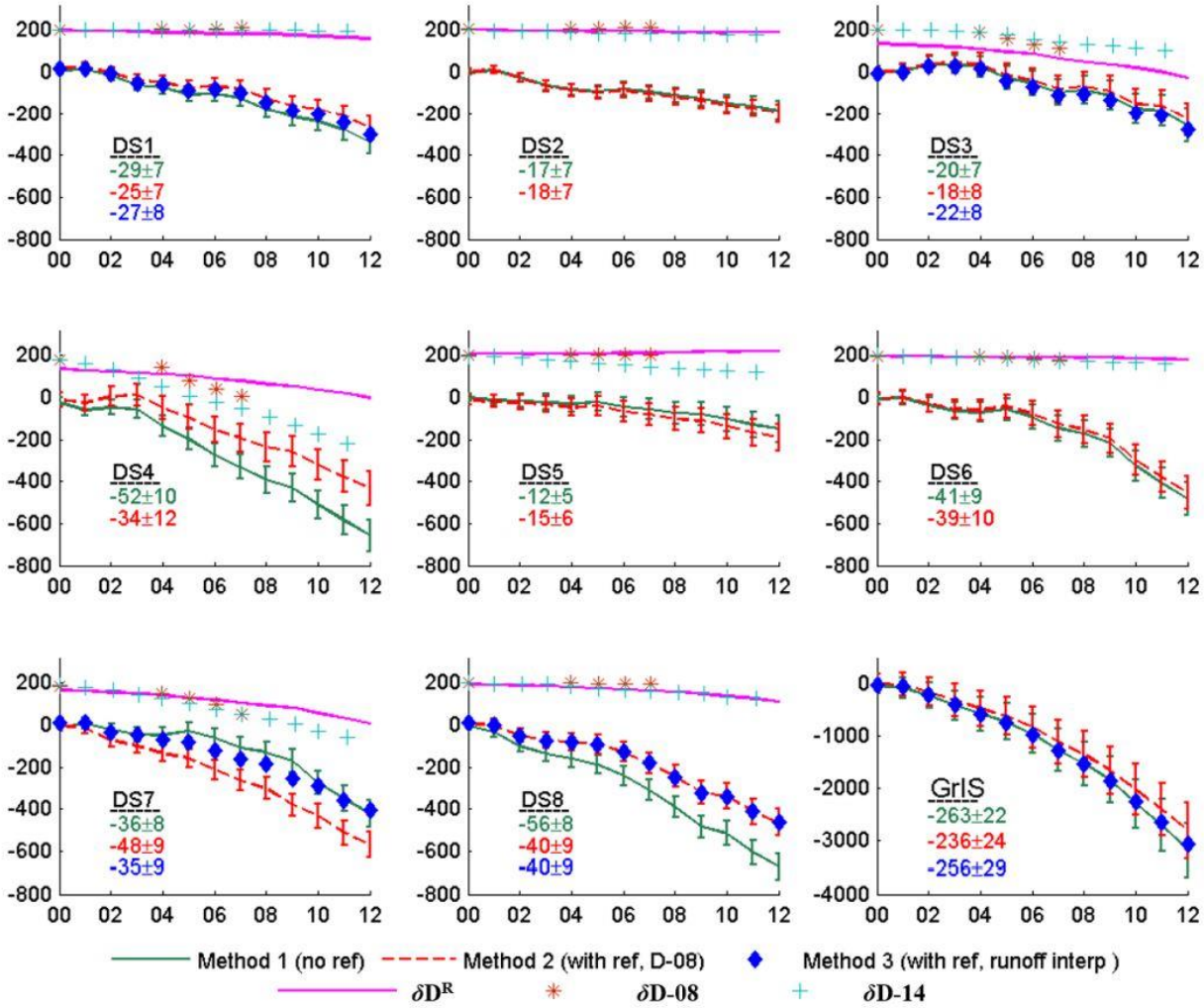

Figure 3.3: Comparison between cumulative TMB (2000–2012) obtained with three different methods. method 1, using no reference TMB, is shown with a green curve. For method 2 (red markers and curve), the reference discharge is based on the estimation from D-08, while the discharge estimation from D-14 is used (δD-14) for the years after 2000. Method 3 (blue markers and curve) interpolates the reference discharge using the modelled runoff data (only in DS1, DS3, DS7 and DS8), is dented by δD^R. δD-08 refers to the discharge estimated using D-08. All the discharges are shifted upward by 200 Gt for visualization purposes. The numbers in each plot indicate the annual TMB change rates in Gt yr^{-1}. The x axis shows the last two digits of the years from 2000 to 2012.

3.4.2. Approximation errors

In the solution of $\hat{\mathbf{x}}$, two types of errors occur: a) systematic errors are caused by measurement errors propagated through the least-squares approach and b) the additional error that is introduced when applying Eq. (3.9). For the type b) error, Bonin and Chamber (2013) show that Eq. (3.9)

leaves a noticeable difference between the approximation $\hat{\mathbf{x}}$ and the "truth" (a GrIS mass changes simulation), in particular in GrIS sub-regions, which we recognize as an error source, also see the discussion in Tiwari et al. (2009). Hereafter the type b) error is denoted as 'approximation error ' or $\boldsymbol{\varepsilon}$. We estimate $\boldsymbol{\varepsilon}$ by using simulations of GrIS as $\mathbf{x}$, following Bonin and Chambers (2013) so that the approximation error becomes $\boldsymbol{\varepsilon} = \mathbf{x} - \hat{\mathbf{x}}$. The simulated regional mass changes on the mascons are $\mathbf{x} = [\mathrm{x}_1, \mathrm{x}_2, \mathrm{x}_3, \ldots, \mathrm{x}_n]$, where n is the total number of mascons. We will show that there is a relation between $\hat{\mathbf{x}}$ and $\mathbf{x}$, which can be used to correct for the approximation errors.

The simulation model $\mathbf{y} = f(\theta, \lambda)$is based on 10 years linear trend (2003 to 2012) of mass changes of SMB and D estimates (see section A3.3), with uncertainties of the simulation model written as $\boldsymbol{\sigma}(\theta, \lambda)$. We employ a Monte-Carlo approach to simulate a sample of 1000 randomly distributed observations, according to $\mathbf{y}_l{}' = \mathbf{y} + \mathbf{k}_l\boldsymbol{\sigma}$ with $\mathbf{k}_l = k_l(\theta, \lambda)$ a vector of random scaling factors varying from -1 to 1, and index l running from 1 to 1000. Hereby it is important to note that we assume that measurement errors do not exist (i.e. the simulation model is assumed to be reality); in addition, we assume that the generated samples in the simulation ($\boldsymbol{\sigma}$) are normally distributed.

Next we apply Eq. (3.9) to yield approximated regional mass changes $\hat{\mathbf{x}} = [\hat{x}_m]$, in which m is the index of the mascons (see figure 3.1). From the simulation we can derive the real regional mass change rate $\mathbf{x} = [x_m]$. As mentioned above, the difference between $\hat{\mathbf{x}}$ and $\mathbf{x}$ equals the approximation error. In figure 3.4 we show that the x_i are linearly correlated with $\hat{x}_i$. By applying this correlation to the approximations derived from GRACE data, one can reduce the approximation errors in the GRACE based regional mass balance approximations.

The simulated trend in regional mass changes $\mathbf{x}'$ and the corresponding approximation $\hat{\mathbf{x}}'$ are shown in figure 3.4. It can be noticed that the approximations are strongly correlated with the simulation in the coastal regions over time and with an average correlation coefficient R^2=0.9. This means that the approximated regional solutions are close to the simulation. The correlation in region DS1a is weaker (~0.6), which suggests that the approximation for region DS1a is influenced more by mass changes in neighbouring regions such as region DS8a. In the simulation the inter-region correlation between DS1a and DS8a is ~ –0.1, while in the approximations, the correlation rises to ~ –0.5. By comparison, another neighbour of DS8a, DS7a, has a very weak inter-region correlation with DS8a both in the simulation and in the approximation (~0.04). The inter-region correlation errors are systematic due to the least-squares inversion (Bonin and Chambers, 2013; Schrama and Wouters, 2011). Previous work shows that the regional approximation errors can be reduced when specifying constraints for the GrIS coastal and inland regions, but within the coastal region all the sub-DSs are constrained by the same prior variance in this study, thus the increase in correlation between DS1a and DS8a remains.

For the coastal regions, there is a linear relationship between the simulations $\mathbf{x}$ and the approximation $\hat{\mathbf{x}}$, as can be seen in figure 3.4. We fit this relationship by $\mathbf{x} = \alpha_1\hat{\mathbf{x}} + \alpha_0$, with a summary of α_1 and α_0 given in table A3.1. The linear relationship between the simulated and the approximated regional mass change rates is found to be stable; even when the simulation uncertainties are multiplied with a factor or 5 (light green marks in figure 3.4), the average

regression parameters ($\alpha_1$and α_0) vary by less than ~1% for the coastal mascons. Therefore, it is reasonable to assume α_1 and α_0 should also reflect the relationship between the reality and the approximation, as derived from GRACE observations. When the vector of observations **y** becomes the GRACE observations, by applying the linear relationship to the corresponding approximation $\hat{\mathbf{x}}$, we can derive an improved GRACE regional solution. We will show that this correction yields better agreement between GRACE and the IOM in section 3.4.3.

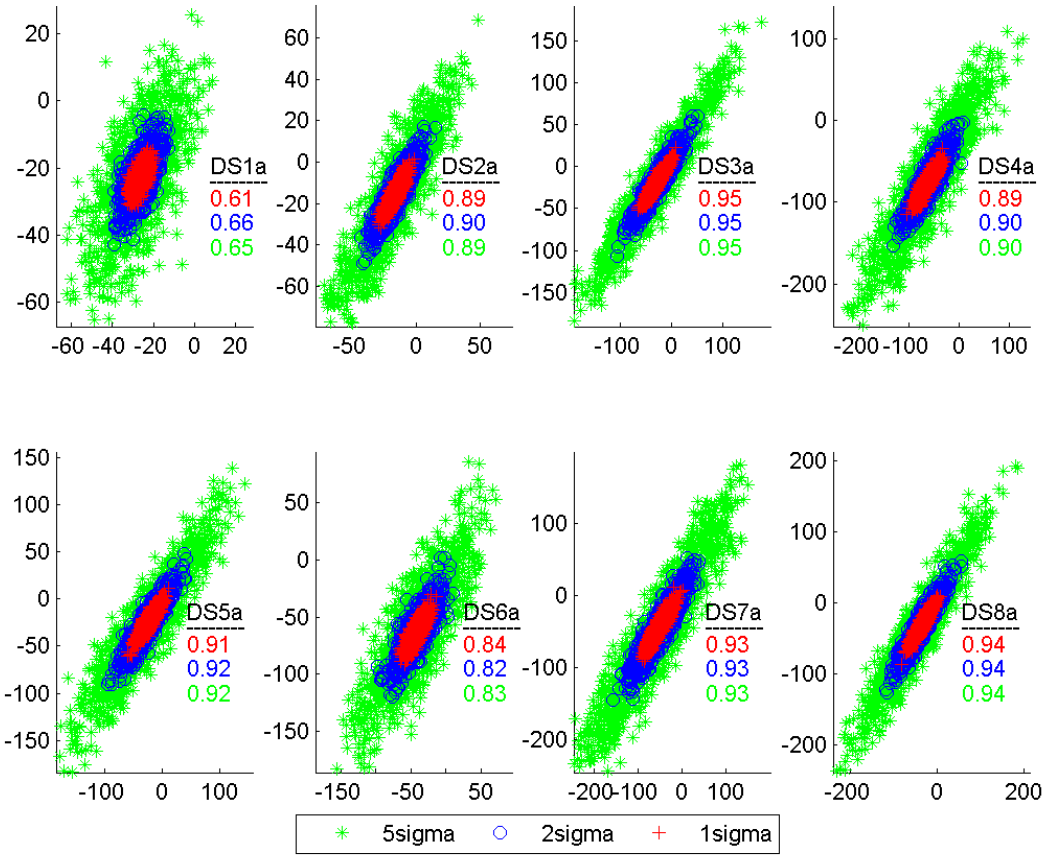

Figure 3.4: Correlation between the linear trend in the simulations x′ (y-axis) and the corresponding approximation $\hat{x}'$ (x-axis). The unit is in Gt•yr^{-1}. The colours are associated with the changing range of x′ for a standard deviation going from 1σ to 5σ. The numbers refer to the R^2 coefficient for three different σ.

Contrary to the coastal regions, the linear relation between **x** and $\hat{\mathbf{x}}$ is weak in the interior regions, where the mean correlation coefficient is ~0.2. This may be because interior regions show smaller mass change rates than the coastal regions, or maybe the processes act on larger scales? Along the margins these are much more affected by topography. For simulations created within a 1σ range, the highest correlation coefficient is only 0.47 for DS7b. The strong constraint used for these regions, i.e. a prior variance of 0.1 m^2, may cause the approximation to be more determined by this constraint than the simulation. However, if we apply a weaker constraint, i.e. $\lambda=10^6$, the correlation coefficients between **x** and $\hat{\mathbf{x}}$ in these regions remain below 0.5. This means that correcting the

approximation errors using the same method as for the coastal regions may create larger uncertainties. Following Bonin and Chambers (2014), we choose to include the approximation errors in the uncertainties but only for the interior regions. The uncertainties are shown in table A3.2.

3.4.3. Results and discussions

We compared the regional mass changing rate from GRACE with the IOM (figure 3.5) before and after applying the approximation error correction to GRACE and with different discharge estimations implemented by the IOM, separately for coastal and interior regions. For the coastal regions, we find that the correction of the approximation errors in the GRACE solutions adjusts the mass distributions between adjacent mascons. For instance, the corrected mass loss rate in DS3a increases by 10 Gt·yr^{-1} while it reduces the mass loss rate in the adjacent region DS4a by 15 Gt·yr^{-1}. In mascon DS5a, DS6a and DS7a, the combined mass change rate is -107±8 Gt·yr^{-1} before correcting and -106±8 Gt·yr^{-1} after correcting for regional approximation errors. In mascon DS6a correcting for the approximation error causes a mass loss increase of 13 Gt·yr^{-1}.

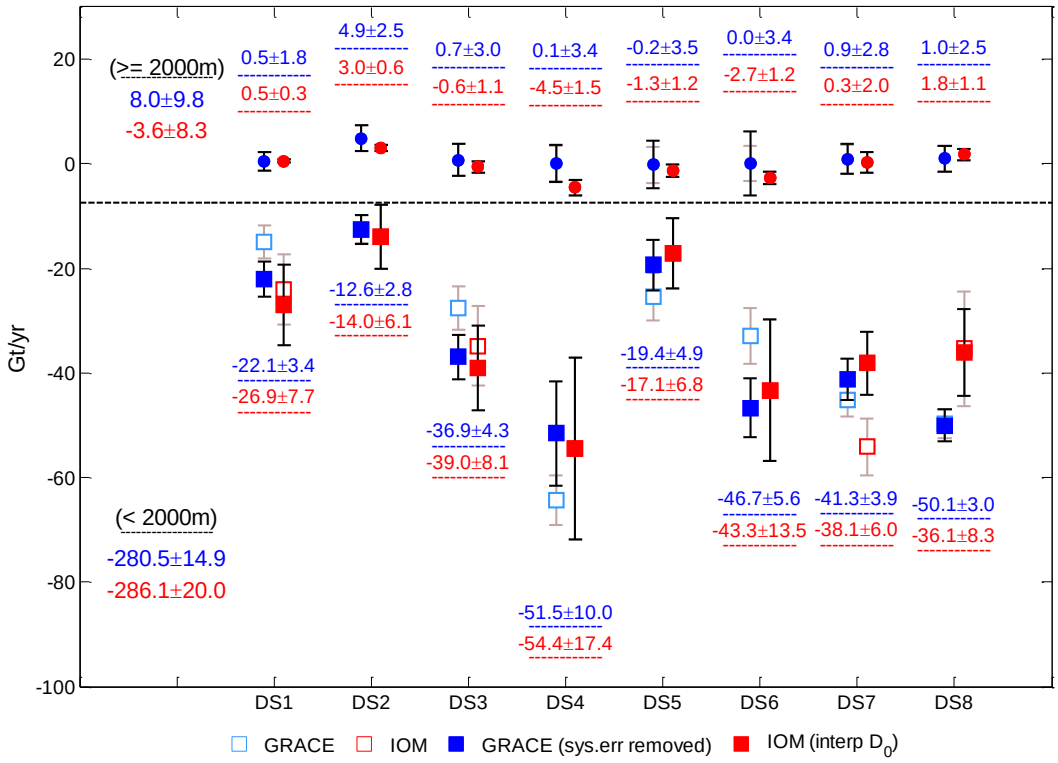

Figure 3.5: Comparison of the regional mass change rates between the GRACE solution and the IOM solutions. Each column refers to one complete basin according to Zwally (2012). The regional mass change rates from GRACE before correcting for the approximation error, are represented by the light blue hollow squares; the filled dark blue squares indicate the mass change rates after implementing the correction. The numbers show the mass change rates in blue and red colour which indicate the GRACE solution and IOM solution respectively. The dashed line separates the solutions from the interior regions (above the dashed

line) from the coastal regions (below the dashed line). The error bars are estimated in section. A3.4.

In the IOM used in the comparison, we only consider TMB in order to reduce the influence of the individual uncertainties in SMB and D. We obtain two IOM solutions, using the reference D_0 by Rignot[08] (method 2) and the interpolated discharges based on RACMO2 runoff (method 3). In mascon DS1a and DS3a, we obtain lower discharge changes rate from method 3 than from method 2. In mascon DS7a, which includes Jakobshavn glacier, method 3 results in smaller mass changes than method 2.

Figure 3.5 shows that agreement between GRACE and IOM improves after correcting the GRACE approximation errors and applying the runoff based discharge estimations in mascon DS3a, DS5a, DS6a and DS7a. The difference between GRACE and IOM estimates is also reduced in DS1a and DS2a, where the remaining difference falls within the uncertainty margins. The corrected GRACE solution in DS4a is only ~3 $Gt \cdot yr^{-1}$ lower than the IOM solution while it was 10 $Gt \cdot yr^{-1}$ higher before correcting the approximation error. However, regardless of correcting the approximation errors, the GRACE inferred regional mass balance agrees with IOM mass balance in DS4a due to the large uncertainties in the GRACE solution and the RACMO2 model there, i.e. ±17 $Gt \cdot yr^{-1}$ (see table A3.2). From figure 3.5 we can also make some inferences about the effect of using different methods to estimate reference discharge. Only in mascon DS8a, IOM and GRACE do not agree within the uncertainties. Previous studies, e.g. Bolch et al. (2013) and Gardner et al. (2013), show that approximately 40 $Gt \cdot yr^{-1}$ mass losses are from the peripheral glaciers. Yet, these portions of mass losses are not considered in our IOM solution. However, given the relationship we found in our discharge data between glacier width and area for the ice sheet's marine-terminating glaciers, we suspect the discharge from these glaciers is quite small and the regional mass changes in these glacier areas are dominated by changes in SMB. Ideally, the GRACE-IOM difference will likely be on the order of single digit $Gt \cdot yr^{-1}$ due to the exclusion of discharge from peripheral marine-terminating glaciers and ice caps as long as we consider the SMB for the whole of Greenland, not just the ice sheet.

For the regions above 2000 m altitude, GRACE inferred regional mass change rates agree with the RACMO2 SMB estimations within uncertainties (see figure 3.5). A noticeable mass increase appears in both GRACE and IOM solutions in mascon 2b (northeast interior). A second observation is that in the IOM, the runoff dominates the regional mass balance on the edge of the southern GrIS interior resulting in mass loss of -8 $Gt \cdot yr^{-1}$. The overall IOM uncertainties in the coastal regions are mainly influenced by the uncertainties in SMB and D estimates, meanwhile applying F^{2000} assumptions contributes additional uncertainties in the GrIS interior regions. In the GRACE solution, the uncertainties are due to the errors in the GRACE coefficients which is not dependent on the altitude, therefore the uncertainty level is similar to the coastal regions.

We also compare our GRACE and IOM solutions to 1) GRACE 2) IOM 3) ICESat altimetry estimates, as shown in table 3.1. All listed GRACE solutions agree within uncertainty levels in DS1, DS2, DS3, DS5 and DS8. In-line with some of the referenced studies, we combine DS6 and DS7. We find a larger rate of mass loss in this area compared to other studies (i.e. -87±10 $Gt \cdot yr^{-1}$) because a longer time interval is considered in this study and mass loss accelerates by ~-21 $Gt \cdot yr^{-2}$

during the time gap between different comparing periods. After accounting for this acceleration, all GRACE solutions become similar in this combined region.

In the southeast region DS4, the regional acceleration of mass loss is negligible (~-0.1 Gt·yr^{-2}). When comparing different GRACE solutions, the mass loss rate in DS4 ranges from -28±7 Gt·yr^{-1} to -51±6 Gt·yr^{-1}. It suggests that a large approximation error, which is associated with different approximation approaches, is likely present in this region in the GRACE solution. As shown in figure 3.5, the regional mass change is reduced by 29% in this region after applying the correction.

Table 3.1: Linear trends in the mass changes in GrIS regions based on satellite gravity data (GRACE), IOM output and altimetry data (ICESat). The unit is Gt•yr^{-1}. The studies are: Zwally et al., 2011; Sasgen et al., 2012; Barletta et al., 2013; Colgan et al., 2013; Groh et al., 2014; Andersen et al., 2015; Sørensen et al., 2011.

Basin	DS1	DS2	DS3	DS4	DS5	DS6	DS7	DS8
	GRACE							
This study （2003–2013）	-22±4	-8±4	-36±5	-51±6	-20±6	-47±8	-40±5	-50±4
Colgan (2003–2010)	-21±6	1±6	-47±13	-28±7	-24±4	-33±7	-23±9	-42±12
Sasgen (2003–2010)	-16±5	-12±5	-38±6	-42±6	-24±6	-56±7		-53±7
Barletta (2003–2012）	-17±2	-12±2	-36±4	-35±3	-23±2	-66±4		-44±4
	IOM							
This study (2003–2013)	-26±8	-10±6	-39±8	-59±18	-18±7	-46±14	-38±6	-35±8
Andersen (2007–2011)	-17±5	-13±6		-38±29	-20±9	-53±13	-53±17	-58±14
Sasgen (2003–2010)	-20±4	-16±5	-31±8	-66±21	-20±7	-66±20		-26±12
	ICESat							
Zwally -11 (2003–2007)	1±0	13±0	-51±1	-75±2	-10±0	-4±0	-14±0	-33±1
Sørensen (2003–2009)	-16±1	-16±3	-40±18	-43±11	-26±5	-51±7		-53±3

The IOM is also relatively uncertain in DS4 (Sasgen et al., 2012). Even though the mass-change rates between GRACE and the IOM in this region show a relatively large difference, agreement is obtained within the large uncertainties. For ICESat-based mass loss estimates, the retrieved long-term mass loss can be very different, e.g., -75±2 Gt·yr^{-1} by Zwally et al. (2011) compared to -43±11 Gt·yr^{-1} by Sørensen et al. (2011). This may be explained by the complicated regional ice surface geometry in the coastal areas (Zwally et al., 2011) or uncertainty resulting from the conversion of height changes to mass change, e.g., different firn corrections and density conversions. Another area where GRACE and the IOM do not agree is the northwest (region DS8). We find that our GRACE solution shows -32±6 Gt·yr^{-1} mass change during 2003–2007 and -46±5 Gt·yr^{-1} during 2003–2010. The ICESat solutions show similar mass loss rates in this region (see table 3.1), while the IOM solution shows lower mass change rates, i.e., -13±3 Gt·yr^{-1} and -28±6 Gt·yr^{-1} for the time period 2003–2007 and 2003–2010, respectively. Moreover, if we determine the mass change rates for the time interval from 2007–2011, the rate is -57±6 Gt·yr^{-1} (GRACE) and -49±11 Gt·yr^{-1} (IOM). Both results agree with the rate of -58±14 Gt·yr^{-1} from Andersen et al. (2015).

We have reduced the approximation error in the GRACE solution for this region, although by a

small amount (-2.3 Gt yr^{-1}). To assess the influence of the remaining approximation errors, we compare the GRACE and IOM solutions in the surrounding areas, i.e., DS1 and DS7. It can be seen in Fig. 5 that mass change rates are consistent between IOM and GRACE solutions, within their uncertainties. This suggests that the approximation errors become negligible in the GRACE solution. The comparison for Ellesmere Island is more difficult because discharge is not included in our IOM solution. However, an IOM solution including the D estimates by Gardner et al. (2011), showed that the mass change rate of the glaciers on this island is 37±7 Gt yr^{-1} between the years of 2004 and 2009. This agrees (to within its uncertainty bound) with our solution for the same time interval, i.e., -35±7 and -29±3 Gt yr^{-1} for IOM and GRACE solutions, respectively. Hence, it is reasonable to believe the mass change estimated from IOM and GRACE agree with each other in this region. After comparing the GRACE and IOM solutions on all the neighbor regions of DS8, no significant differences between the IOM and GRACE solutions are found. This suggests that the remaining approximation error is not the major source of the difference in DS8.

The uncertainties of the GIA effect are included as part of the uncertainties of the GRACE solution for this region as well (see table A3.3), but adding these still cannot bridge the gap between GRACE and IOM. The ICESat-based mass change estimate by Kjeldsen et al. (2013) yields a mass loss rate of 55±8.4 Gt·yr^{-1} from 2003 to 2010, which is consistent with the GRACE solution in this study. All evidence combined indicates that the IOM method underestimates the mass loss rate in this basin by ~-15 Gt·yr^{-1}. In Sasgen et al. (2012), the discharge estimations from Rignot[08] are used, in which a portion of DS8 was un-surveyed, to which they ascribed the difference between GRACE and IOM (24±13 Gt·yr^{-1}). In this study, the discharge estimation from Enderlin et al. (2014) covers the entire glacier area in this region, but only for the years after 2000. Therefore, despite observations of relatively stable terminus positions for the majority of the marine-terminating glaciers in northwest Greenland between 1985–2000 (Howat and Eddy, 2011), we hypothesize that the estimated reference discharge over-estimates the regional D_0. Deriving D_0 from D-14 involved the assumption that D from 1990 to 2000 follows Rignot[08], which contains high regional uncertainties. On the other hand, if we use the runoff-based estimate of D_0, uncertainties are influenced by the uncertainty of the RACMO2 model. The SMB inter-comparison study of Vernon et al. (2013) shows that the 1961–1990 reference SMB_0 of RACMO2 model is larger than some other SMB models, e.g. MAR or PMM5. It is interesting to see that when the cumulative TMB is calculated independently from the reference SMB_0 and D_0 (using Eq 3.5, method 1), the mass change rates agree with the GRACE mass balance in this region within uncertainties. This indicates that modelled SMB (as well as SMB_0) could have uncertainties that are larger than 18%.

3.5. Conclusions

In this study, we implement a simulation of GrIS mass changes and show that the approximation errors caused by the least-squares inversion approach can be quantified and furthermore be reduced in the GRACE solution. For using the IOM, we apply an improved reference discharge estimate that can better agree with other independent estimates. We show that the regional differences

between our GRACE and IOM solutions are reduced and agree within the calculated confidence intervals. This is confirmed by an inter-comparison with ICESat based regional mass change rates. In the southeast, the corrections for the approximation errors in GRACE are especially important. We find that the IOM solutions underestimate mass loss in the northwest compared to GRACE and ICESat solutions, which we attribute to incorrect estimates in reference D and/or SMB used to construct the IOM estimates. For the whole GrIS and considering the early half of the comparison time window, we find a 208±18 $Gt \cdot yr^{-1}$ mass loss rate for the period 2003 to 2008 from the GRACE solution, while the IOM solution shows a mass loss rate of 195±25 $Gt \cdot yr^{-1}$. The loss rates increase by ~67% and ~85% in 2009–2014 in the GRACE and IOM solutions, respectively. The 10-year acceleration in the GRACE data is -25±8 $Gt \cdot yr^{-2}$, consistent with the IOM solution, -26±12 $Gt \cdot yr^{-2}$.

Acknowledgements. This research is funded by means of scholarship GO-AO/27 provided by the Netherlands Organization of Scientific Research, NWO. We are grateful to Ian Joughin for the suggestions of estimating the ice flux at high elevation. Furthermore the authors acknowledge the thoughtful comments by Etienne Berthier and three other anonymous referees of this manuscript.

Appendix A

A3.1. Reference discharge based on the pre-1960 discharge estimations

The GrIS ice discharge D was distributed into 34 glaciers by Rignot et al. (2008), denoted by D-08. The reference discharge D_0-08 is considered equivalent to the discharge estimation for the year of 1996. We define the reference discharge in 1996 and 2000 as D_0-08 and D_{2000}-08, respectively. The deviations between D_0-08 and D_{2000}-08 are due to the discharge changes in late 1990s (Enderlin et al., 2014). Similarly, we define Enderlin[14] as D-14, with the time series starting from the year of 2000 (D_{2000}-14). In order to estimate the reference discharge D_0-14, we find scaling factors between D_0-08 and D_{2000}-08 and scale the D_{2000}-14 to yield the estimation of D_0-14. We estimate the uncertainties of estimated D_0-14 via 500 pairs of randomly generated $\widetilde{D}_0$-08, $\widetilde{D}_{2000}$-08 and $\widetilde{D}_{2000}$-14, following from the normal distribution N (D, σ_D), in which σ_D is the error in the discharge estimations. For the entire GrIS, we find that the interpolated $D14_0$=413.8±31.6 Gt, similar to previous studies. (Sasgen et al., 2012; van den Broeke et al., 2009)

A3.2. Approximation error correction

In order to determine the linear relationship between the simulated regional mass balances with the associated approximations after applying the least-squares inversion, the linear fitting parameters α_0 and α_1 are calculated for different simulation error levels, the values of which are shown in table A3.1. The values of α_0 and α_1 and their uncertainties vary slightly in all coastal regions. In order to determine one value for α_0 and α_1, we assume the α_0 and α_1 follow the normal distribution in each region and draw 1000 random samples for each error level. Then we combine all the samples and fit into another normal distribution, from which the α_0 and α_1 are determined for each region (see the table A3.1).

A3.3. The GrIS simulation

The GrIS monthly mass balance simulations that will be used in section 3.4.2 are based on the RACMO2 model and the discharges estimates from Enderlin et al., (2014). Note that the discharge estimates are given the form of lumped mass change for 178 different geographical locations. To get SMB and D estimates for each basin we sum the discharges for all glaciers or the gridded SMB values within each basin, respectively. We interpolate SMB and D onto a gridded map of EWH with a resolution of 1 arc degree for the GrIS and surrounding areas. To account for leakage from outside the GrIS, as occurs in GRACE, we apply the annual mass changes estimates from Schrama et al. (2014) for all the major glacier areas (GrIS excluded). We convolve the gridded mass distribution over the Earth's surface and obtain the potential coefficients in response to this distribution up to d/o 60. Noise in the monthly GRACE coefficients manifests mainly as north-south stripes in the spatial domain (Swenson and Wahr, 2006). In order to mimic this error in the simulation, we add randomly generated noise as described in Bonin and Chambers (2013) to the potential coefficients. The simulation model was discussed in details in Xu et al., (2015). Note that for this study we focus on the discussion of long-term linear trend, thus the linear trend of the monthly simulation is used as the simulation model for later use.

A3.4. Uncertainty estimations

A summary of the uncertainties in the regional mass balance (linear trend) is shown in table A3.2. In our GRACE inferred mass balance, the uncertainties are associated with 1a) the standard deviations of the CSR RL05 GRACE spherical harmonics coefficients (including the standard deviations of the external degree l=1 and 2 coefficients), 2a) the variations of the regional mass changes due to different GIA models and 3a) the uncertainties due to the corrections of the systematic error in the least-squares inversion solutions. The uncertainties of the IOM inferred mass balance consist of the uncertainties of the 1960 – 1990 reference in SMB_0 and in D_0 and 2b) the systematic error in the SMB (RACMO2) and 2c) the errors in the yearly D estimations (Enderlin 2014 and Rignot 2008).

A3.5. Selection of the GIA model for GrIS regions.

We apply the GIA correction to the GRACE data using 11 different GIA models before estimating the associated regional mass changes in 20 GrIS and surrounding Arctic regions (see the mascon definition in section 3.3). By comparing with one without applying GIA correction, we assume the differences are the regional GIA effects. In addition to Paulson-07 GIA model, we use a GIA model with lateral changes in viscosity and the ICE-5G loading history (van der Wal et al. 2013).

Moreover, we use 8 different GIA models based on the ice history model from Simpson et al. (2009), provided by Glenn Milne within the scope of the IMBIE project. The upper mantle viscosity ranges from 0.3×10^{21} to 1×10^{21} Pa·s and the lower mantle viscosity ranges from 1×10^{21} to 10×10^{21} Pa·s. The thickness of the lithosphere is assumed to be 96 km or 120 km.

In table A3.3, the GIA related mass changes can vary from -7 $Gt\cdot yr^{-1}$ to 10 $Gt\cdot yr^{-1}$ for the entire GrIS. A positive GIA effect appears in the northern GrIS while in the south and southwest GrIS, (DS5a to DS7a) negative GIA signals prevail.

In order to quantify the uncertainties of the regional GIA in the Paulson-07, since it is the GIA model we used to derive our GRACE solution, we estimate the standard deviation of all models with respect to Paulson-07. The uncertainties are summarized in table A3.3.

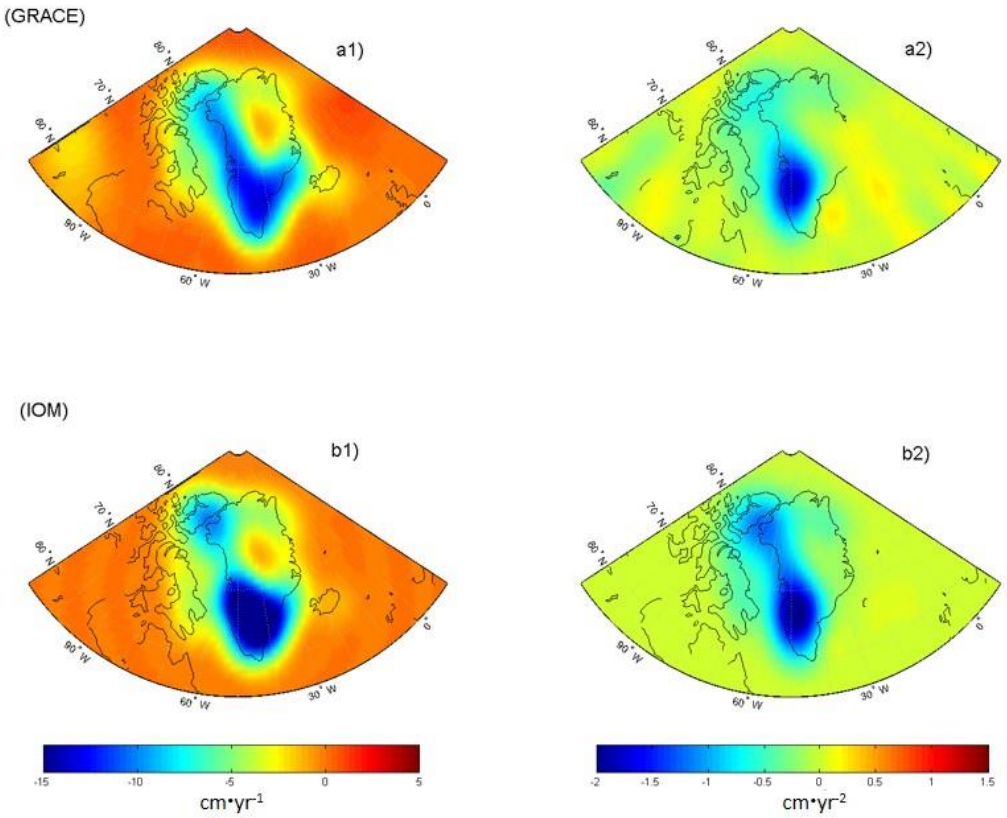

Figure A3.1: The EWH of the linear trend (a1) and accelerations (a2) in CSR release 5 level 2 GRACE data. The linear trend (b1) and the accelerations (b2) of IOM solution in EWH. The time interval is from Jan 2003 to Jan 2012. The Gaussian filter half width in all plots is $r_{1/2}$=300 km.

Table A3.1: The linear fit parameters α_0 and α_1 describing the relationship between the regional simulated mass balance and the approximations obtained after the inversion procedure as applied to GRACE data of the coastal regions. For the interior GrIS regions, we show the approximation errors as additional uncertainties.

mascon (< 2000 m)	DS1a	DS2a	DS3a	DS4a	DS5a	DS6a	DS7a	DS8a
α_0 (Gt)	-10.93±1.46	-0.64±0.54	6.82±1.47	-14.90±1.54	-1.86±1.61	-17.15±1.54	2.54±2.23	0.28±1.02
α_1	0.85±0.03	1.02±0.02	0.95±0.01	0.96±0.02	0.90±0.01	0.90±0.02	0.97±0.01	1.00±0.01
mascon (>=2000 m)	DS1b	DS2b	DS3b	DS4b	DS5b	DS6b	DS7b	DS8b
uncertainty (Gt yr)	0.28	0.35	0.45	0.6	2.88	5.1	0.67	0.65

Table A3.2: The uncertainties associated with the regional mass change rates. For the GRACE inferred regional solutions, "coef.std" refers to the errors due to the standard deviations in the CSR RL05 spherical coefficients, "GIA" refers to the errors obtained from comparing 11 GIA models. Note that the GIA uncertainties in the interior GrIS are all close to 0 thus they are neglected. In the column with the header "Cor" we show the uncertainties which are caused by the approximation error correction. For SMB and D trend estimations, the uncertainties consist of the reference SMB_0 and D_0 error ("SMB_0" and "D_0") and the systematic errors in RACMO2 model and in the discharge estimations ("sys"). The column entitled with "Cum. Uncer" refers to cumulative uncertainties using the assumptions 1) and 2), see the details in section. 3.2. The highlighted columns show the total uncertainties of the linear fit of the GRACE and IOM mass balances.

Mascon	GRACE				RACMO2 (SMB)			Discharge (D)			Cum.Uncer	IOM
	coef.std(1a)	GIA (2a)	Cor (3a)	Total	SMB_0 (1b)	Sys (2b)	Total	D_0 (1c)	Sys (2c)	Total	Apply assum. 1) and 2)	SMB-D
DS1a	1.9	3.9	1.6	3.4	1.9	7.2	7.6	0.8	0	0.8	1.1	7.7
DS2a	2.1	2.2	0.6	2.8	1.6	5.8	6	1.1	0.3	1.1	2.9	6.8
DS3a	3.2	3	1.5	4.3	3.6	6.8	7.8	2	1	2.2	2.1	8.4
DS4a	3.8	2.6	8.8	10	8.6	10.6	17.1	3.1	1.4	3.4	1.6	17.5
DS5a	4.4	0.2	1.7	4.9	3.9	5.2	6.7	1.1	0.7	1.2	0.8	6.9
DS6a	3.7	0.8	1.7	5.6	4.7	12.5	13.4	0.6	0.3	0.6	1.4	13.5
DS7a	3	0.5	2.2	3.9	2	4.9	5.4	2	1.5	2.5	4.9	7.7
DS8a	2.4	3.7	1.1	4.5	3.3	7.7	8.3	2.1	1.1	2.4	2.3	8.9
Coastal	9	7.3	4.5	14.9	12.1	22.6	27.7	4.9	2.7	5.5	15.4	32.2
DS1b	1.8		0.3	1.8	0.3	0.1	0.3				1.1	1.1
DS2b	2.4		0.4	2.4	0.6	0.2	0.6				2.9	3.0
DS3b	3		0.5	3	1	0.3	1.1				2.1	2.4
DS4b	3.4		0.6	3.5	1.5	0.3	1.5				1.6	2.2
DS5b	3.5		2.9	4.5	1.1	0.3	1.2				0.8	1.4
DS6b	3.4		5.1	6.1	1.2	0.4	1.2				1.4	1.8
DS7b	2.8		0.7	2.9	1.8	0.6	2				4.9	5.3
DS8b	2.4		0.7	2.5	0.9	0.4	1.1				2.3	2.5
interior	7.8		6	9.8	8.1	1.7	8.3				15.4	17.5
GrIS	11.9	7.3	7.5	17.8	14.5	22.7	28.9	4.9	2.7	5.5	0	29.4

Table A3.3: The GIA effects on mass balance in different GrIS regions based on 11 different GIA models. The unit is Gt yr^{-1}. For the GIA models using Simpson's ice history model, the column headers are in the form of "*x*p*ab*", where the *x* value refers to the lithosphere thickness (km), and a and b represent the viscosity of the upper and lower mantle, in 10^{20} and 10^{21} Pa·s respectively.

ICE model	ICE-5G	Wouter van der Wal		Simpson							
Mascon	Paulson-07	heatflow	seismic	96p32	96p55	96p58	96p85	96p510	120p51	120p81	120p11
DS1a	4	5	2	1	-1	-1	-1	0	3	4	4
DS2a	3	1	1	1	1	1	2	2	2	3	3
DS3a	0	2	-1	1	-1	-2	-1	-1	2	3	3
DS4a	0	3	1	-1	0	0	1	1	1	3	4
DS5a	-3	-1	0	-5	-8	-7	-7	-7	-4	-4	-5
DS6a	-2	1	2	-5	-2	-2	1	-2	-3	-1	0
DS7a	-3	0	0	-1	-5	-5	-6	-5	-2	-2	-3
DS8a	-1	-1	0	1	-1	-2	-2	-2	-1	-2	-2
Ellesmere	7	4	4	1	2	3	4	3	4	5	6
Baffin	12	-3	6	10	12	12	12	13	1	0	-1
Iceland	-1	0	-1	-1	-3	-3	-3	-3	0	0	-1
Svalbard	2	0	2	2	3	4	3	5	0	0	0

Chapter 4

Regional Greenland ice sheet mass changes based upon a hierarchical mascon constraining method

Abstract

In this study, we derive regional mass changes for 19 regions in Greenland and 4 surrounding glacier areas from GRACE using a least-squares inversion approach. The method of constraining the solution is to a large extent independent from priori information about the study area. The method considers two levels of mascons: 19 smaller mascons which are the target areas, and larger mascons which consist of several of the smaller mascons. The idea of the method is to use the inverted mass changes of the larger mascons, which are less susceptible to inversion instability, to govern the least-squares solution of the smaller mascons. We validate this method using a GrIS simulation based on modelled surface mass balance (SMB) and an ice discharge estimate. The results show a significant improvement in most of the GrIS sub-basins after applying the proposed hierarchical constraint method, compared to a least-squares solution based on a single constraint. Finally, we apply our method to GRACE data to investigate the mass loss in the 19 GrIS regions.

Key words: GRACE, mascons, small region mass changes, hierarchical constraints

4.1. Introduction

The Gravity Recovery And Climate Experiment (GRACE) satellites observe mass changes on the Earth's surface by measuring the gravitational field changes over time. GRACE data have been used to derive the mass changes relating to ice melt on Greenland (Shepherd et al., 2012, Schrama et al., 2014; Velicogna et al., 2014; Anderson et al., 2015; Wiese et al., 2015; Colgan et al., 2015; Alexander et al., 2016; Schlegel et al., 2016; and Ran et al., 2017). In order to extract the GrIS regional mass changes signal from the GRACE data, a least-squares inversion approach can be used (Wouters et al., 2008; Sasgen et al., 2010; Schrama and Wouters, 2011). The inversion approach divides the GrIS in several regions or mascons with a pre-defined mass distribution. This method requires the conversion of the mass changes for a single mascon to changes of the gravitational field. The scale of the uniform mass distribution in the mascons is adjusted to fit the observed gravity field changes. Among several inversion methods, the basin-averaged least-squares inversion by Schrama and Wouters (2011) is a simple but effective inversion approach to study the mass changes in GrIS regions, see applications in Bonin and Chambers (2013) and Xu et al. (2015). Some other studies assumed the non-uniform distributed mass for the GrIS mascons but this has the drawback of relying on the prior knowledge of mass change in these areas (Wouters et al., 2008 and Sasgen et al., 2012). The regional mass changes approximations derived from the basin-averaged least-squares inversion are consistent with other independent regional mass changes estimates such as the Input-output Method (IOM) and satellite altimetry (Sasgen et al., 2012; Shepherd et al., 2012; Velicogna et al., 2014 and Xu et al., 2016). Recent developments towards smaller mascons are discussed and their shortcomings are specified. After that we present a new method for obtaining constraints which depend less on a priori information than earlier methods.

Bonin and Chambers (2013) find that the least-squares inversion method is sensitive to the geometric definition of mascons. Their closed-loop simulated showed that when approximating simulated GrIS mass change with different mascon definitions, the approximation-to-simulation residual varies with mascon. Bonin and Chambers (2013) found that it is best to define the mascons according to hydrological drainage systems (DS). Furthermore, as introduced by Schrama and Wouters (2011), a priori information on the variance of the regional mass changes can be used to constrain the approximations. Without priori information on the magnitude of the constraint, a very weak constraint can be applied in order to remove most of the numerical instability during the inversion. In Bonin and Chambers (2013) a constant variance for all mascons is considered which is optimized based on a simulation of GrIS mass change. Based on a similar simulation Xu et al. (2015) showed that the approximation derived from the least-squares inversion sometimes results in negative correlation of mass changes in neighboring basins. This negative correlation is not necessarily a physical signal in the GRACE data but results from instability in the approximation for small mascons. In Xu et al. (2016), the negative correlation is recognized as the error, or approximation error. In Xu et al. (2015) the approximation error is reduced by using different constraints for different regions, for instance a small variance for mass changes in the higher elevation GrIS regions where run-off is small (Colgan et al., 2015) and larger variances for the

coastal areas which lose ice more rapidly through discharge and runoff (Andersen et al. 2014).

There are several drawbacks of this constraining method: 1) Since the constraints depend on the location of mascons, changing the definition of mascon requires finding new constraints based on simulation, 2) The method relies on priori information about the variance of mass changes in the study area which might not be reliable in all situations, 3) It is computational expensive to optimize the location dependent constraints for a large number of mascons (Xu et al., 2015).

In this study we introduce a new method to constrain the least-squares inversion approach which is not necessary to depend on establishing a simulation or the priori information of the study area but still reduces the negative correlation error. First the least-squares inversion set-up is introduced in section 4.2. Then the new constraining method is explained in section 4.3. Before diving into the smaller areas in GrIS, we investigate the limitation of the spatial resolution of GRACE data in section 4.4. The mass change estimates from the new method are discussed in section 4.5.

4.2. Least-squares inversion

In this study, we will employ a simulation of monthly spherical harmonics similar to the GRACE data; the detail of the simulation is in section A4.1. We follow the least-squares inversion method of Schrama and Wouters (2011) to approximate the mass changes in GrIS basins:

$$\mathbf{y} = \mathbf{A}\boldsymbol{\alpha} + \boldsymbol{\varepsilon}, \tag{4.1}$$

where the observation vector **y** is the global equivalent water height (EWH) map derived from the spherical harmonic coefficients associated with the mass distribution on the Earth's surface. The method of calculating the EWH map from the spherical harmonics is given by Wahr et al., (1998). The design matrix $\mathbf{A} = [\mathbf{a_1}, \mathbf{a_2} \dots, \mathbf{a_n}]$ contains column vectors $\mathbf{a_i}$ which are influence functions of the pre-defined mascons. In this study we assume a constant 1 m height water layer uniformly distributed across the mascons, and mascons corresponding to drainage systems. $\mathbf{a_i}$ can be obtained by converting the spherical harmonics to EWH in the spatial domain using the same method of deriving the EWH maps from the observations. Note that this means the same filter as used for the observations has to be applied to the influence functions (Wouters et al, 2008). The parameter vector $\boldsymbol{\alpha} = [\boldsymbol{\alpha}_1, \boldsymbol{\alpha}_2, \dots, \boldsymbol{\alpha}_n]$ contains the scaling factors associated with each mascon. $\mathbf{A}\boldsymbol{\alpha}$ represents the approximation of mass changes of the whole GrIS. The observation-to-approximation difference is given by $\boldsymbol{\varepsilon}$.

The least-squares solution of equation (4.1), subject to constraints, is:

$$\hat{\boldsymbol{\alpha}} = (\mathbf{A}^{\mathrm{T}}\mathbf{A} + \sigma^{-1}\mathbf{I})^{-1}\mathbf{A}^{\mathrm{T}}\mathbf{y} \tag{4.2}$$

where $\sigma^{-1}\boldsymbol{I}$ is a regularization term [*Tikhonov*, 1963] which constrains the approximation $\hat{\boldsymbol{\alpha}} = [\hat{\alpha}_1, \hat{\alpha}_2, \dots, \hat{\alpha}_n]$ and reduces the numerical instability during the least-squares approach as described in (Schrama and Wouters, 2011 and Baur and Sneeuw, 2011). We do not consider a covariance matrix of the equivalent water height thickness data in vector **y** other than an identity matrix. Schrama et al. (2007) used a full covariance matrix and demonstrated it does not adequately explain the full error structure in the equivalent water height maps. More recent estimates of full noise

covariance matrices have been used in inversion or regularization procedures (Klees et al., 2008 and Sabaka et al. 2010). The results of such a procedure are highly dependent on the accuracy of the covariance matrix. Here we proceed to show our method in an inversion.

In order to verify the feasibility of this method, we will use this inversion method to approximate the regional mass changes and compare it to the estimates derived according to the methods of chapter 2 and chapter 3. In this chapter, a single constraint σ is used. The magnitude of σ will be discussed later in this chapter.

4.2.1. Mascons

The shape and position of the mascons have a noticeable effect on regional mass changes estimates as was explained by Bonin and Chambers (2013). Following Bonin and Chambers (2011) we define the mascons to be the drainage systems (DS) and sub-drainage system (sub-DS). Here the definition of Zwally et al. (2012) is used (see figure A4.2). According to this definition, there are 8 major GrIS DSs; each of them can be further divided by several smaller sub-DSs with distinguishable surface characteristics related to the atmospheric advection (Zwally et al., 2012). Following this definition, there are 18 sub-DS in total. DS5 is the only DS with no sub-DS, and it will be considered as one sub-DS. Wouters et al. (2008) showed that the glacier regions surrounding Greenland, which are Ellesmere Island, Baffin Island, Iceland and Svalbard (hereafter, EBIS), also influence the approximation for the GrIS. Therefore, the EBIS regions are included as 4 separate mascons in our inversion.

The position of each mascon is mapped onto a grid. It may happen that different portions of a cell belong to different mascons when this cell is situated on the boundary of two mascons, or a cell is located at the edge of Greenland. For the first problem, we choose to assign the conflicting cell to the mascon which contributes the largest area in this cell; and for the latter problem the cell will be recognized as a mascon cell when it is partially situated on Greenland. The influence of the grid resolution is investigated in section 4.4.1.

4.2.2. Global spherical harmonic analysis and filtering

In the beginning of the mission, GRACE level-2 data consist of spherical harmonic coefficients up to maximum degree and order 60. Later GRACE level-2 solutions (release 5 of the CSR) include higher degree and order potential coefficients. In our studies in chapter 2 and chapter 3, we estimate the mass changes of 8 drainage regions as defined in Zwally et al. (2012). However, in this study, smaller mascons are considered. Thus, to better preserve the signal in these mascons, level-2 data produced by the University of Texas Center for Space Research (CSR) up to degree and order 96 are used to define the equivalent water thickness data, which is **y** in equation (4.1).

GRACE level-2 spherical harmonics coefficients at increasing degree and order are more likely to contain noise. In the spatial domain, the GRACE noise manifests as north-to-south directed “stripes” (e.g. Swenson and Wahr 2006). To reduce the stripes, a homogenous Gaussian filter with a certain smoothing radius $r_{1/2}$ is applied to the spherical harmonic coefficients (Swenson and Wahr, 2003).

4.3. Hierarchical constraint method

In this section, we will demonstrate a constraining method which is not dependent on priori information of the study area, e.g. a simulation of GrIS. Firstly, we need to explain the definition of the "levels" of mascons. For instance, when a mascon can be further divided into several small within mascons, then the "mother" mascon is considered as a high level mascon and the "off-spring" mascons are the low level mascons. The main concept of our new method, is to use the inverted approximation of the high level mascons to constrain the inversion for enclosed low level mascons. The reason is that we expect reduced approximation errors in mass changes estimates of the high level mascons

4.3.1. Inversion of two levels of mascons

Inversion of small (LL) mascons

We label the set of 23 smallest mascons as low level (LL) mascons, see also the mascon map in figure 4.1. The corresponding influence functions are $\mathbf{A}_{\boldsymbol{LL}} = [\boldsymbol{a}_{\boldsymbol{LL1}}, \boldsymbol{a}_{\boldsymbol{LL2}}, \dots, \boldsymbol{a}_{\boldsymbol{LL23}}]$, where $\boldsymbol{a}_{\boldsymbol{LLi}}$ refers to the influence function for LL mascon $\boldsymbol{i}$ and the estimated scaling factors with respect to each pre-defined mass distribution equation (4.2), are $\widehat{\mathbf{X}}_{\boldsymbol{LL}} = [\hat{x}_{LL1}, \hat{x}_{LL2}, \dots, \hat{x}_{LL23}]$. We multiply the scaling factor $\widehat{\mathbf{X}}_{\boldsymbol{LL}}$ with the associated mass distribution and the area of each mascon to yield the approximated regional mass changes $\widehat{\mathbf{M}}_{\boldsymbol{LL}} = [\hat{m}_{LL1}, \hat{m}_{LL2}, \dots, \hat{m}_{LL23}]^{\mathrm{T}}$ in units of Gt. The relationship between an individual mass in each mascon and the overall mass for the entire GrIS is:

$$\mathbf{h}_{\boldsymbol{LL}}\widehat{\mathbf{M}}_{\boldsymbol{LL}} = \hat{M}_{\mathrm{gris}} \qquad \textbf{(4.3)}$$

$\hat{M}_{\mathrm{gris}}$ refers to the approximated mass changes for entire GrIS when $\boldsymbol{h}_{\boldsymbol{LL}} = [1,1,\dots,1]$. Note that at this stage the approximation for each individual mascon is only constrained by the pre-determined scaling factor $\widehat{\boldsymbol{\alpha}}$ in equation (4.2).

Inversion of large (HL) mascons

We combine the LL mascons into larger mascons resulting in a new mascon definition. We define these LL mascon combinations as the high level (HL) mascons. For the HL mascons the negative correlation error will be smaller. Here we investigate if we can use the estimates for the large mascons as constraints for the smaller mascons.

HL mascons can be created from the set of LL mascons in different ways; examples of HL mascons are shown in figure 4.1. In figure 4.1(b), we create HL mascons by combining all the LL mascons according to the DS by Zwally et al. (2011). For instance, the mascon HL1 is constituted of four LL mascons on the northern GrIS, i.e. mascon LL1 to LL4. Note that in this study, the 4 additional mascons representing the EBIS regions are the same for both LL and HL mascons.

In figure 4.1(b) and figure 4.1(c), we show two different ways of forming HL mascons. With the least-squares inversion, we can estimate the regional mass changes for a certain HL mascon definition, i.e. $\widehat{\mathbf{M}}^{\boldsymbol{k}}_{\boldsymbol{HL}} = [\hat{m}^{k}_{HL1}, \hat{m}^{k}_{HL2}, \dots, \hat{m}^{k}_{HLj}]^{\mathrm{T}}$ where k is index for the HL mascon definition

($k \geq 1$), and j is the total number of HL mascons included in this definition. Since each HL mascon consists of one or more LL mascons, the regional mass estimate $\widehat{m}_{HLj}^{k}$ in HL mascon definition k should also be the combination of the mass estimates of the LL mascons that form this HL mascon. Hence the following relationships can be obtained:

$$\mathbf{h}_{HL}^{k}\widehat{\mathbf{M}}_{\boldsymbol{LL}} = \widehat{\mathbf{M}}_{\boldsymbol{HL}}^{\boldsymbol{k}} \qquad \textbf{(4.4)}$$

in which $\mathbf{h}_{HL}^{k}$ is the matrix of the linear coefficients relating the LL mascons to the HL mascons: $\mathbf{h}_{HL}^{k} = [\mathbf{h}_{HL1}^{k}; \mathbf{h}_{HL2}^{k}; \dots; \mathbf{h}_{HL23}^{k}]$, $\mathbf{h}_{HLj}^{k}$ is a 1 by n vector ($1 \leq j \leq n$), which has the value 1 if the LL mascon j ($1 \leq j \leq 23$) is included in the HL mascon k, otherwise the elements are 0. An example of constructing an $\mathbf{h}_{HL}^{k}$ matrix is shown in figure 4.2.

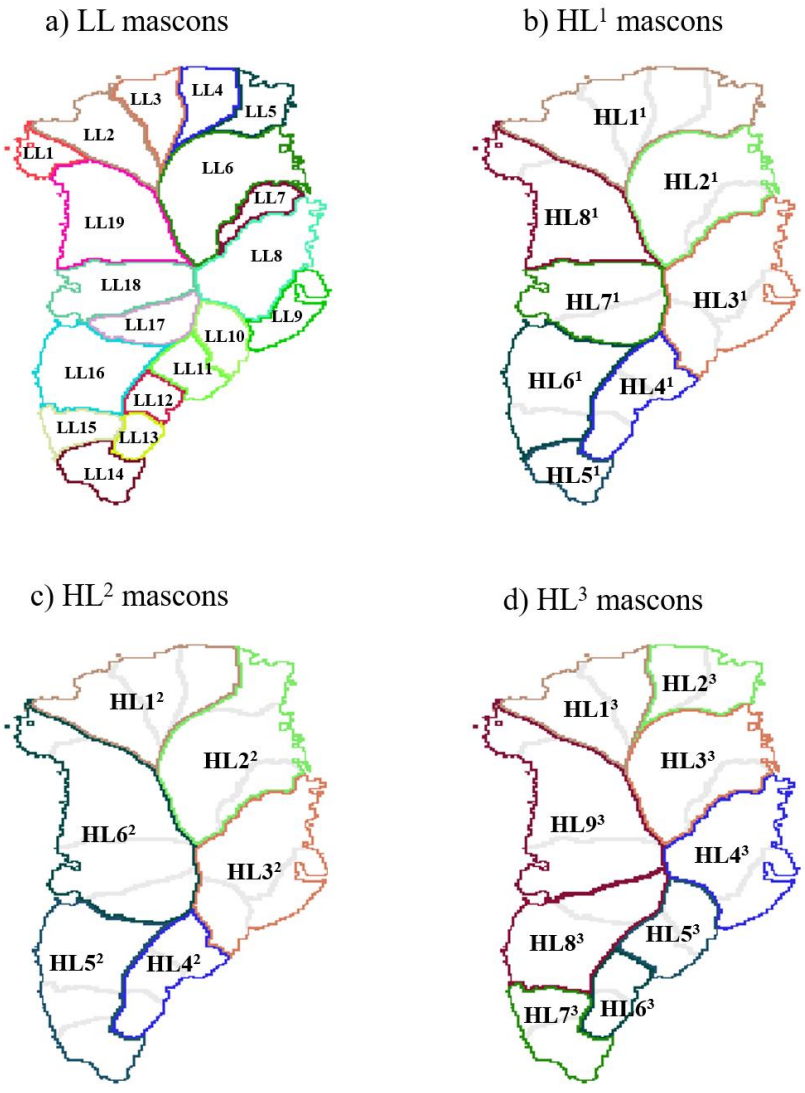

Figure 4.1: Examples of LL and HL mascon definitions. a) L1 mascon definition based on DSs from Zwally et al. (2011), 19 GrIS mascons in total; b) L2 mascon definition with combining the sub-DS to DS. c) and

d) are two different mascon definitions using the rule defined in section 4.3.3, in these two definitions *d*=3 and 4, respectively.

4.3.2. Constraining LL with HL

Since there are n LL mascons and assuming we use l different HL mascon definitions, in total one can find $n \times l$ approximations for HL mascons satisfying equation (4.4). We use more than 1 HL mascon definition to reduce the probability that one particular definition will dominate the approximation error. It is worth mentioning that the same HL mascon may appear multiple times in different HL mascon definitions. We treat these approximations as constraints in equation (4.3):

$$\begin{pmatrix} \mathbf{h_{LL}} \\ \mathbf{h_{HL1}} \\ \vdots \\ \mathbf{h_{HLl}} \end{pmatrix} \begin{pmatrix} \widehat{\mathbf{M}}_{LL} \\ \widehat{\mathbf{M}}_{LL} \\ \vdots \\ \widehat{\mathbf{M}}_{LL} \end{pmatrix} = \begin{pmatrix} \widehat{\mathrm{M}}_{\mathrm{gris}} \\ \widehat{\mathbf{M}}_{\mathbf{HL1}} \\ \vdots \\ \widehat{\mathbf{M}}_{\mathbf{HLl}} \end{pmatrix} \tag{4.5}$$

or

$$\mathbf{H}\widehat{\mathbf{M}}_{\boldsymbol{LL}} = [\widehat{\mathrm{M}}_{\mathrm{gris}}, \widehat{\mathbf{M}}_{HL}]^{\mathrm{T}} \tag{4.6}$$

On the right hand of equation (4.6), mass changes approximations $\widehat{\mathrm{M}}_{\mathrm{gris}}$ and $\widehat{\mathbf{M}}_{HL}$ are the inverted mass changes consisting of HL mascons. $\widehat{\mathrm{M}}_{\mathrm{gris}}$ is the combination of all $\widehat{\mathrm{M}}_{\boldsymbol{LL}}$ which are derived from equation (4.3) and $\widehat{\mathbf{M}}_{HL} = [\widehat{\mathbf{M}}_{\mathbf{HL1}} \ldots \widehat{\mathbf{M}}_{\mathbf{HLl}}]^{\mathbf{T}}$. $\mathbf{H}$ is a matrix that gives the relation between LL and HL mascons. We solve equation (4.6) using the least-squares approach and the result is $\widehat{\mathbf{M}}'_{\boldsymbol{LL}}$ which is not only derived from the LL inversion, but also constrained by the HL inversion approximations, moreover without introducing external information, such as simulation based constraints. Note that, in our later experiment we will apply a constraint for deriving the mass changes of high level mascons but only to perform a comparison.

4.3.3. Definition of HL mascons

In this section it is discussed how HL mascons are created. Since the LL mascons on GrIS are a subdivision of the 8 major DS we choose to always group LL mascons into 8 HL mascons. The motivation for this approach is that we already find a good consistency between different studies for both the GrIS and for 8 particular regions (Barletta, et al., 2013; Bonin and Chambers, 2013; Xu et al., 2015). In order to explore more HL definitions, we will start from the definition used in chapter 3 (figure A4.2), i.e. 8 GrIS mascons and 4 additional mascons for the surrounding glacier areas.

We impose the condition that the majority of the HL mascons must include the same number of LL mascons in order to prevent that any HL mascon becomes too big or too small. The number of LL in each HL mascon is set to d. Note that the mascons outside GrIS will always be the same, thus in the following only the HL mascons for GrIS are discussed. When d is large, the size of the HL mascon increases while the number of HL mascons decreases. We group the LL mascons clock-wise starting from mascon LL1 (see examples in figure 4.1). The total number of LL mascons is 19, which is not dividable by any chosen *d*, so this leaves one HL mascon with a different size from the others. For instance, when *d*=2, mascon LL19 cannot be paired with another LL mascons.

So we decide that if the number of the "left over" LL mascons is equal or less than half of d, then this mascon will be added to the HL mascon next to it. The indexing of HL mascons is also clock-wise starting from the one including the LL1 mascon. HL mascon definitions that can be obtained according to this procedure are illustrated in figure 4.2. Our LL mascon definitions follow from the 19 drainage basins found by (Zwally, 2012). We allow the topologic parameter d to vary between 2 and 4 so that the areas of HL mascons are similar to the mascons in the 8 DSs definition by Zwally et al. (2012).

The consequence is that we can retrieve 20 different HL mascon definitions. The number of HL mascons associated with each d is 9, 6 and 5, for d=2, 3 and 4, respectively.

In figure 4.2, a simplified case of GrIS LL mascon definition is shown in the top row. We use seven LL mascons to separate the GrIS. The first and the last mascon, i.e. mascon LL1 and mascon LL7 are assumed to be lying next to each other. We let d=2, and group the neighboring mascons starting from mascon LL1 which results in three HL mascons. The "left-over" HL mascon has only 1 LL mascon, LL7. Following the rule that is mentioned above, it is included in HL mascon 3. As a result, the new HL mascons definition (HL1) contains two mascons with size 2 and one with size 3. The corresponding linear relationship matrix $\mathbf{h}_{HL}$ is shown on the right hand side.

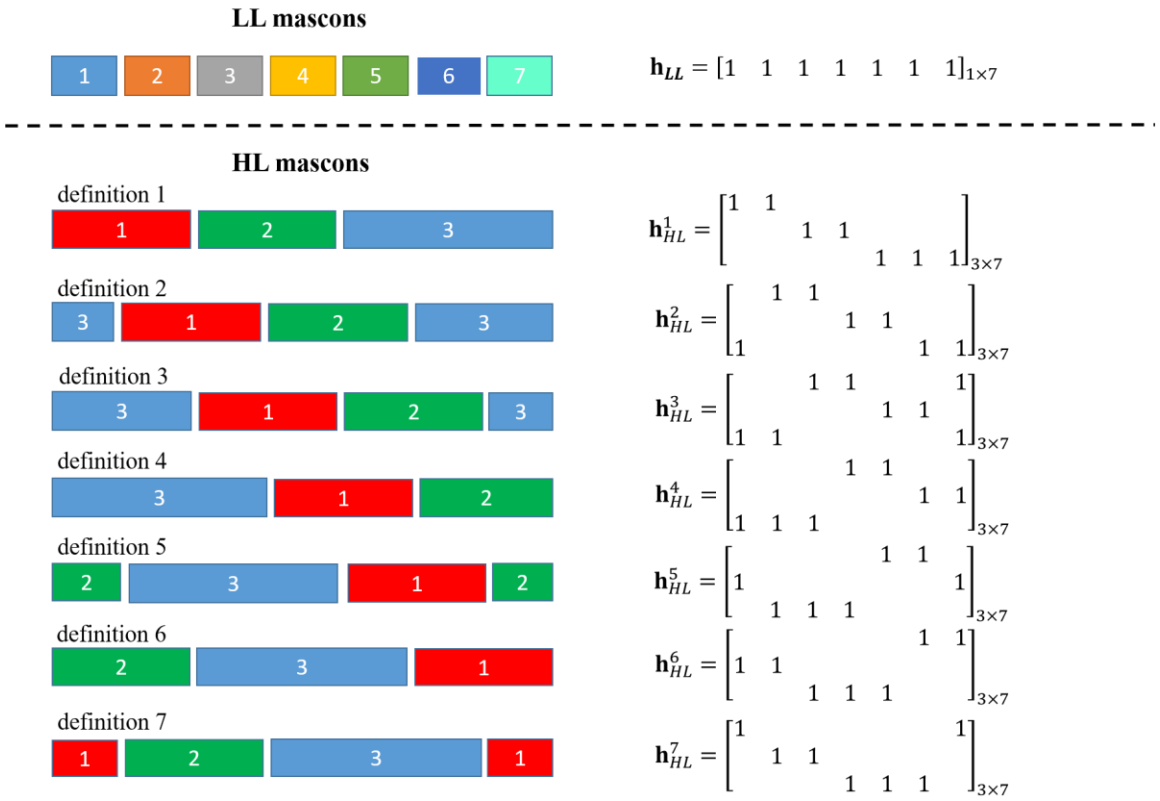

Figure 4.2: An example of separating HL mascons based on the LL mascon definitions. Seven blocks on the top layer represent the smaller LL mascons. All the possible HL mascon separations are shown below the dashed line. In each HL separation, three lager mascons are marked in blue, red and green. On the right hand side, the corresponding $\mathbf{h}_{LL}$ and $\mathbf{h}_{HL}$ matrix is listed; see also the explanation in section 4.3.1.

It also can be noticed that, if we group HL mascons starting from a new LL mascon, e.g. from mascon LL2, then one obtains a different HL mascon definition as definition 2 (third row in figure 4.2). If we move the starting LL mascon, then in total seven different HL mascon definitions are obtained for the example with 7 LL mascons. As mentioned before, three different values of d are used. Furthermore, the rank of each $\mathbf{h}_{HL}$ is determined by the number of HL mascons in each definition. Hence, the rank of the **H** matrix (in equation (4.6)) becomes 381 for the GrIS and 609 when we include the EBIS areas. Equation (4.6) can be solved and we discuss the influence using HL mascons as the constraint in section 4.5.

4.4. Grid resolution for mascons

Due to the smaller sizes of the mascons (LL mascons) used in this study, a different grid resolution on which the mascons are discretized can generate noticeable differences in mass estimates. To test this, LL mascons with three different spatial resolutions are constructed, i.e. 0.25°, 0.5° and 1°. The mascon definitions for the different grids are shown in figure A4.2 and the areas of each corresponding mascon can be found in table A4.1. The mascons on the highest resolution grid have the smallest areas compared to coarser mascons because a grid cell is considered to be part of the mascon if it is partly contained in the mascon. We apply least-squares inversion using equation (4.3), with observations **y** based on the simulated spherical harmonics as described in section A4.1. For this test, a Gaussian filter with smoothing radius $r_{1/2}$=300 km is applied to the spherical harmonics of the observations and the influence functions. We choose the regularization term σ=3 for all the mascons as determined by Bonin and Chambers (2013). Note that the simulation is only used to verify the feasibility of the hierarchical method, the required constraints that we impose do not depend on a simulation. We compare the inverted approximation of the regional mass changes to the actual mass changes resulting from the simulation, and study the differences in the linear mass change rate for each mascon. The result is shown in table 4.1 where it can be seen that the use of different mascon resolutions results in a variation of the approximation for the same mascon. When applying the mascons with the finest resolution of 0.25°, the approximation-to-simulation difference is the lowest in most of the mascons. In DS1.3, DS4.3 and DS8.1 the approximation deviates more from the simulation. When using the 0.25° resolution mascons, the approximation-to-simulation differences increase by 0.5 Gt·yr^{-1}, 0.9 Gt·yr^{-1} and 0.6 Gt·yr^{-1}, respectively, compared to the lowest one. However, when we consider the simulated mass change rates in these mascons, the variations are all less than 10%, i.e. ~8.2%, ~6.4%, ~4.3% for DS1.3, DS4.3 and DS8.1, respectively. Thus, a finer resolution is considered to be better when applying the least-squares inversion method. Therefore, in the following test we will employ a 0.25° resolution for the definition of the LL and HL mascons. The resolution does not matter for the GRACE data which has low resolution, but it could matter for following the outlines of the drainage areas.

Table 4.1: The annual trend difference of the mass change in each mascon between the approximation and the simulation. The spatial resolution of the mascon grid varies from 0.25° to 1.0°. The unit is Gt·yr^{-1}

Resolution	DS1.1	DS1.2	DS1.3	DS1.4	DS2.1	DS2.2	DS3.1	DS3.2	DS3.3	DS4.1	
0.25°	-2.8	-1.8	3.2	-5.9	5.3	-4.4	9.4	-7	5.9	-4.5	
0.5°	-3.2	-2.1	2.7	-6.2	7.5	-4.4	10.2	-7.7	7.2	-4.6	
1.0°	-3.3	-1.9	2.8	-6.4	9.5	-5.1	11.0	-7.6	7.4	-4.5	
	DS4.2	DS4.3	DS5	DS6.1	DS6.2	DS7.1	DS7.2	DS8.1	DS8.2	GrIS (sum)	GrIS (rms)
0.25°	11.5	4.7	-5.7	9.4	-26.8	31.2	-19.2	9.4	-3.3	8.6	12.0
0.5°	11.8	3.8	-7.5	9.5	-27.9	33.2	-19.6	8.8	-3.6	11.1	12.6
1.0°	12.3	5.8	-6.0	10.2	-30.3	34.2	-21.1	9.8	-3.4	14.4	13.3

4.5. Results analysis

4.5.1. Observation: simulation

In order to judge how well our hierarchical constraint method performs compared to the conventional least-squares inversion based on equation (4.2) we conduct two experiments.

Experiment 1.

To validate the claim that the constraints based on priori information are not needed we need to show that our method is stable with or without such constraints. Furthermore, in this experiment we need to find out the optimal constraint $\boldsymbol{\sigma}$ for our reference solution from equation (4.2). Therefore, we ran the hierarchical method and the standard least-squares inversion method (i.e. equation 4.2) by allowing various constraint values $\boldsymbol{\sigma}$ namely $\boldsymbol{\sigma}=1\times10^{6}$, 1×10^{3}, 10, 3, 0.1. Note that it is possible to use different constraints $\boldsymbol{\sigma}$ for different mascons as we have demonstrated in chapter 2. However, in chapter 2 the mascons are defined according to the 2000 m elevation contour, which gives an indication of using two different constraints for GrIS. In this study, the mascons are defined only according to the glacier basin layout. Some more study is required to determine how many different constraints are needed and for which mascons. Although it can be an interesting topic, it is not the main focus in this chapter. Therefore, one constraint $\boldsymbol{\sigma}$ is applied for both HL and LL mascons in the hierarchical method. Our conclusions are:

- When using a very weak constraint $\boldsymbol{\sigma}=10^{6}$, the approximation is basically un-constrained (Schrama and Wouters, 2011). Therefore, the associated solution can be considered as not using any priori information on the GrIS mass changes.
- The constraints $\boldsymbol{\sigma}=10$ and 0.1 are the optimal constraints found in chapter 2 for the coastal and interior GrIS regions, respectively. We use them here separately (one at a time) to represent the constraints for the large and very small mass changes.
- The constraint $\boldsymbol{\sigma}=3$ is the optimal constraint found by Bonin and Chambers (2013) when a single value constraint is considered.

In this experiment, we are not only interested in the mass change trend in the approximation, but also the approximated regional mass change distribution for each month is studied, since it is

possible that a good trend approximation is obtained while the mass changes time series is very different from the simulation. We apply equation (4.2) with the LL mascons using the constraint $\boldsymbol{\sigma}$=3, and denote the solution by "*LL only*". To compare with the "*LL only*" approximations, we first create several different HL mascons based on the method in section 4.3.3 and estimate regional mass changes. Then we use the hierarchical constraint method described in section 4.3.2 to obtain the "*LL+HL*" approximations. The results of this experiment are given in table A4.2 while selected results are summarized in table 4.3. As can be seen in this table, with smaller values of $\boldsymbol{\sigma}$, the absolute trend differences (per mascon) with respect to the simulation decrease from 15.1 Gt·yr^{-1} to 8.2 Gt·yr^{-1} in the "*LL only*" solutions, and also the monthly mass approximations (per mascon per month) become closer to the simulated mass changes with decreasing $\boldsymbol{\sigma}$. In contrast, the solutions using the hierarchical method are hardly sensitive to changing the constraint $\boldsymbol{\sigma}$**,** not only for the trend but also for the monthly approximation of mass changes. Moreover, in all cases the hierarchical method performs better in this table, which means it gives a better approximation for each mascon. However, one may find in table A4.2 that the trend in the approximation for the entire GrIS as well as for DS 5 of the "*LL only*" method is sometimes slightly better than "*LL+HL*" solution. For instance, when $\boldsymbol{\sigma}$=10^6, the "*LL+HL*" solution shows ~6 Gt·yr^{-1} less mass loss than the simulation, but the difference for the "*LL only*" solution is close to 0 Gt·yr^{-1}. This is likely because approximation errors in mascons are cancelled out when integrating over the entire GrIS.

From table 4.3 we conclude that using the strongest constraint $\boldsymbol{\sigma}$=0.1 results in seemingly better approximations, but if we assess the overall mass changes trend from table A4.2 for the entire GrIS, the solutions for both methods diverge more from the simulation for $\boldsymbol{\sigma}$=0.1. In that case we find overall ~66 Gt·yr^{-1} less mass loss for the "*LL only*" solution. Consequently, we choose the constraint $\boldsymbol{\sigma}$**=3** as the best constraint in this experiment for the conventional least-squares inversion, which reduces the approximation errors in each mascon to a level that will not significantly affect the consistency (~ -10 Gt·yr^{-1} difference) in the approximations for the entire GrIS.

Table 4.3: The comparison between the hierarchical method (*LL + HL*) or the normal constrained least-squares method in equation (4.2) (*LL only*). In this table, the mean absolute differences to the simulation are shown.

Constraint ($\boldsymbol{\sigma}$)	*Trend Diff.(Gt·yr^{-1})*		*Monthly Diff.(Gt)*	
	LL only	LL + HL	LL only	LL + HL
10^6	15.1	4.5	101.7	41.9
1000	14.9	4.5	99.6	41.9
10	11.3	4.4	71.9	41.9
3	9.0	4.2	58.7	40.4
0.1	8.2	4.8	46.2	37.1

The effect of using constraints for both LL only and LL + HL methods is also demonstrated in figure 4.3. In this figure, trend differences to the simulation are compared between using the constraints $\boldsymbol{\sigma}$=10^6 and $\boldsymbol{\sigma}$**=3**. These trend differences can be considered as the "accuracy" of the approximations. When we further compare the "accuracy" of two approximations, the solution

resulting from using $\boldsymbol{\sigma}$**=3** is better. Hence we consider the "accuracy" differences as the improvement in this figure. When the improvement is negative it means the regional solution becomes worse in that area. Apparently, the optimized value of $\boldsymbol{\sigma}$ is more important for reducing the monthly approximation error in all mascons for "*LL only*" solutions. Apart from a small deterioration in mascons 1.1, 3.3 and 5, the trend in mass changes approximations is improved as well. Furthermore, it can be noticed that the trend improvement in the "*LL+HL*" solutions is negligible compared to the error margins except in DS4.3 and DS5. DS5 is the only mascon that consists of an entire basin; in this mascon stronger constraints (e.g. $\boldsymbol{\sigma}$ **=0.1**) reduce the approximation error, and also for the adjacent mascon DS4.3. Nevertheless, it is safe to say that, using or not using a constraint will not significantly alter the result obtained by the hierarchical method.

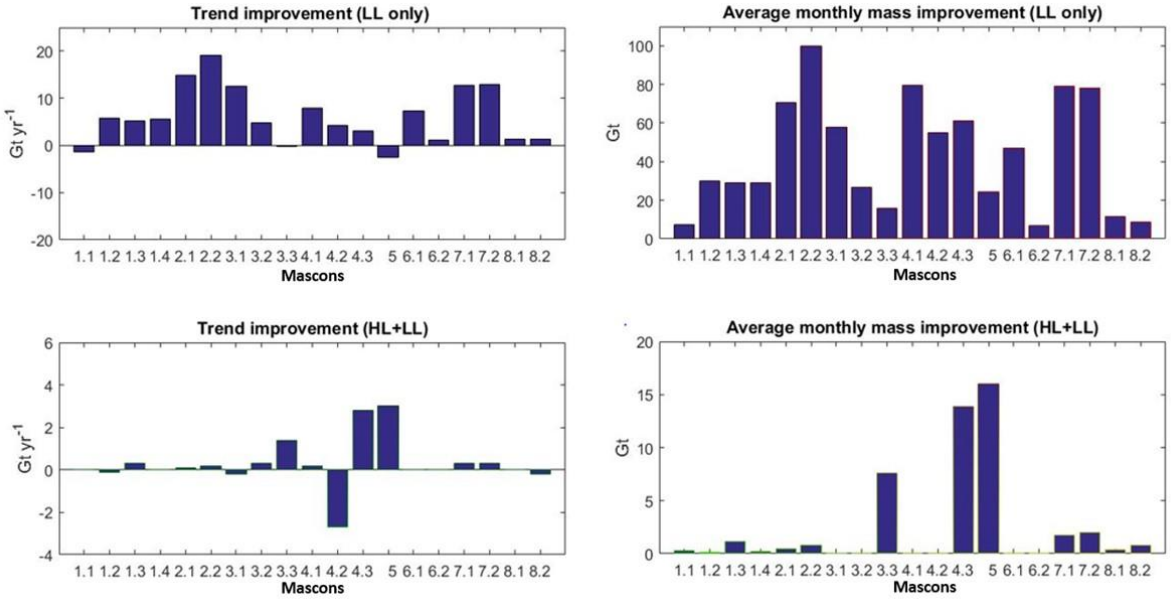

Figure 4.3: The differences to the simulation between using the constraint in the LL only and the LL+HL solution. Both the differences in the trend and in the monthly mass approximations are considered. The x-axis indicates the mascon index. The top row shows the results associated with the constraint $\boldsymbol{\sigma} = \mathbf{10^6}$, and the results of $\boldsymbol{\sigma} = 3$ are in the bottom row.

Experiment 2.

In this experiment, we show the comparison between a conventional least-squares method and the hierarchical method. As reference we consider the approximations of the "*LL only*" solution and the optimal constraint $\boldsymbol{\sigma}$=3, while the hierarchical solution is denoted as "*LL+HL"*. In this experiment no constraint is used for the hierarchical method. To compare both solutions, the regional mass change rates for each mascon as well as for the whole GrIS are shown in table 4.4. Comparing the mass change rates in each mascon with the simulation, it can be seen that the approximation-to-simulation difference is reduced in every mascon when the hierarchical constraint method is applied.

The west GrIS mascons 6.2, 7.1 and 7.2 mascons are different from each other regarding the coverage area and the regional mass change rate. These three mascons are adjacent to each other and the area of mascon 7.1 is approximately half of its neighboring mascons. At the same time, mascon 7.1 also contains a significant amount of mass loss of ~-35.3 $Gt \cdot yr^{-1}$ in the simulation, which is three times larger than in mascon 6.2 and four times larger than in mascon 7.2. The high mass loss is due to the ice discharge from the Jakobshavn glacier in mascon 7.1, which has been rapidly increasing during the simulated time period (Howat et al., 2011; van de Wal et al., 2012; Enderlin et al., 2014 and Andersen et al., 2015). This leads to a concentrated mass distribution in these areas since we treat the discharge as the point mass change at the glacier outlet grid in the simulation. As can be seen in figure A4.1 the negative point mass change will be smoothed out and spread across three mascons when the smoothing radius increases. In the "*LL only*" approximations, the approximated mass changes become proportional to the size of these three mascons which causes the regional approximations to deviate from the simulation. As can be found in table 4.3, the simulation-to-approximation differences are -27 $Gt \cdot yr^{-1}$, +31 $Gt \cdot yr^{-1}$ and -19 $Gt \cdot yr^{-1}$ for mascon 6.2, mascon 7.1 and mascon 7.2, respectively. The negative-positive-negative difference suggests that a negative correlation error exists in the approximation which could be further reduced by introducing separate constraints σ for different mascons (Section 2), or applying a correction as in Section 3.

Table 4.4: comparison of the linear annual mass change rates in 19 regions between 2000 and 2012. The unit is $Gt \cdot yr^{-1}$. The approximation based on 19 LL mascons is labelled as "LL only", while approximations also constrained by the HL mascons are indicated by "LL+ HL".

(unit $Gt \cdot yr^{-1}$)	DS1.1	DS1.2	DS1.3	DS1.4	DS2.1	DS2.2	DS3.1	DS3.2	DS3.3	DS4.1	DS4.2	DS4.3
LL only	-10.0	-6.4	-2.9	-10.8	-3.8	-5.9	3.8	-12.1	-9.9	-24.7	-21.6	-9.3
LL+HL	-7.0	-5.6	-9.0	-6.2	-8.3	1.3	1.5	-6.3	-13.5	-19.8	-27.2	-14.3
Simulation	-7.2	-4.6	-6.1	-4.9	-9.1	-1.5	-5.6	-5.1	-15.8	-20.2	-33.1	-14.0
	DS5	DS6.1	DS6.2	DS7.1	DS7.2	DS8.1	DS8.2	Elles.	Baff.	Ice.	Sval.	GrIS
LL only	-17.5	-0.7	-43.3	-4.3	-29.1	-4.5	-8.4	-25.3	-14.8	-3.9	-5.0	-221.0
LL+HL	-10.0	-11.3	-38.7	-17.9	-15.6	-9.1	-5.7	-23.9	-16.1	-4.8	-5.7	-222.7
Simulation	-11.8	-10.1	-16.5	-35.5	-9.9	-13.9	-5.1	-20.9	-16.9	-4.8	-5.3	-229.8

4.5.2. Mass changes derived from GRACE Level-2 data

We implemented CSR RL05 GRACE level 2 spherical harmonic coefficients to derive the EWH observation **y** in this section. The GRACE coefficients from January 2003 to December 2012 are obtained from the University of Texas Center for Space Research (CSR). The maximum degree and order is 96. We use the monthly degree 1 coefficients (C_{10}, C_{11} and S_{11}) estimates by Swenson et al. (2008), to represent the mass changes resulting from geocenter motion. The more accurate geopotential flattening coefficients (C_{20}) obtained from Satellite Laser Ranging (SLR) are used to replace the ones observed by GRACE (Chen et al., 2013). In the following step we average the monthly spherical harmonics between 2003 and 2012 and remove the average from the GRACE data in order to obtain the spherical harmonics of the monthly mass changes. To remove effects

other than ice melt, we remove the monthly continental water storage changes from the Global Land Data Assimilation System (GLDAS) model version 2 (Rodell et al., 2004). Note that the permafrost and glacier regions are excluded from the model output. The GIA effect is corrected for by removing a GIA model (ICE-5G based) by Paulson et al. (2007). The rest of the procedure is the same as in section 4.2 and in section 4.3.

We compare the "LL only" and "LL+HL" solution with the IOM within the same time span in figure 4.5. In this figure, we show the possible ranges of the mass change rates for a 95% confidence interval. The errors of the approximation of the GRACE data are estimated from propagating the uncertainty of the GRACE data, differences between various GIA models and the magnitude of the GLDAS model. Details of the error estimation can be found in table A4.3 and in (Xu et al., 2016). The GRACE data originates from the CSR release 5 solution that comes with maximum degree and order of 60 or 96. We assume that spherical harmonic coefficients beyond degree and order 60 do not represent any geophysical signal, and that they mostly contain noise (Bonin and Chambers, 2015).

We estimate the uncertainty of the SMB simulation as error-to-mass change ratio of ~18% (Ettema et al., 2009) and the uncertainty of the D simulation is from Enderlin et al. (2014). It can be found in figure 4.3 that the "*LL+HL*" solution agrees with the IOM in more mascons than the "*LL only*" solution. Also considering the improvement seen in section 4.5.1, it suggests that the "*LL+HL*" solution is less affected by an approximation error. For this reason the LL+HL approach is better suited for approximating the GRACE data in the LL mascons. In mascons 1.1 and 2.2 the "*LL+HL*" solution is further from the IOM than "*LL only*" solution but still within the uncertainties. We think this is due to the fact that "*LL only*" is already constrained with the priori information by σ=3, and this constraint could be the optimal constraint for these two regions. Apparently, the additional governing information introduced by *HL* mascon approximations enlarges the approximation error in these regions.

It can also be noticed that in some mascons the "*LL+HL*" solution is closer to the IOM than "*LL only*" solution but still does not agree with the simulation, i.e. in mascon 3.2, 4.2, 7.1, 7.2 and 8.1. For mascons 3.2, 7.1 and 7.2, the differences are similar to the approximation-to-simulation difference in section 4.5.1. Thus it is likely that for these mascons the differences are mainly due to approximation error. These three mascons belong to DS 3 and 7, respectively. In Xu et al. (2016) we showed that GRACE and the simulation can agree in these two areas when the "*LL only*" method is applied. Therefore, the negative correlation error appearing in mascon 3.2, 7.1 and 7.2 arises because of the separation of the DS into smaller sub-areas. Although it may not be the major reason, the uncertainty of the GRACE coefficients in these mascons can be underestimated as explained before, and causing a smaller range of the possible mass change rates in the approximations. Regarding mascon 4.2, we have shown a noticeable negative correlation error appearing in DS 4 (Xu et al., 2016) which explains the difference between GRACE approximations and the simulation in sub-DS mascon 4.2. The difference between "*LL+HL*" solution and the simulation is smaller than for the "*LL only*" solution. Regarding mascon 8.1, our conclusion is that the difference is not due to GRACE regional mass changes being poorly approximated, but because

of the underestimated uncertainty in the IOM, see Sasgen et al., (2012) and Xu et al., (2016).

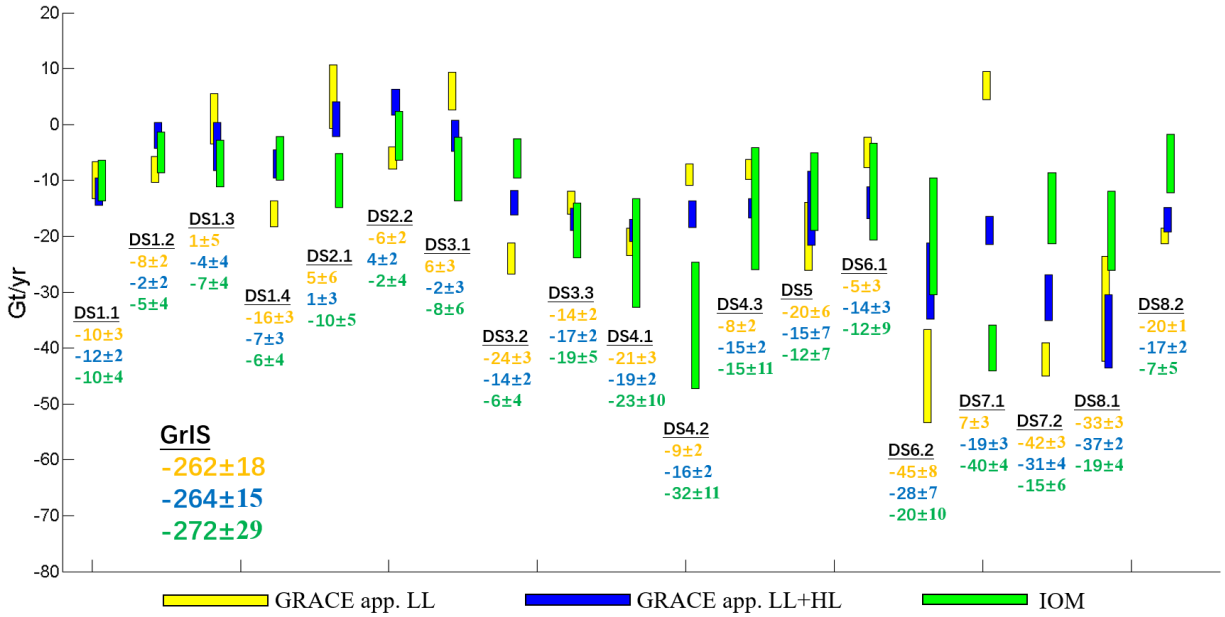

Figure 4.5: Comparison between the annual mass change rate approximations derived from GRACE data with the IOM in LL mascons. The approximations are derived from using the "LL only" solution (yellow) and the "LL+HL" solution (blue). The solution from the IOM is shown in green. The time interval is between Jan 2003 and Dec 2012. Note that the mass loss rates for the IOM differ from what is presented in table 3.1 because here a 0.25 degree cell resolution is used whereas 1 degree was used in table 3.1.

4.6. Conclusion and recommendations

In this study, we show that our hierarchical constraint method is capable of reducing errors in mass changes estimates in small GrIS regions. It can be a feasible method for constraining the GRACE regional solution to prevent having to rely on priori information, which might be biased or erroneous. We compared our results with a least-squares solution constrained only by a single prior variance. The simulation as well as the real GRACE data implementation show that our new method is able to better constrain the approximation for 19 GrIS mascons. The separation of 19 mascons approaches a resolution limit of GRACE data on the GrIS. We demonstrated that a finer separation of mascons results in an increased approximation error.

We suggest that the hierarchical constraining method can be implemented in other areas for obtaining mass changes estimates in small regions from GRACE data. The hierarchical constraint method can be further improved by employing a weighted least-squares method. Because the same HL mascon can be found in different HL mascon definitions different estimates will be obtained for the same HL mascons. This creates the possibility of estimating the variance of the inversion for this HL mascon, which could be employed as the weights for the associated approximations.

Appendix A

A4.1. Spherical harmonics simulation

In this study, we establish a 10-year simulation of the GrIS and surrounding areas, in order to be able to compare the inverse regional mass changes approximation with the pre-defined "truth". For this study we employ the surface mass balance estimated by the Regional Atmospheric Climate Model version 2.3 (RACMO2.3) and the ice discharge estimates of Enderlin et al. (2014). The RACMO2.3 model is developed and maintained at the Institute for Marine and Atmospheric Research (IMAU), Utrecht University, the Netherlands. The details of RACMO2.3 model can be found in Noël et al. (2015). The ice discharge is derived from the estimates of the ice thickness change and the velocity of the ice flux. Ice thickness changes are obtained from NASA's Operation IceBridge airborne ice-penetrating radar data. Ice surface velocity is obtained from tracking the movement of surface features that are visible in repeat 17 Landsat-7 Enhanced Thematic Mapper Plus and Advanced Spaceborne Thermal and Reflectance 18 Radiometer (ASTER) images (Enderlin et al., 2014).

We distribute the monthly RACMO2.3 SMB estimates onto a global spherical grid at 0.25^{o} spatial resolution. We also consider the ice discharge as point mass changes located on grid cells located along the edge of GrIS where the corresponding glacier outlets are located. It has to be mentioned that the discharge is given on an annual basis. Hence, in order to integrate with the monthly based SMB estimates, we assume no temporal variation in discharge and interpolate the annual change to the monthly change using the same baseline of the RACMO2.3 months, i.e. Jan 2000 to Dec 2012. For the nearby glacier regions outside Greenland we consider Ellesmere Island, Baffin Island, Iceland and Svalbard. Furthermore, only the SMB estimates from RACMO2.3 are used. We note that ice discharge is relatively small compared to the regional SMB changes, for details see Xu et al. (2016).

In order to include other glacier regions, we use the estimates of the mass changes from Jacob et al., (2012). To estimate the remaining land mass changes, we apply the GRACE level-2 monthly land mass grids, the "*GRACE Tellus*" version RL05.DSTvSCS1409. These data are available from *http://grace.jpl.nasa.gov.* Details can be found in Swenson (2012), Landerer and Swenson (2012) and Swenson and Wahr (2006). All GRACE data are projected on the same global grid as was used for RACMO2.3 SMB and the ice discharge data for the GrIS.

Next, we convert the global mass distribution grids over the entire Earth surface to spherical harmonics coefficients up to maximum degree and order 96. Furthermore, to better simulate the monthly GRACE level-2 coefficients, one also has to consider noise in the GRACE data which manifests itself as the well-known GRACE "stripes" in the north-to-south direction (e.g. Swenson and Wahr 2006).

We first separate the noise from the actual mass changes signals from the GRACE data over land areas. In this study, we use the aforementioned spherical harmonics of the simulation to represent the spherical harmonics of the actual mass changes on the Earth's surface. After removing simulated mass change signals from GRACE data at the same month, we also remove a linear trend

from the remaining GRACE data in order to minimize the influences of the uncertainties in the RACMO2.3 SMB, the ice discharge as well as all other mass change estimate uncertainties in the simulation. What remains is considered to be noise-only spherical harmonics. It has been demonstrated by Bonin and Chambers, (2012, 2015) that one can simulate the monthly GRACE stripes using the "noise-only" GRACE spherical harmonics. For the GRACE noise model, we employ the Jan 2003 to Dec 2012 monthly spherical harmonics of GRACE and a simulation of the global mass changes within the same time span to extract the pattern of GRACE noise. This model is used for the full-time span of the simulation, i.e. Jan 2000 to Dec 2012. In the end, we combine the simulated GRACE noise and simulated mass changes in the spectral domain which yields the spherical harmonics of the simulation used for this study. The scattered mass distribution for the GrIS and neighboring glacier regions and the corresponding EWH maps can be seen in figure A4.1.

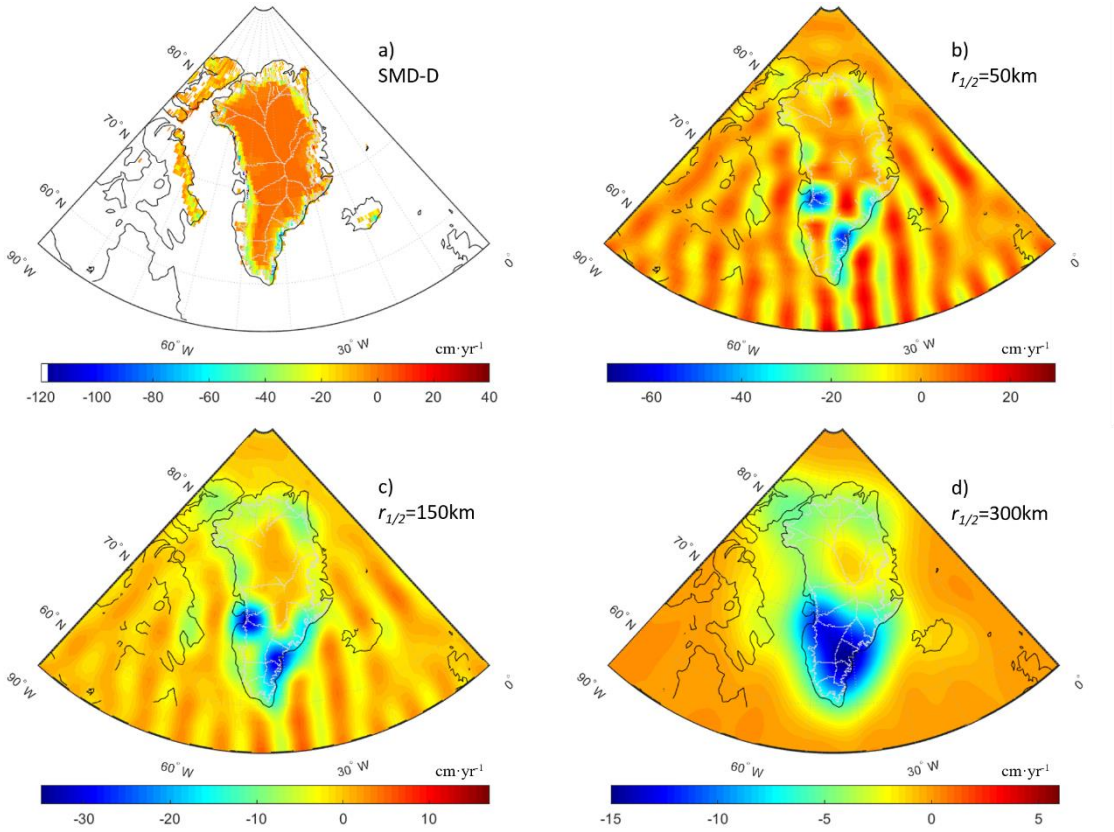

Figure A4.1: The annual mass change rate of simulation with unit equivalent water level height in cm·yr^{-1}. The simulated time interval is 2000–2012. a) The scattered mass distribution derived from the estimates of the surface mass balance. b) to d) The EWH maps obtained when we use the associated spherical harmonics up to the maximum degree and order l=96 and the Gaussian filter using different smoothing radii ranging from $r_{1/2}$=0 km to $r_{1/2}$=300 km. The GRACE noise is simulated using the CSR GRACE level-2 coefficients from Jan 2000 to Dec 2012. Note the color scales are different

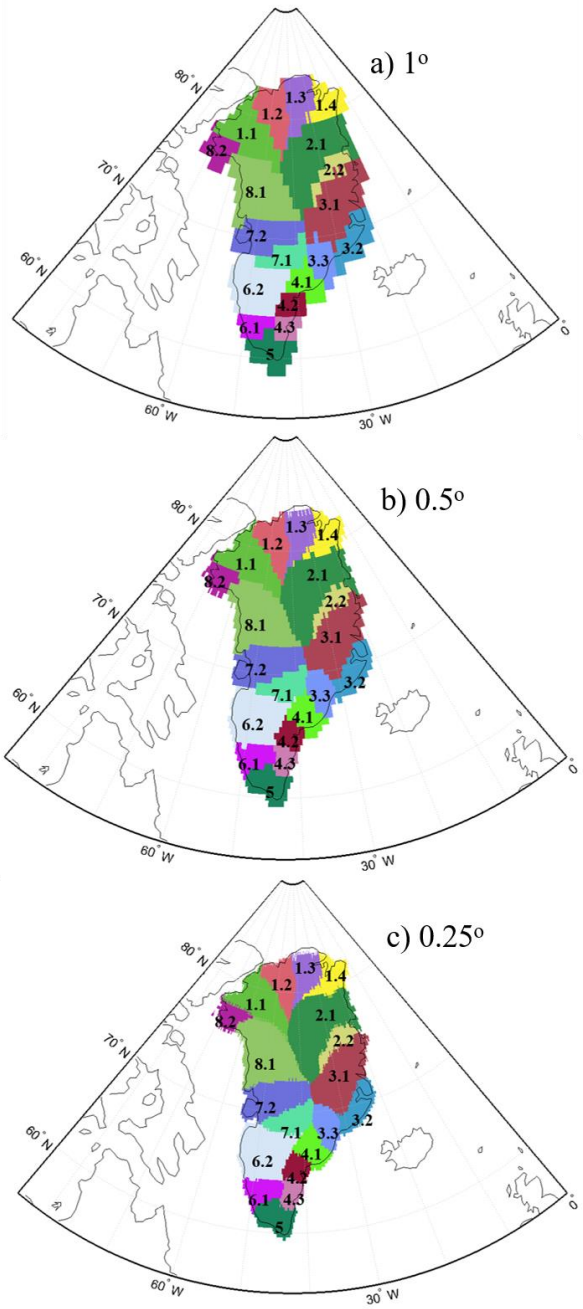

Figure A4.2: Mascon definitions for GrIS. Our mascons follow the DS and sub-DS separation by Zwally et al. (2011). Each mascon is created based on a global grid with resolution of 1°, 0.5°, and 0.25°.

Table A4.1: Comparison of the areas for each mascon based on the global grid using different spatial resolution., The unit is 10^5 km^2.

	Area (10^5 km^2)									
	DS1.1	DS1.2	DS1.3	DS1.4	DS2.1	DS2.2	DS3.1	DS3.2	DS3.3	DS4.1
Resolution	DS1.1	DS1.2	DS1.3	DS1.4	DS2.1	DS2.2	DS3.1	DS3.2	DS3.3	DS4.1
1º	1.93	1.30	1.18	0.89	3.19	0.61	2.75	1.29	0.91	0.88
0.5º	1.76	1.12	1.01	0.92	3.10	0.58	2.49	1.10	0.83	0.85
0.25º	1.63	1.02	0.92	0.85	3.06	0.60	2.36	0.98	0.81	0.83
	DS4.2	DS4.3	DS5	DS6.1	DS6.2	DS7.1	DS7.2	DS8.1	DS8.2	GrIS
1º	0.58	0.50	1.26	0.61	2.33	0.93	1.72	2.94	0.82	25.8
0.5º	0.55	0.47	1.01	0.75	2.20	0.92	1.84	2.77	0.65	24.3
0.25º	0.54	0.47	0.95	0.73	2.18	0.94	1.80	2.70	0.59	23.4

Table A4.2: The mass changes approximation of the simulation using different constraining methods. The hierarchical constraint method is denoted by "HL+LL", and "LL only" refers to the results from the normal constrained least-squares method. Each comparison invokes the same least-squares constraint σ^2. We list the approximated annual trend from 2003 to 2012 in 19 GrIS sub-regions and the difference between the approximated trend with the simulation ("Trend Diff."). In addition, the table includes the average of monthly differences between approximation and simulation (Month Diff.) in order to show the "oscillation" of the monthly mass approximation.

DS	$\sigma = 10\text{^}6$						$\sigma = 10\text{^}3$					
	Trend (Gt·yr^{-1})		**Trend Diff.** (Gt·yr^{-1})		**Monthly Diff.** (Gt per month)		**Trend** (Gt·yr^{-1})		**Trend Diff.** (Gt·yr^{-1})		**Monthly Diff.** (Gt per month)	
	LL only	HL+LL	LL only	HL+LL	LL only	HL+LL	LL only	HL+LL	LL only	HL+LL	LL only	HL+LL
1.1	-8.6	-7.0	1.4	-0.2	28.1	15.2	-8.6	-7.0	1.4	-0.2	28.0	15.2
1.2	-12.1	-5.5	7.5	0.9	47.1	13.3	-12.1	-5.5	7.5	0.9	46.7	13.3
1.3	2.3	-9.3	-8.4	3.2	58.3	24.2	2.3	-9.3	-8.4	3.2	58.0	24.2
1.4	-16.3	-6.2	11.4	1.3	63.1	13.7	-16.2	-6.2	11.3	1.3	62.9	13.7
2.1	11.1	-8.2	-20.2	-0.9	111.5	26.0	11.0	-8.2	-20.1	-0.9	110.6	26.0
2.2	-25.1	1.5	23.6	-3.0	124.6	23.6	-24.9	1.5	23.4	-3.0	123.6	23.6
3.1	16.3	1.3	-21.9	-6.9	109.4	41.3	16.2	1.3	-21.8	-6.9	108.8	41.3
3.2	-16.9	-6.6	11.8	1.5	57.4	15.8	-16.8	-6.6	11.7	1.5	56.9	15.8
3.3	-10.1	-12.1	-5.7	-3.7	65.1	50.0	-10.3	-12.1	-5.5	-3.7	62.2	49.9
4.1	-32.7	-19.6	12.5	-0.6	143.1	44.0	-32.0	-19.6	11.8	-0.6	134.3	44.1
4.2	-17.4	-29.9	-15.7	-3.2	158.4	56.6	-18.5	-29.9	-14.6	-3.2	146.2	56.7
4.3	-21.8	-17.1	7.8	3.1	83.9	24.3	-20.9	-17.1	6.9	3.1	74.9	24.2
5	-14.9	-7.0	3.1	-4.8	50.1	71.5	-15.2	-7.1	3.4	-4.7	48.2	71.4
6.1	6.6	-11.3	-16.7	1.2	88.6	30.1	6.6	-11.3	-16.7	1.2	88.5	30.1
6.2	-44.4	-38.7	27.9	22.2	160.4	129.2	-44.2	-38.7	27.7	22.2	159.3	129.2
7.1	8.4	-17.6	-43.9	-17.9	254.9	93.3	8.3	-17.6	-43.8	-17.9	254.5	93.3
7.2	-42.0	-15.9	32.1	6.0	224.0	52.5	-42.0	-15.9	32.1	6.0	224.0	52.5
8.1	-3.2	-9.1	-10.7	-4.8	80.1	51.6	-3.1	-9.1	-10.8	-4.8	80.3	51.6
8.2	-9.8	-5.5	4.7	0.4	24.1	20.4	-9.8	-5.5	4.7	0.4	24.0	20.4
GRIS	-230.6	-223.8	0.6	-6.2	1932.2	796.6	-230	-223.9	0.2	-6.1	1891. 9	796. 5

DS	$\sigma = 10$						$\sigma = 3$					
	Trend (Gt·yr^{-1})		**Trend Diff.** (Gt·yr^{-1})		**Monthly Diff.** (Gt per month)		**Trend** (Gt·yr^{-1})		**Trend Diff.** (Gt·yr^{-1})		**Monthly Diff.** (Gt per month)	
	LL only	HL+LL	LL only	HL+LL	LL only	HL+LL	LL only	HL+LL	LL only	HL+LL	LL only	HL+LL
1.1	-9.5	-7.0	2.3	-0.2	23.1	15.1	-10.0	-7.0	2.8	-0.2	20.7	14.9
1.2	-8.8	-5.6	4.2	1.0	27.9	13.2	-6.4	-5.6	1.8	1.0	17.1	13.2
1.3	-0.5	-9.2	-5.6	3.1	41.6	23.9	-2.9	-9.0	-3.2	2.9	29.2	23.1
1.4	-13.2	-6.2	8.3	1.3	47.1	13.6	-10.8	-6.2	5.9	1.3	34.1	13.5
2.1	1.3	-8.3	-10.4	-0.8	62.7	25.9	-3.8	-8.3	-5.3	-0.8	40.9	25.5
2.2	-12.6	1.4	11.1	-2.9	59.6	23.2	-5.9	1.3	4.4	-2.8	24.9	22.8
3.1	8.3	1.4	-13.9	-7.0	71.5	41.6	3.8	1.5	-9.4	-7.1	51.4	41.7
3.2	-14.2	-6.4	9.1	1.3	42.1	15.8	-12.1	-6.3	7.0	1.2	30.8	16.0

3.3	-9.4	-12.6	-6.4	-3.2	54.8	47.0	-9.9	-13.5	-5.9	-2.3	49.4	42.4
4.1	-28.1	-19.8	7.9	-0.4	84.4	45.0	-24.7	-19.8	4.5	-0.4	63.6	44.5
4.2	-23.8	-28.9	-9.3	-4.2	90.2	62.5	-21.6	-27.2	-11.5	-5.9	103.4	72.0
4.3	-12.2	-16.0	-1.8	2.0	12.6	18.5	-9.3	-14.3	-4.7	0.3	22.9	10.4
5	-17.3	-8.2	5.5	-3.6	31.8	65.1	-17.5	-10.0	5.7	-1.8	25.7	55.5
6.1	2.4	-11.3	-12.5	1.2	61.2	30.2	-0.7	-11.3	-9.4	1.2	41.7	30.1
6.2	-42.4	-38.7	25.9	22.2	147.7	129.2	-43.3	-38.7	26.8	22.2	153.4	129.7
7.1	2.7	-17.7	-38.2	-17.8	216.7	92.7	-4.3	-17.9	-31.2	-17.6	175.9	91.6
7.2	-36.9	-15.8	27.0	5.9	191.7	51.7	-29.1	-15.6	19.2	5.7	146.1	50.5
8.1	-2.8	-9.1	-11.1	-4.8	79.0	51.5	-4.5	-9.1	-9.4	-4.8	68.3	51.2
8.2	-9.3	-5.6	4.2	0.5	19.5	20.1	-8.4	-5.7	3.3	0.6	15.4	19.5
GRIS	-226.3	-223.6	−3.7	-6.2	1365.2	785.8	-221.4	-222.7	-8.6	-7.3	1114.9	768.1

DS	$\sigma = 0.1$					
	Trend (Gt·yr^{-1})		**Trend Diff. (Gt·yr^{-1})**		**Monthly Diff.** (Gt per month)	
	LL only	HL+LL	LL only	LL only	HL+LL	LL only
1.1	-8.0	-6.4	0.8	-0.8	11.7	14.1
1.2	-4.9	-6.1	0.3	1.5	9.7	11.4
1.3	-4.3	-6.8	-1.8	0.7	16.1	13.1
1.4	-3.7	-5.1	-1.2	0.2	8.9	11.1
2.1	-8.5	-5.8	-0.6	-3.3	24.9	25.8
2.2	-0.3	-0.9	-1.2	-0.6	6.8	13.2
3.1	-5.1	-2.0	-0.5	-3.6	21.1	23.2
3.2	-6.5	-6.8	1.4	1.7	11.6	11.7
3.3	-3.4	-12.6	-12.4	-3.2	64.7	47.8
4.1	-6.0	-11.3	-14.2	-8.9	25.3	11.7
4.2	-8.9	-17.1	-24.2	-16.0	155.6	132.4
4.3	-1.6	-5.5	-12.4	-8.5	62.7	45.4
5	-10.1	-11.7	-1.7	-0.1	58.4	47.1
6.1	-2.3	-9.3	-7.8	-0.8	33.9	19.2
6.2	-41.4	-30.8	24.9	14.3	116.6	87.7
7.1	-5.6	-17.6	-29.9	-17.9	146.3	92.6
7.2	-26.7	-14.6	16.8	4.7	56.0	47.3
8.1	-11.0	-10.8	-2.9	-3.1	29.1	34.4
8.2	-5.6	-6.4	0.5	1.3	18.4	16.4
GRIS	-163.9	-187.6	-66.1	-42.4	877.8	705.6

Table A4.3: The uncertainty estimates for each LL mascon (unit: Gt).

	GRACE uncer.		*GIA uncer.*		*Overall uncer.*	
	LL only	LL+HL	LL only	LL+HL	LL only	LL+HL
DS1.1	3.7	3.7	2.7	1.5	4.5	4.0
DS1.2	2.6	3.4	1.9	1.6	3.2	3.7
DS1.3	2.4	3.6	4.3	3.9	5.0	5.3
DS1.4	2.5	3.6	1.9	1.7	3.1	4.0
DS2.1	5.8	4.3	4.9	2.2	7.6	4.8
DS2.2	2.5	4.4	1.5	0.7	2.9	4.4
DS3.1	5.1	4.0	2.3	1.9	5.6	4.5
DS3.2	3.2	3.0	2.3	1.6	3.9	3.4
DS3.3	3.1	2.5	1.3	1.6	3.4	3.0
DS4.1	3.3	2.2	1.9	1.7	3.8	2.8
DS4.2	2.7	2.1	1.3	2.2	3.0	3.1
DS4.3	2.6	2.1	1.2	1.3	2.9	2.5
DS5	3.5	2.3	5.8	6.5	6.8	6.9
DS6.1	3.7	2.7	1.9	2.6	4.1	3.7
DS6.2	5.6	3.7	7.8	6.5	9.6	7.4
DS7.1	3.6	4.3	1.8	1.2	4.0	4.5
DS7.2	5.0	4.6	1.7	3.4	5.3	5.7
DS8.1	5.5	4.4	9.0	6.2	10.5	7.6
DS8.2	2.0	4.0	1.0	0.9	2.2	4.1
GrIS	16.5	15.3	16.3	13.8	23.1	20.6
Elles.	2.2	1.0	4.1	3.7	4.7	3.9
Baff.	2.9	2.8	11.0	10.7	11.4	11.0
Ice.	0.5	1.1	0.9	0.9	1.1	1.4
Sval.	1.0	0.6	2.4	2.4	2.6	2.5

Chapter 5

Conclusions and recommendations

The variations of the Greenland Ice Sheet (GrIS) mass at basin and sub-basin scale are studied in this dissertation. Our focus is to estimate these regional mass changes using the GRACE gravity measurements which allow to gain insight in the processes that cause mass gain and loss on GrIS. An alternative method is the Input-output Method (IOM) which uses climate models and discharge measurements. With the availability of advanced surface mass balance models (e.g. RACMO2) and ice discharge surveys fully covering the GrIS, the resulting IOM solution becomes an important source of information for the mass changes of GrIS. In this study, we have demonstrated that the regional mass changes of GrIS from GRACE level 2 data can be improved with the help of the IOM solution. Moreover, we reconcile the regional mass changes between GRACE and IOM solutions. We do this not by "condensing" the different estimates within a same time period but instead, we identify the causes of regional estimates differences between these methods and find that the results can be very similar to each other given realistic error estimates.

In chapters 2, 3 and 4 we address the presence of approximation errors in the GRACE mascon solutions. In chapter 2 and chapter 3 we also investigate optimized constraints to provide more accurate estimates of the regional mass changes in eight main basins of the GrIS each separated in an interior and coastal area. In chapter 3 we investigate the uncertainties that are part of the IOM method which are related in part to the historic reference discharge. In chapter 4, we describe a hierarchical constraint method which uses the high level mascons to constrain the enclosed sub-level mascons. In all cases we respect the drainage systems laid out in Zwally et al. (2012). Section 5.1 answers the research questions defined in section 1.4 and in section 5.2 recommendations for future research are provided.

5.1. Conclusions

Research question 1: How can the variance information derived from an IOM solution help to get better constraints for the mascon inversion procedure?

Firstly, as we have shown in chapter 2, it is possible to derive variance information from the IOM method to improve the definition of the constraints. By using the variance information, we show that the optimized constraints for different GrIS regions can be determined which help to reduce the approximation error.

In chapter 2 we employ a model based simulation similar to the one used by Bonin and Chambers (2013) to determine optimal values for multiple constraints. As objective function to be minimized we propose the inter-region correlation of the mass changes in addition to the misfit of the forward modeled gravity of the GRACE data. This multi-objective optimization problem is

solved using a Non-dominated Sorting Genetic Algorithm (NSGA-II). This algorithm allows us to find the optimal combination of the regional constraints for both objectives. Tests with the optimal constraints in the simulation indicate a reduction of the approximation errors in some mascons, particularly in the interior regions of the GrIS where mass changes are smaller. At the same time the coastal regions are also properly constrained by the optimal constraint for those regions.

Research question 2: How large are the differences between the GRACE mascon inversion results and the IOM results and how can they be explained?

We study this question in chapter 3. In summary: we compare two methods and find that these two methods result in different mass changes estimates in northwest and southeast GrIS regions. We cannot reconcile these differences since they are larger than the estimated uncertainties. We demonstrate that the southeastern differences are mainly due to the approximation errors in GRACE solution, and error in the IOM solution which is larger than previously assumed in the northwest GrIS is responsible for the differences in that region.

To be more specific, a direct comparison was made between our method and the IOM solution. It is found that there are inconsistent mass change rates in several GrIS regions. In order to explain the differences, we firstly revisit our GRACE method which is demonstrated in chapter 2. We find that when using this method on a simulation, the approximations cannot agree with the simulation within the uncertainties in particular in the south-eastern GrIS regions. We calculate the approximation-to-simulation ratio based on this simulation, then multiple this ratio to our GRACE solution to adjust the GRACE solution accordingly. The improved GRACE solution in the south-east shows better consistency with the IOM solution.

We further discuss the possible causes that could underlie the differences and find that there are persistent approximation errors in southeastern GrIS areas. We trace this problem to the uncertainty of the reference SMB and the reference discharge. In the IOM method, not including the reference SMB and discharge may lead to a larger uncertainty in the IOM solution due to the cumulated modelling errors, but including them also introduces a source of uncertainty. In van den Broeke et al. (2009) and Shepherd et al. (2012), the IOM is proven to be consistent with the GRACE observation, whereas in our study, we find that, when subtracting the differences between GRACE and IOM results approximately ±10% additional uncertainty remains in the IOM solution in the northwest GrIS.

In order to better identify this 10% mismatch, in section 3.4.1, we quantify the uncertainty of the reference SMB with the RACMO2.3 model during the reference period (from Jan 1960 to Dec 1990). The uncertainty of the reference discharge is difficult to determine since there is insufficient historical discharge data of the GrIS discharge during the reference period. Therefore, we consider the modelled reference run-off in the SMB model as an alternative parameter to estimate in the least-squares adjustment. This is supported by a correlation test between the modelled run-off and discharge estimates between 2000 and 2012. In section 3.4.3, we show that by replacing the reference discharge with the modelled run-off based reference discharge the existing regional differences between GRACE and IOM solution are reduced. Nevertheless, in section 3.4.1, the difference between the mass change rates of the two techniques in the northern GrIS is not reduced.

Therefore, we further validate both improved solutions by comparing them to the ICESat-based regional mass change rates. The inter-comparison with the ICESat solution indicates a better agreement with our GRACE solution than with the regional IOM solution, thus we conclude in chapter 3 that the difference between GRACE and IOM in northern GrIS is due to the underestimated uncertainty in reference discharge and the SMB model.

Research question 3: How can we impose an alternative constraint on the GRACE mascon inversion procedure with less dependence on simulated mass changes?

To answer this research question we set-up a hierarchical constraint method based on the observation that GRACE derived mass changes solutions for larger mascons are more stable and more accurate than the solutions for small mascons. A property of the hierarchical constraint method is that smaller mascons are grouped within larger ones and that the sum of the enclosed mascons is linked to the mass changes of the larger mascon. The results show that the hierarchical constraint method is capable of reducing the approximation errors in several GrIS regions with only need for weak a priori constraints which do not have a large effect on the results. By using GRACE data, we show that the mass change estimates from the hierarchical constraint method are consistent in 12 out of 19 regions when comparing to the independent mass changes estimates from the IOM in the same mascon areas. Meanwhile, the normal least-squares inversion approach with an optimized constraint leads to the regional mass changes estimates which are consistent in 10 out of 19 regions with the IOM solution.

Research question 4: How do our GRACE mascon inversion results compare to other published results?

In this thesis we derive several versions of the GrIS regional mass changes approximations which differ from each other because of the definition of GrIS basins as well as the observation time window, and the method by which we constrain the procedures. We compare our findings to other published solutions.

In chapter 2, the implementation of three localized constraints results in regional mass change estimates which are in good agreement to some other regional GrIS studies in the large GrIS basins which involve both the areas below and above 2000 m. When we assess our approximation relative to the 2000 m contour, we find that the results of the GRACE solution are in closer agreement with independent SMB studies than previous studies, (Schrama et al.,2011) and (Bonin and Chambers, 2013). Note that the latest GRACE data are available until October 2017, However, in this study, we consider the time period from 2003 to 2012 because we compare what we retrieve from GRACE solution with the IOM solution. In the IOM solution we use the time series of the RACMO2 SMB output from 2000 to 2012, while the ice discharge estimates up to 2012 are from Enderlin et al. (2014). Therefore, in chapter 2.5 we provide only the mass changes estimates from 2003 to 2012. For the time period after 2012, it is recently suggested by Schrama (personal communication) that the mass changes for the whole GrIS increased by ~23% when including the available observations in 2015 and 2016, i.e. from -222±5.3 Gt·yr-1 (2003–2010) to -273.4±5.3 Gt·yr^{-1} (2002–2016).

In chapter 3, we compute the GRACE and IOM solutions of the mass changes between 2003

and 2013 with the same mascon definition based on the GrIS catchment layout from Zwally et al. (2012). We implement the correction to the approximation errors in the GRACE data. In section 3.4.3 we find for the whole GrIS 208±18 Gt·yr^{-1} between 2003 to 2008 from the GRACE solution, while the IOM solution shows a mass loss rate of 195±25 Gt·yr^{-1}. These loss rates increase by ~67% and ~85% in 2009–2013 in the GRACE and IOM solutions, respectively. The 10-year acceleration in the GRACE data is -25±8 Gt yr^{-2}, consistent with the IOM solution, which is -26±12 Gt yr^{-2}.

In section 4.5, we show for the whole GrIS -264±15 Gt·yr^{-1} mass changes from 2003–2012. For IOM, the value is -272±29 Gt·yr^{-1}. Two types of regional mass changes estimates differ in the small regions located on the southeastern, western and northwestern GrIS. These small regions belong to the basin 4, basin 6, basin 7 and basin 8 of the eight basins' definition of the GrIS. As we discover in chapter 3, these differences are due to the approximation error in GRACE solutions and the underestimated uncertainty in IOM.

5.2. Recommendations

In this dissertation we developed methods to improve the regional mass change estimates on Greenland derived from the GRACE data. We proposed two different constraints, namely for mascons above the 2000 m contour and those below, as well as a third constraint for the EBIS area. We noticed that within the ablation area mass changes can be different for different glaciers. An example is the mass change in the southern and southwestern coastal areas which are higher than the areas in the north. This observation suggests that one could investigate refined basin dependent constraints to be able to further reduce the approximation error.

In this thesis we have used IOM results and we compared them to the GRACE data. The IOM solution will likely improve because new measurement data become available. A recent survey of the ice thickness along the flux gate of the GrIS glaciers provides information that can be used to establish more accurate ice discharge estimates (Andersen et al., 2015). In that case, the IOM solution may no longer need to consider the reference SMB and ice discharge so that at least one recognized source of the uncertainty (in the IOM solution) can be avoided. We have also seen that the current RACMO2.3 SMB approach underestimates uncertainties in some GrIS areas. Future studies could benefit from an improved uncertainty estimate accompanying the SMB model and a better description of the assumption of a reference discharge in the northwestern GrIS.

We suggest that our methods for determining optimal constraints and the hierarchical constraint method may also be used in other areas where large mass change rates occur, such as Antarctica. The hierarchical method in chapter 4 has shown that smaller areas can be constrained by estimates for larger mascons. In this way we can increase the resolution of mass changes estimates.

The GRACE mission has come to an end in October 2017 after being in orbit for 15 years; the mission has provided unique data that have significantly changed our knowledge of mass loss and the effects of climate change in the polar areas; but also provided indispensable insight in relaxation processes as a result of changes within the lithosphere and mantle due to glacial isostatic rebound. Longer time series are indispensable for identifying long-term trends, and we look forward to data from the GRACE follow-on mission.

References

Andersen, M. L., Andersen, S. B., Stenseng, L., Skourup, H., Colgan W., Kristensen, S., Boncori, J., Ahlstrøm, A., Fettweis, X., and Forsberg, R. 2014. Mass loss from an ice-sheet drainage basin in West Greenland, Geol Surv Den Greenl, 86-90, ISBN: 9788778713834

Andersen, M., Stenseng, L., Skourup, H., Colgan, W., Khan, S., Kristensen, S., Andersen, S., Box, J., Ahlstrøm, A., & Fettweis, X., 2015 Basin-scale partitioning of Greenland ice sheet mass balance components (2007–2011), Earth Planet. Sci. Lett, 409, 89-95, DOI: doi:10.1016/j.epsl.2014.10.015.

Bales, R. C., Guo, Q., Shen, D., McConnell, J. R., Du, G., Burkhart, J. F., Spikes, V. B., Hanna, E., and Cappelen, J. 2009. Annual accumulation for Greenland updated using ice core data developed during 2000–2006 and analysis of daily coastal meteorological data, J Geophys Res-Atmos (1984–2012), 114.

Bamber, J., van den Broeke, M., Ettema, J., Lenaerts, J., and Rignot, E. 2012. Recent large increases in freshwater fluxes from Greenland into the North Atlantic, Geophys Res Lett, 39, L19501, DOI: 10.1029/2012GL052552.

Barletta, V. R., Sørensen, L. S., & Forsberg, R., 2013. Scatter of mass changes estimates at basin scale for Greenland and Antarctica, The Cryosphere, 7, 1411-1432, DOI:10.5194/tc-7-1411-2013.

Baur O., Sneeuw N., 2011 Assessing Greenland ice mass loss by means of point-mass modeling: a viable methodology. J. Geod. 85(9): 607–615, doi:10.1007/s00190-011-0463-1

Bell, R. E., Tinto, K., Das, I., Wolovick, M., Chu, W., Creyts, T. T., Frearson, N., Abdi, A., and Paden, J. D. 2014. Deformation, warming and softening of Greenland ice by refreezing meltwater, Nature Geoscience, 7(7), 497-502.

Bolch, T., Sandberg, S. L., Simonsen, S.B., Mölg, N., Machguth, H., P. Rastner, P., and Paul, F. 2013. Mass loss of Greenland's glaciers and ice caps 2003–2008 revealed from ICESat data, Geophys. Res. Lett., 40, 875–881, doi:10.1002/grl.50270.

Bonin, J. and Chambers, D. 2013. Uncertainty estimates of a GRACE inversion modelling technique over Greenland using a simulation, Geophys J Int, 194, 212-229.

Bonin, J. and Chambers, D. 2015. Quantifying the resolution level where the GRACE satellites can separate Greenland's glacial mass balance from surface mass balance, The Cryosphere, 9, 1761-1772, doi:10.5194/tc-9-1761-2015.

Box, J., and Colgan, W. 2013. Greenland Ice Sheet Mass Balance Reconstruction. Part III: Marine Ice Loss and Total Mass Balance (1840–2010). J. Climate, 26, 6990–7002, doi: http://dx.doi.org/10.1175/JCLI-D-12-00546.1.

Case. K., Kruizinga. G., and Wu. S. 2002, "GRACE Level 1B Data Product User Handbook", JPL Publication D-22027.

Chen, J., Wilson, C., Tapley, B., and Ries, J. 2004. Low degree gravitational changes from GRACE: Validation and interpretation, Geophys Res Lett, 31.

Chen, J., Wilson, C., Famiglietti, J., & Rodell, M., 2007. Attenuation effect on seasonal basin-scale water storage changes from GRACE time-variable gravity, J Geodesy, 81, 237-245, DOI: 10.1007/s00190-006-0104-2.

Chen, J., Wilson, C., & Tapley, B., 2011. Interannual variability of Greenland ice losses from satellite gravimetry, J. Geophys. Res-Sol. Ea., 116, DOI: 10.1029/2010JB007789.

Cheng, M., Tapley, B. D., and Ries, J. C. 2013. Deceleration in the Earth's oblateness, J Geophys Res-Sol EA, 118, 740-747.

Cogley, J. G. 2004. Greenland accumulation: An error model, J Geophys Res-Atmos (1984–2012), 109.

Colgan, W., Box, J. E., Andersen, M. L., Fettweis, X., Csathó, B., Fausto, R. S., Van As, D., and Wahr, J. 2015. Greenland high-elevation mass balance: inference and implication of reference period (1961–90) imbalance, Ann. Glaciol, 56, 105-117, DOI: http://dx.doi.org/10.3189/2015AoG70A967.

References

Colgan, W., Abdalati, W., Citterio, M., Csatho, B., Fettweis, X., Luthcke, S., Moholdt, G., and Stober, M. 2015. Hybrid inventory, gravimetry and altimetry (HIGA) mass balance product for Greenland and the Canadian Arctic, Remote Sens. Environ, 168, 24–39, doi:10.1016/j.rse.2015.06.016.

Cox, C., Humphrey, N., and Harper, J. 2015. Quantifying meltwater refreezing along a transect of sites on the Greenland ice sheet, The Cryosphere, 9(2), 691-701.

Deb, K., Pratap, A., Agarwal, S., & Meyarivan, T., 2002. A fast and elitist multiobjective genetic algorithm: NSGA-II, Evol. Comput., IEEE Transactions on, 6, 182-197, DOI: 10.1109/4235.996017.

Gardner, A. S., Moholdt, G., Cogley, J. G., Wouters, B., Arendt, A. A., Wahr, J., Berthier, E., Hock, R., Pfeffer, W. T., Kaser, G., Ligtenberg, S. R., Bolch, T., Sharp, M. J., Hagen, J. O., van den Broeke, M. R., and Paul, F. 2013. A Reconciled Estimate of Glacier Contributions to Sea Level Rise: 2003 to 2009, Science, 340 (6134), 852-857, DOI:10.1126/science.1234532.

Enderlin, E. M., Howat, I. M., Jeong, S., Noh, M. J., Angelen, J. H., and Broeke, M. R. 2014. An improved mass budget for the Greenland ice sheet, Geophys Res Lett, 41, 866-872.

Ettema, J., van den Broeke, M. R., van Meijgaard, E., van de Berg, W. J., Bamber, J. L., Box, J. E., and Bales, R. C. 2009. Higher surface mass balance of the Greenland ice sheet revealed by high-resolution climate modeling, Geophys Res Lett, 36, L12501, doi:10.1029/2009GL038110.

Fettweis, X. 2007. Reconstruction of the 1979–2006 Greenland ice sheet surface mass balance using the regional climate model MAR, The Cryosphere Discussions, 1, 123-168.

Forsberg, R. and Reeh, N.: Mass change of the Greenland Ice Sheet from GRAC E. 2007. Gravity Field of the Earth – 1st meeting of the International Gravity Field Service, Harita Der-gisi, Ankara, vol. 73, avaialble at: http://www.igfs.net.

Gallée, H. and Schayes, G. 1994. Development of a three-dimensional meso-γ primitive equation model: Katabatic winds simulation in the area of Terra Nova Bay, Antarctica, Mon Weather Rev, 122, 671-685.

Greve, R., and Blatter, H. 2009. Dynamics of ice sheets and glaciers, Springer Science & Business Media.

Groh, A., Ewert, H., Fritsche, M., Rülke, A., Rosenau, R., Scheinert, M., and Dietrich, R. 2014. Assessing the Current Evolution of the Greenland Ice Sheet by Means of Satellite and Ground-Based Observations, Surv Geophys, 1-22.

Hamilton, G. S., & Whillans, I. M., 2002. Local rates of ice-sheet thickness change in Greenland, Ann. Glaciol., 35, 79-83, DOI: 10.3189/172756402781817383.

Hanna, E., Huybrechts, P., Janssens, I., Cappelen, J., Steffen, K., and Stephens, A. 2005. Runoff and mass balance of the Greenland ice sheet: 1958–2003, J Geophys Res-Atmos (1984–2012), 110, D13108, doi:10.1029/2004JD005641.

Hansen, P. C., 1992. Analysis of discrete ilL-posed problems by means of the L-curve, SIAM REV, 34, 561-580, DOI:10.1137/1034115.

Harig, C., and Simons, F 2016.Ice mass loss in Greenland, the Gulf of Alaska, and the Canadian Archipelago: Seasonal cycles and decadal trends, Geophys. Res. Lett., 43, 3150–3159, doi:10.1002/2016GL067759.

Hoegh-Guldberg, O and Bruno, JF. 2010. The impact of climate change on the world's marine ecosystems. Science,1523-1528. doi:10.1126/science.1189930.

Howat, I. M., Ahn, Y., Joughin, I., van den Broeke, M. R., Lenaerts, J., and Smith, B. 2011. Mass balance of Greenland's three largest outlet glaciers, 2000–2010, Geophys. Res. Lett, 38, L12501/1–L12501/5, doi:10.1029/2011GL047565.

Howat, I. M. and Eddy, A. 2011. Multi-decadal retreat of Greenland's marine-terminating glaciers, J Glaciol, 57, 389-396.

Jacob, T., Wahr, J., Pfeffer, W. T., & Swenson, S., 2012. Recent contributions of glaciers and ice caps to sea level rise, Nature, 482, 514-518, DOI::10.1038/nature10847.

Jin, S. and Zou, F., 2015. Re-estimation of glacier mass loss in Greenland from GRACE with correction of land–ocean leakage effects, Glob Planet Change, 170-178.

Johannessen, O. M., Khvorostovsky, K., Miles, M. W., and Bobylev, L. P. 2005. Recent ice-sheet growth in the interior of Greenland, Science, 310, 1013-1016.

Joughin, I., Das, S. B., King, M. A., Smith, B. E., Howat, I. M., and Moon, T. 2008. Seasonal speedup along the western flank of the Greenland Ice Sheet, Science, 320(5877), 781-783.

Jürgen, B., Kalyanmoy, D., Kaisa, M., and Roman S. 2008. Multiobjective Optimization: Interactive and Evolutionary Approaches, ISBN: 978-3-540-88907-6.

Khan, S. A., Kjær, K. H., Bevis, M., Bamber, J. L., Wahr, J., Kjeldsen, K. K., Bjørk, A. A., Korsgaard, N. J., Stearns, L. A., and van den Broeke, M. R. 2014. Sustained mass loss of the northeast Greenland ice sheet triggered by regional warming, Nature Climate Change, 4(4), 292–299.

Kjeldsen, K. K., Khan, S. A., Wahr, J., Korsgaard, N. J., Kjær, K. H., Bjørk, A. A., Hurkmans, R., Broeke, M. R., Bamber, J. L., and Angelen, J. H. 2013. Improved ice loss estimate of the northwestern Greenland ice sheet, J Geophys Res-Sol EA, 118, 698-708.

Klees, R., Liu, X., Wittwer, T., Gunter B.C., Revtova, E.A.,Tenzer, R., Ditmar, P., Winsemius, H.C. and Savenije, H.H.G.: 2008, A comparison of global and regional GRACE models for land hydrology. Surv Geophys, 29, 335–359. DOI: 10.1007/s10712-008-9049-8

Korona, J., Berthier, E., Bernard, M., Rémy, F., and Thouvenot, E. 2009. SPIRIT. SPOT 5 stereoscopic survey of Polar Ice: reference images and topographies during the fourth International Polar Year (2007–2009), ISPRS Journal of Photogrammetry and Remote Sensing, 64(2), 204-212.

Krabill, W., Abdalati, W., Frederick, E., Manizade, S., Martin, C., Sonntag, J., Swift, R., Thomas, R., Wright, W., Yungel, J. 2000. Greenland ice sheet: high-elevation balance and peripheral thinning, Science, 289(5478), 428–430 (doi: 10.1126/science.289.5478.428)

Kusche, J. 2007 ,Approximate decorrelation and non-isotropic smoothing of time-variable GRACE-type gravity field models, J. Geodyn.,81,733–749, doi:10.1007/s00190-007-0143-3.

Lenaerts, J., den Broeke, M., Déry, S., Meijgaard, E. v., Berg, W., Palm, S. P., and Sanz Rodrigo, J. 2012. Modeling drifting snow in Antarctica with a regional climate model: 1. Methods and model evaluation, Journal of Geophysical Research: Atmospheres, 117(D5).

Livingstone, S., Clark, C., Woodward, J., and Kingslake, J. 2013. Potential subglacial lakes and meltwater drainage pathways beneath the Antarctic and Greenland ice sheets, The Cryosphere, 7, 1721-1740.

Luthcke, S. B., Sabaka, T., Loomis, B., Arendt, A., McCarthy, J., and Camp, J. 2013 Antarctica, Greenland and Gulf of Alaska land-ice evolution from an iterated GRACE global mascon solution, J Glaciol, 59, 613-631.

Luthcke, S. B., Zwally, H., Abdalati, W., Rowlands, D., Ray, R., Nerem, R., Lemoine, F., McCarthy, J., and Chinn, D. 2006 Recent Greenland ice mass loss by drainage system from satellite gravity observations, Science, 314, 1286-1289.

McMillan, M., Nienow, P., Shepherd, A., Benham, T., and Sole, A. 2007. Seasonal evolution of supra-glacial lakes on the Greenland Ice Sheet, Earth and Planetary Science Letters, 262(3), 484-492.

Moon, T., Joughin, I., Smith, B., Broeke, M. R., Berg, W. J., Noël, B., and Usher, M. 2014. Distinct patterns of seasonal Greenland glacier velocity, Geophys. Res. Lett, 41, 7209-7216.

Noël, B., van de Berg, W. J., van Meijgaard, E., Kuipers Munneke, P., van de Wal, R. S. W., and van den Broeke, M. R. 2015. Evaluation of the updated regional climate model RACMO2.3: summer snowfall impact on the Greenland Ice Sheet, The Cryosphere, 9, 1831-1844, doi:10.5194/tc-9-1831-2015.

Ohmura, A. and Reeh, N. 1991. New precipitation and accumulation maps for Greenland, J. Glaciol, 37, 140-148.

Palmer, S. J., Dowdeswell, J. A., Christoffersen, P., Young, D. A., Blankenship, D. D., Greenbaum, J. S., Benham, T., Bamber, J., and Siegert, M. J. 2013. Greenland subglacial lakes detected by radar, Geophysical Research Letters, 40(23), 6154-6159.

Parry, M. L. 2007. Climate change 2007-impacts, adaptation and vulnerability: Working group II contribution to the fourth assessment report of the IPCC, Cambridge University Press.

Paulson, A., Zhong, S., and Wahr, J. 2007. Inference of mantle viscosity from GRACE and relative sea level data, Geophys J Int, 171, 497-508.

Peltier, W. 2004. Global glacial isostasy and the surface of the ice-age Earth: the ICE-5G (VM2) model and GRACE, Annu. Rev. Earth Planet. Sci, 32, 111-149.

Petersen, G. N., Kristjánsson, J. E., and Ólafsson, H. 2004. Numerical simulations of Greenland's impact on the Northern Hemisphere winter circulation, Tellus A, 56(2), 102-111.

Pfeffer, W. T., Meier, M. F., and Illangasekare, T. H. 1991. Retention of Greenland runoff by refreezing: implications for projected future sea level change, Journal of Geophysical Research: Oceans, 96(C12), 22117-22124.

Ray, R., and Luthcke, S., 2006. Tide model errors and GRACE gravimetry: towards a more realistic assessment, Geophys. J. Int., 167, 1055-1059, DOI: 10.1111/j.1365-246X.2006.03229.x.

Rignot, E., Box, J., Burgess, E., and Hanna, E. 2008. Mass balance of the Greenland ice sheet from 1958 to 2007, Geophys Res Lett, 35, L20502.1-L20502.5, doi:10.1029/2008GL035417.

Rignot, E. and Kanagaratnam, P. 2006. Changes in the velocity structure of the Greenland Ice Sheet, Science, 311, 986-990.

Rignot, E., Velicogna, I., van den Broeke, M., Monaghan, A., and Lenaerts, J. 2011. Acceleration of the contribution of the Greenland and Antarctic ice sheets to sea level rise, Geophys Res Lett, 38, L05503.1-L05503.5, doi:10.1029/2011GL046583.

Rodell, M., Houser, P., Jambor, U. e. a., Gottschalck, J., Mitchell, K., Meng, C., Arsenault, K., Cosgrove, B., Radakovich, J., and Bosilovich, M. 2004. The global land data assimilation system, Bulletin of the American Meteorological Society, 85, 381-394.

Rowlands, D., Luthcke, S., McCarthy, J., Klosko, S., Chinn, D., Lemoine, F., Boy, J. P., & Sabaka, T., 2010. Global mass flux solutions from GRACE: a comparison of parameter estimation strategies—mass concentrations versus Stokes coefficients, J. Geophys. Res-Sol. Ea., 115, DOI: 10.1029/2009JB006546.

Sabaka, J., Rowlands, D., Luthcke S., and J.-P. Boy, J., 2010. Improving global mass flux solutions from Gravity Recovery and Climate Experiment (GRACE) through forward modeling and continuous time correlation, J Geophys Res-Sol, 115, 10.1029/2010JB007533.

Sasgen, I., Martinec, Z., and Bamber, J. 2010. Combined GRACE and InSAR estimate of West Antarctic ice mass loss, J Geophys Res-Earth (2003–2012), 115, F04010, doi: 10.1029/2009JF001525.

Sasgen, I., van den Broeke, M., Bamber, J. L., Rignot, E., Sørensen, L. S., Wouters, B., Martinec, Z., Velicogna, I., and Simonsen, S. B. 2012. Timing and origin of recent regional ice-mass loss in Greenland, Earth Planet SC Lett, 333, 293-303

Schrama E., Wouters B, and D.A. Lavallée 2007 Signal and noise in Gravity Recovery and Climate Experiment (GRACE) observed surface mass variations. JGR 112, B08407 doi:10.1029/ 2006JB004882.

Schrama, E., Wouters, B., and Vermeersen, B., 2011. Present day regional mass loss of Greenland observed with satellite gravimetry, Surv. Geophys., 32, 377-385, DOI: 10.1007/s10712-011-9113-7.

Schrama, E. J. and Wouters, B. 2011. Revisiting Greenland ice sheet mass loss observed by GRACE, J Geophys Res-Sol EA (1978–2012), 116, 377–385, doi: 10.1007/s10712-011-9113-7.

Schrama, E. J., Wouters, B., and Rietbroek, R. 2014. A mascon approach to assess ice sheet and glacier mass balances and their uncertainties from GRACE data, J Geophys Res-Sol EA.

Shepherd, A., Ivins, E. R., Geruo, A., Barletta, V. R., Bentley, M. J., Bettadpur, S., Briggs, K. H., Bromwich, D. H., Forsberg, R., and Galin, N. 2012. A reconciled estimate of ice-sheet mass balance, Science, 338, 1183-1189.

Simpson, M. J., Milne, G. A., Huybrechts, P., and Long, A. J. 2009. Calibrating a glaciological model of the Greenland ice sheet from the Last Glacial Maximum to present-day using field observations of relative sea level and ice extent, Quaternary Sci Rev, 28, 1631-1657.

Sørensen, L. S. and Forsberg, R. 2010. Greenland ice sheet mass loss from GRACE monthly models, gravity, Geoid Earth Obs., 135, 527–532, doi:10.1007/978-3-642-10634-7_70.

Sørensen, L. S., Simonsen, S. B., Nielsen, K., Lucas-Picher, P., Spada, G., Adalgeirsdottir, G., Forsberg, R., and Hvidberg, C. 2011. Mass balance of the Greenland ice sheet (2003–2008) from ICESat data-the impact of interpolation, sampling and firn density, The Cryosphere, 5, 173-186.

Swenson, S., & Wahr, J., 2002. Methods for inferring regional surface mass anomalies from Gravity Recovery and Climate Experiment (GRACE) measurements of time variable gravity, J. Geophys. Res-Sol. Ea., 107, ETG 3-1-ETG 3-13, DOI: 10.1029/2001JB000576.

Swenson, S., Wahr, J., and Milly, P. 2003. Estimated accuracies of regional water storage variations inferred from the Gravity Recovery and Climate Experiment (GRACE), Water Resour Res, 39, 11.1-11.3, doi:10.1029/2002WR001808.

Swenson, S. and Wahr, J. 2006. Post-processing removal of correlated errors in GRACE data, Geophys Res Lett, 33, L08402, doi:10.1029/2005GL025285.

Swenson, S., & Wahr, J., 2007. Multi-sensor analysis of water storage variations of the Caspian Sea, Geophys. Res. Lett., 34, L16401, DOI: 10.1029/2007GL030733.

Swenson, S., Chambers, D., and Wahr, J. 2008. Estimating geocenter variations from a combination of GRACE and ocean model output, J Geophys Res-Sol EA (1978–2012), 113.

B.D. Tapley, B.D., Bettadpur. S., Watkins. M., and Reigber. C. 2004. The gravity recovery and climate experiment: Mission overview and early results. Geophys. Res. Lett., 31:L09607. doi: 10.1029/2004GL019920.

Tedesco, M., Fettweis, X., Mote, T., Wahr, J., Alexander, P., Box, J., and Wouters, B. 2013. Evidence and analysis of 2012 Greenland records from spaceborne observations, a regional climate model and reanalysis data, The Cryosphere, 7.

Thomas, R., Csatho, B., Davis, C., Kim, C., Krabill, W., Manizade, S., McConnell, J., and Sonntag, J. 2001. Mass balance of higher-elevation parts of the Greenland ice sheet, J Geophys Res-Atmos (1984–2012), 106, 33707-33716.

Tiwari, V. M., Wahr, J., and Swenson, S. 2009. Dwindling groundwater resources in northern India, from satellite gravity observations, Geophys. Res. Lett., 36, L18401, doi:10.1029/2009GL039401.

Tikhonov, A. N. 1963. Regularization of incorrectly posed problems, Soviet Math. Dokl, 1624-1627.

Unden, P., Rontu, L., Järvinen, H., Lynch, P., Calvo, J., Cats, G., Cuxart, J., Eerola, K., Fortelius, C., and Garcia-Moya, J. A. (2002), HIRLAM-5 scientific documentation.

Uppala, S. M., Kållberg, P., Simmons, A., Andrae, U., Bechtold, V., Fiorino, M., Gibson, J., Haseler, J., Hernandez, A., and Kelly, G. 2005. The ERA-40 re-analysis, Q J Roy Meteor Soc, 131, 2961-3012.

van Angelen, J., Lenaerts, J., Lhermitte, S., Fettweis, X., Kuipers Munneke, P., van den Broeke, M., and Van Meijgaard, E. 2012. Sensitivity of Greenland Ice Sheet surface mass balance to surface albedo parameterization: a study with a regional climate model, The Cryosphere, 6.

van de Wal, R., Boot, W., Smeets, C., Snellen, H., van den Broeke, M., and Oerlemans, J. 2012. Twenty-one years of mass balance observations along the K-transect, West Greenland, Earth system science data discussions, 5, 351-363.

van den Broeke, M., Bamber, J., Ettema, J., Rignot, E., Schrama, E., van de Berg, W. J., van Meijgaard, E., Velicogna, I., and Wouters, B. 2009. Partitioning recent Greenland mass loss, science, 326, 984-986.

van den Broeke, M., Enderlin, E., Howat, I., Munneke, P., Noël, B., van de Berg, W., van Meijgaard, E., and Wouters, B., 2016. On the recent contribution of the Greenland ice sheet to sea level change, The Cryosphere, 10, 10, 1933–1946, doi:10.5194/tc-10-1933-2016

van der Wal, W., Barnhoorn, A., Stocchi, P., Gradmann, S., Wu, P., Drury, M., and Vermeersen, B. 2013. Glacial isostatic adjustment model with composite 3-D Earth rheology for Fennoscandia, Geophys J Int, 194, 61-77.

Velicogna, I., & Wahr, J., 2005. Greenland mass balance from GRACE, Geophys. Res. Lett., 32, DOI: 10.1029/2005GL023955.

Velicogna, I., & Wahr, J., 2006. Measurements of time-variable gravity show mass loss in Antarctica, Science, 311, 1754-1756, DOI: 10.1126/science.1123785.

Velicogna, I., 2009. Increasing rates of ice mass loss from the Greenland and Antarctic ice sheets revealed by GRACE, Geophys. Res. Lett., 36, DOI: 10.1029/2009GL040222.

Velicogna, I. and Wahr, J. 2013. Time-variable gravity observations of ice sheet mass balance: Precision and limitations of the GRACE satellite data, Geophys Res Lett, 40, 3055-3063.

Ran, J., Ditmar, P., Klees, R. et al. 2017 Statistically optimal estimation of Greenland Ice Sheet mass variations from GRACE monthly solutions using an improved mascon approach. J Geod., https://doi.org/10.1007/s00190-017-1063-5

Sutterley, T., and van den Broeke, M. 2014. Regional acceleration in ice mass loss from Greenland and Antarctica using GRACE time-variable gravity data, Geophys Res Lett, 8130–8137, doi: 10.1002/2014GL061052.

Vernon, C., Bamber, J., Box, J., van den Broeke, M., Fettweis, X., Hanna, E., and Huybrechts, P. 2013. Surface mass balance model intercomparison for the Greenland ice sheet, The Cryosphere, 7, 599-614.

Wahr, J., Molenaar, M., and Bryan, F. 1998. Time variability of the Earth's gravity field: Hydrological and oceanic effects and their possible detection using GRACE, Journal of Geophysical Research, 103, 30205-30230,30229.

Wouters, B., Chambers, D., and Schrama, E. 2008. GRACE observes small-scale mass loss in Greenland, Geophys Res Lett, 35, L20501, doi:10.1029/2008GL034816.

Wouters, B., Bamber, J., van den Broeke, M., Lenaerts, J., and Sasgen, I. 2013. Limits in detecting acceleration of ice sheet mass loss due to climate variability, Nat Geosci, 6, 613-616.

Xu, Z., Schrama, E., and van der Wal, W. 2015. Optimization of regional constraints for estimating the Greenland mass balance with GRACE level-2 data, Geophys J Int, 202, 381-393.

Xu, Z., Schrama, E., Van der Wal, W., Van den Broeke, M. and Enderlin, E.M.: Improved GRACE regional mass balance estimates of the Greenland Ice Sheet cross-validated with the Input-output method, The Cryospehre Discussion, 1, 1-18, doi: doi:10.5194/tc-10-1-2016, 2016.

Zwally, H. and Giovinetto, M. 2000. Spatial distribution of net surface mass balance on Greenland, Ann Glaciol, 31, 126-132.

Zwally, H., Schutz, B., Abdalati, W., Abshire, J., Bentley, C., Brenner, A., Bufton, J., Dezio, J., Hancock, D., and Harding, D. 2002. ICESat's laser measurements of polar ice, atmosphere, ocean, and land, J Geodyn, 34, 405-445.

Zwally, H. J., Giovinetto, M. B., Li, J., Cornejo, H. G., Beckley, M. A., Brenner, A. C., Saba, J. L., and Yi, D. 2005. Mass changes of the Greenland and Antarctic ice sheets and shelves and contributions to sea-level rise: 1992–2002, J Glaciol, 51, 509-527.

Zwally, H. J., Jun, L., Brenner, A. C., Beckley, M., Cornejo, H. G., Dimarzio, J., Giovinetto, M. B., Neumann, T. A., Robbins, J., and Saba, J. L. 2011. Greenland ice sheet mass balance: distribution of increased mass loss with climate warming; 200307 versus 19922002, J Glaciol, 57, 88-102.

Zwally, H. J., Mario B. Giovinetto, Matthew A. Beckley, and Jack L. Saba. 2012. http://icesat4.gsfc.nasa.gov/cryo_data/ant_grn_drainage_systems.php, last access: 09-02-2015.

Curriculum Vitae

Zheng Xu was born in Jiangsu, China in November 1983. From 2002 to 2006 he studied at the Mathematics and Applied Mathematics College of Nanjing University of Finance and Economics, Nanjing, China. After three years practice in an insurance company in China, he enrolled in the UNESCO international education program in 2010 and started his graduate education on Hydroinformations at the UNESCO-IHE institute, Netherlands. He completed his master thesis on high performance compution and optimization at this institute. In 2011, Zheng Xu was selected as PhD candidate and joined the Astrodynamics and Space Missions group at the Faculty of Aerospace Engineering at the Delft University of Technology in the Netherlands.

List of Publications

Journal Articles

Xu, Z., Schrama, E., and van der Wal, W.: Optimization of regional constraints for estimating the Greenland mass balance with GRACE level-2 data, Geophys J Int, 202, 381–393, 2015. https://doi.org/10.1093/gji/ggv146

Xu, Z., Schrama, E., van der Wal, W., Van den Broeke, M. and Enderlin, E.M.: Improved GRACE regional mass balance estimates of the Greenland Ice Sheet cross-validated with the Input-output method,The Cryosphere, 1, https://doi.org/10.5194/tc-10-895-2016.

Conference abstracts

Z. Xu, E.Schrama, (2012) A better GRACE solution for improving the regional Greenland mass balance, *European Geosciences Union (EGU) General Assembly*, 2012, 14, 3773, in Vienna, Austria.

Z. Xu, E. Schrama, (2013) Identify regional surface mass changes in Greenland from GRACE satellite data, *European Geosciences Union (EGU) General Assembly*, 2013, 15, EGU2013–9829, in Vienna, Austria.

Z. Xu, C. Vélez, D. Solomatine, A. Lobbrecht, (2010) Use of cloud computing for optimal design of urban wastewater systems, *9th International Conference on Hydroinformatics*, 2010, Tianjin, China.

W. van der Wal, Z. Xu, (2016) 3D viscosity maps for Greenland and effect on GRACE mass balance estimates, *European Geosciences Union (EGU) General Assembly*, 2016, 18, EPSC2016-10010, in Vienna, Austria.